SLOPE SCALE MODELING OF SNOW SURFACE TEMPERATURE IN TOPOGRAPHICALLY COMPLEX TERRAIN

by

James Mark Staples

A thesis submitted in partial fulfillment
of the requirements for the degree

of

Master of Science

in

Civil Engineering

MONTANA STATE UNIVERSITY
Bozeman, Montana

December 2008

APPROVAL

of a thesis submitted by

James Mark Staples

This thesis has been read by each member of the thesis committee and has been found to be satisfactory regarding content, English usage, format, citation, bibliographic style, and consistency, and is ready for submission to the Division of Graduate Education.

Dr. Edward E. Adams

Approved for the Department of Civil Engineering

Dr. Brett W. Gunnik

Approved for the Division of Graduate Education

Dr. Carl A. Fox

STATEMENT OF PERMISSION TO USE

In presenting this thesis in partial fulfillment of the requirements for a master's degree at Montana State University, I agree that the Library shall make it available to borrowers under rules of the Library.

If I have indicated my intention to copyright this thesis by including a copyright notice page, copying is allowable only for scholarly purposes, consistent with "fair use" as prescribed in the U.S. Copyright Law. Requests for permission for extended quotation from or reproduction of this thesis in whole or in parts may be granted only by the copyright holder.

James Mark Staples

December 2008

ACKNOWLEDGEMENTS

I would like to thank the Department of Civil Engineering at Montana State University for support; Brian McGlynn in the Department of Land Resources and Environmental Sciences and the National Science Foundation for limited use of LIDAR data; and the Yellowstone Club and the Ski Patrol for access and significant help with the field sites and instrumentation. Thanks to Dr. Edward Adams for his advising and guidance; Dr. Ladean McKittrick for his help running the model; Robb Larson for his help with instrumentation; and Andrew Slaughter for his extraordinary efforts to program the weather stations and collect and organize the data.

TABLE OF CONTENTS

TABLE OF CONTENTS – CONTINUED

LIST OF TABLES

LIST OF FIGURES

LIST OF FIGURES - CONTINUED

LIST OF FIGURES - CONTINUED

LIST OF FIGURES - CONTINUED

LIST OF FIGURES - CONTINUED

ABSTRACT

In mountainous terrain, landscape can influences the thermal state of snow. Snow temperature and mass flux have been calculated using an energy balance model, Radtherm/RT, to account for the effects of topography and meteorological conditions. For a specific location, a terrain model is defined and contains a connected assemblage of elements or facets. Each element has a specified terrain type with assigned thermal properties. Meteorological data are applied, and a one dimensional energy balance is calculated for each element. This energy balance includes conduction, convection, radiation, and latent heat; however, the calculation of radiation is unique. Taking into account topography, global position, and time, the model is used to calculate incoming solar radiation for each element as well as reflected short wave radiation and the exchange of long wave radiation between terrain surfaces. Light detection and ranging topographic data with a one meter resolution were used to create separate models (on the order of 10^4 m^2) for two slopes in southwest Montana. Meteorological data were collected at these two slopes as well as a third location having a relatively unobstructed view of the sky. The results for elements in different locations and under different meteorological conditions were compared. Readily available USGS topographic data with a 30 meter resolution were used to create a model (on the order of 10^6 m^2) containing both slopes. For this model of a much larger scale, surface temperatures and mass flux were again calculated and compared with results for the slope scale models. Incoming long wave radiation from the atmosphere only was found to be critical input data for accurate temperature calculations. The set value for albedo also had a major effect. When suitable long wave data and good estimations of albedo were used, snow surface temperature was calculated with accuracies on the order of several degrees. Additionally, when surface hoar deposition and growth was observed and reasonable temperature results were achieved, calculated values of mass flux were consistently positive. In one instance, observed variations in surface hoar growth across a slope matched calculated variations in mass flux across the same slope.

CHAPTER 1

INTRODUCTION

Snow covers 40% of land in the northern hemisphere during winter months [Rees 2006] and 6.6 million square miles of North America [NASA 2008] (Figure 1); consequently, it has important implications in environmental studies. In mountainous regions, snow is an important component in the study of glaciology and landscape morphology. In the Western United States, snow provides a significant source of water; however, snow also presents a very real and constant threat of avalanches in mountain ranges where people live, work, and recreate. Since 1998 in the United States, 28 people per year have died in avalanches on average [GNFAC 2008]. Many more are likely caught and injured but not reported. In addition to the threat to human life, avalanche control measures and highway closures incur large costs to both local highway departments and economies.

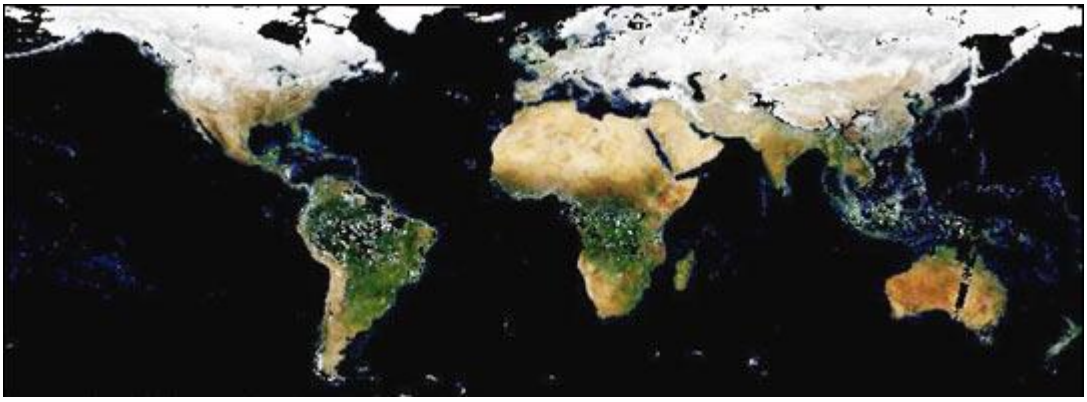

Figure 1. Composite satellite image from NASA's Multi-angle Imaging SpectroRadiometer (MISR) taken during the months December 2001 to February 2002 showing extent of snow cover over the northern hemisphere [NASA].

Examples of available data reveal that during the winter of 2007 and 2008, the Colorado Department of Transportation (DOT) spent 7,586 hours on avalanche mitigation and experienced 184.5 hours of road closures [Colorado DOT Fact Book 2007-2008]. During the previous season, they experienced 955 hours of road closures [Colorado DOT Fact Book 2006-2007]. According to the Washington State DOT, closures of I-90 over Snoqualmie Pass costs the state economy more than $500,000 per hour. During the winter of 2007-2008 Washington DOT used 12,421 pounds of explosives for avalanche control on Snoqualmie and Stevens Passes, and Snoqualmie Pass was closed for 370 hours as a result of avalanche control [Washington State DOT 2008]. A better understanding of the processes that lead to avalanches can limit the loss of revenue and human life.

Avalanches are broadly classified as one of two types: loose snow or slab avalanches. Loose snow avalanches initiate at discrete points and entrain surface layers of snow as they move down slope, whereas slab avalanches fracture across large areas and along discrete shear boundaries within the snowpack [McClung and Schaerer 1993]. Many professionals focus their forecasting and avalanche mitigation on slab avalanches, because this type causes most avalanche fatalities in North America [Tremper 2001]. Slab avalanches require four components to occur: a slab, a weak layer, a steep slope, and a trigger (Figure 2).

The slab is a layer of cohesive snow which runs down slope and comprises the avalanche, a trigger initiates a weak layer failure, a weak layer propagates a fracture under the slab, and a steep slope allows the slab to overcome friction. Slab avalanches

are notably dangerous because weak layers often fail across large areas allowing the slab to quickly move down slope as a relatively cohesive unit.

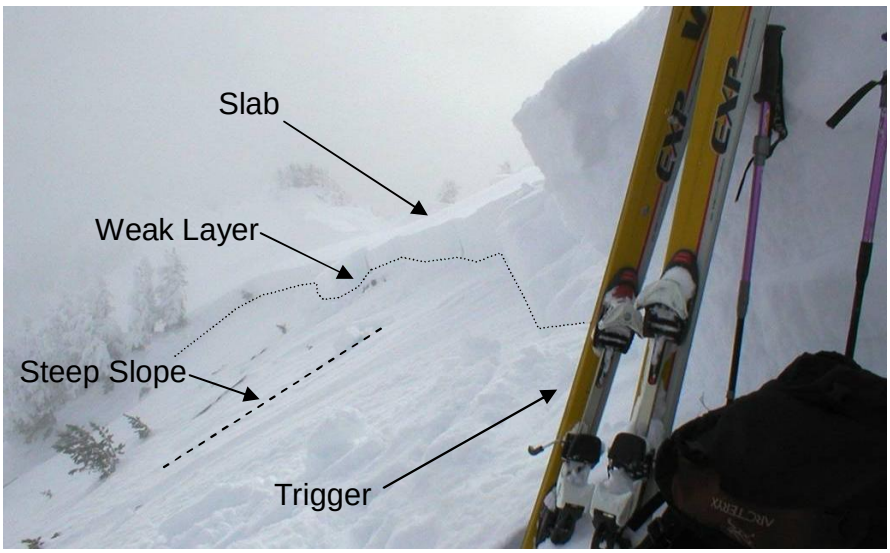

Figure 2. The four components necessary for an avalanche showing part of the slab which did not slide.

A skier or rider (the trigger) can initiate a failure, which will propagate long distances in all directions, through the weak layer. In this situation the person is caught in the avalanche with little opportunity to escape. This situation contrasts loose snow avalanches in which the avalanche occurs immediately below the trigger and fans out as it moves down slope.

A combination of environmental variables such as sun, wind, precipitation, and temperature creates a stratified snowpack which contains layers of relatively weak and strong snow [Tremper 2001]. Strong layers form when snow crystals metamorphose into rounded forms that bond well and form a slab. Weak layers form when a combination of processes causes snow crystals to metamorphose into sharp, angular crystals that do not bond well. Weak layers can form at or near the snow surface where subsequent snowfall covers the weak layer and becomes a slab. Because such weak layers form on the

surface, it is the energy balance at the snow surface that controls their formation [Marks and Dozier 1992]. To better understand these processes and the ensuing weak layer formation as well as understanding weak layer variations across seemingly uniform slopes, it is desirable to model the energy balance at the snow surface over complex terrain. Modeling these variations over large spans of time and space is nearly impossible by hand requiring a very large number of computations [Fierz et al. 2003].

The purpose of this project is to conduct these computations using a first principles energy balance model, RadThermRT. This model has been used to account for the effects of weather, snow properties, topography and other landscape features on the energy balance over two small slopes in southwest Montana. A similar study was conducted for the Bridger Mountain Range but over a larger area [Adams et al. 2004b]. The primary result in this project is a calculation of snow surface temperature because it is the predominant force driving weak layer formation. A secondary result is mass flux because the deposition of water vapor on the snow surface adds heat to the energy balance and forms a type of weak layer.

CHAPTER 2

BACKGROUND

Weak Layers

Varied environmental and atmospheric conditions transform new snowflakes into rounded forms and faceted forms (Figure 3), thus creating a layered snowpack. Each of these layers has different mechanical properties which affect avalanche formation.

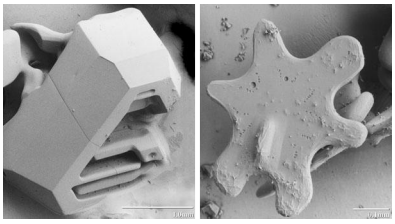

Figure 3. Scanning electron microscope images of a faceted form (left) and a rounded form (right). [photos from USDA, http://emu.arsusda.gov/snowsite/default.html]

As a general rule, rounded snow crystals tend to comprise strong layers in a snowpack, and faceted snow crystals tend to make up weak layers in a snowpack. The following section will give a description of three common weak layers.

One possible weak layer is a layer of new snow less cohesive than overlying snow, but this type tends to gain strength relatively quickly, and few deadly avalanches occur on such weak layers in southwest Montana [Birkeland 1998]. Most fatal avalanches occur within weak layers containing faceted snow. Temperature gradients in excess of 10^0C/m often metamorphose existing snow crystals into faceted crystals [McClung and Schaerer 1993]. The exact nature of this metamorphic process is discussed in the following section on metamorphism. These faceted crystals do not bond

well, take significant time to gain strength as a layer, and can propagate fractures over very long distances. Depending on how and where they form, three types of faceted snow crystals can be found: depth hoar, near-surface facets, and surface hoar. Between 1990 and 1996 in the mountains of southwest Montana, 94% of all investigated backcountry avalanches occurred on weak layers containing one of these three types [Birkeland 1998]. Of those avalanches, 90% occurred on faceted crystals which had formed at the snow surface [Birkeland 1998].

Faceted Snow Crystals: Depth Hoar

Depth hoar forms in the basal layers of a snowpack early in winter when the snowpack is thin, and the air is cold. Temperatures at the snow-ground interface are near zero degrees Celsius, and air temperatures are often much colder. In this setting, large temperature differences, a relatively shallow snowpack, and relatively warm temperatures at the ground can lead to conditions favorable to form depth hoar.

Faceted Snow Crystals: Near-Surface Facets

Near-surface facets, as the name implies, are weak faceted snow crystals formed at or near the snow surface in response to large temperature gradients. These faceted crystals can form as a result of three processes: melt-layer recrystallization, diurnal recrystallization, and radiation recrystallization [Birkeland 1998].

Melt-Layer Recrystallization: When relatively cold snow is deposited on wet snow with liquid water at 0^0C, very large temperature gradients develop and produce melt-layer recrystallized facets. Warm air temperatures, solar radiation, rain, wet

snowfall or a combination of these occurrences generate a wet snow surface at 0^0C. The ensuing temperature gradient depends on the temperature of the newly fallen cold snow (Figure 4). This temperature gradient continues as liquid water in the warm snow releases latent heat during the refreezing process. Fukuzawa and Akitaya [1993] observed this process in Japan when warm wet snow was covered by 2 cm of cold dry snow. This process has also been documented in Canada [Jamieson and Langevin 2004] and Utah [Greene and Johnson 2002].

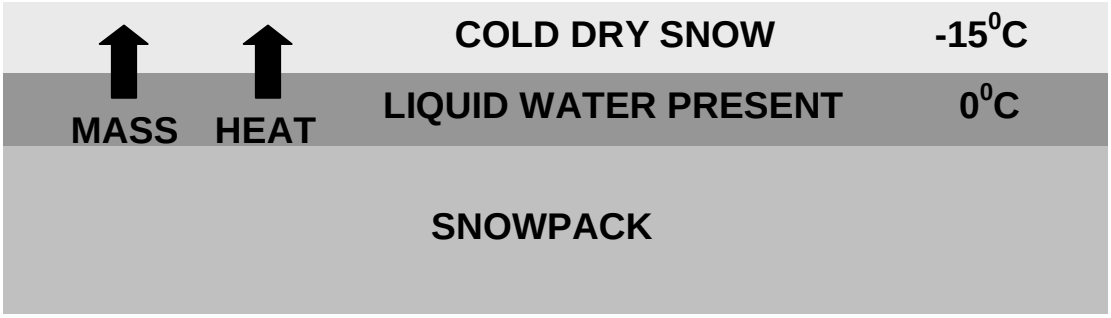

Figure 4. Conditions under which the melt-layer recrystallization process occurs. Faceted snow crystals will form near at the interface of the warm, wet snow and the cold, dry snow.

Diurnal Recrystallization: Near a depth of 30cm below the surface, snow temperatures change slowly, while temperatures at the snow surface can change rapidly. Diurnal recrystallization occurs when the snow surface temperature experiences large temperature fluctuations between day and night as a result of diurnal fluctuations in air temperature and solar radiation (Figure 5). Because deeper layers of snow remain at a relatively constant temperature and surface snow experiences large temperature changes, significant temperature gradients occur and form faceted snow crystals near the surface.

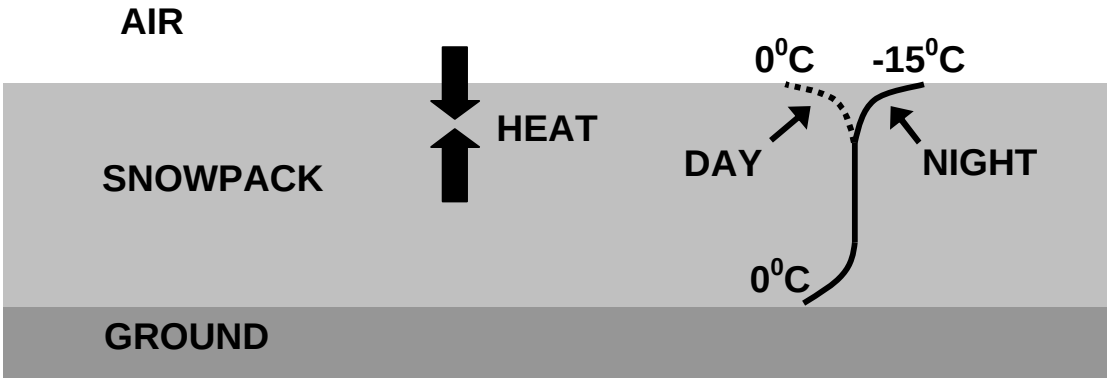

Figure 5. Diurnal fluctuations of the snow surface temperature create steep temperature gradients and can produce faceted crystals near the snow surface.

Radiation-Recrystallization: Faceted snow crystals can also form near the snow surface as a result of radiation-recrystallization. This process requires a radiation balance commonly found during clear weather. Under these conditions, the snow surface reflects most solar radiation, absorbs some, and transmits some to underlying layers. Clear skies allow the snow surface to emit significant long wave radiation (strictly a surface phenomenon) and lose heat. This loss of heat at the surface balances or exceeds the heat gain from solar radiation. The snow surface remains relatively cold, subsurface layers become relatively warm, and resulting temperature gradients can produce faceted crystals (Figure 6).

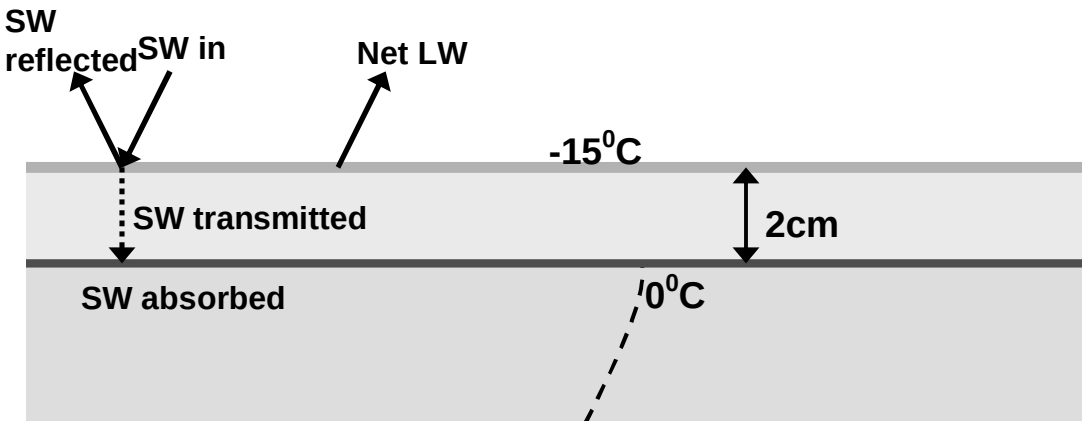

Figure 6. Conditions under which radiation recrystallization occurs and faceted snow crystals from just under the snow surface.

Faceted Snow Crystals: Surface Hoar

Surface hoar forms directly on snow from atmospheric water vapor. It is not formed by the metamorphosis of an existing crystal (Figure 7). Under clear skies, the snow surface can experience rapid losses of heat by the emission of long wave radiation. Significant temperature gradients develop between the snow surface and relatively warmer air. When this air is warm enough and contains sufficient moisture, it will deposit water vapor on the snow surface. This process is similar to the condensation of dew in summer months, except the water vapor is deposited on the snow surface in a solid form. The resulting faceted crystals are called surface hoar.

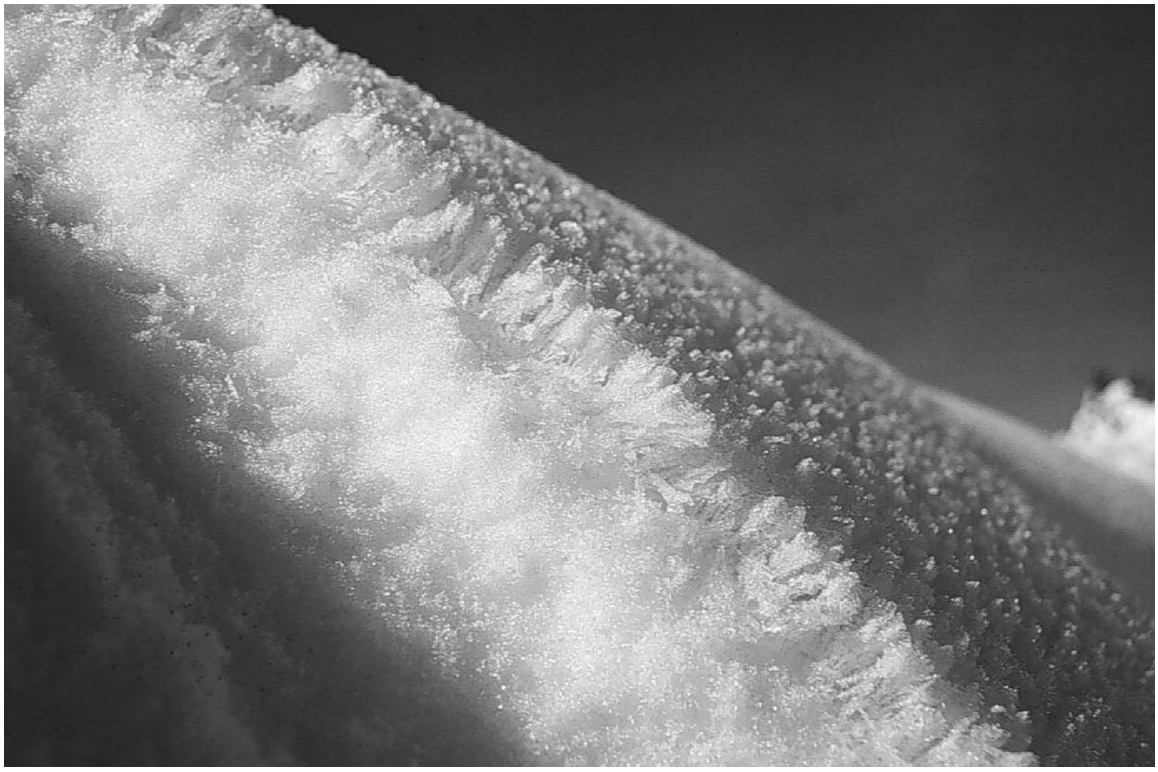

Figure 7. Feathery surface hoar crystals formed on this snow when water vapor was deposited on the snow surface. (Courtesy of the Gallatin National Forest Avalanche Center)

Metamorphism

Upon reaching earth's surface, snow is subjected to an ever changing set of environmental conditions. As a result of these changing conditions, a complex exchange of heat and energy occurs between the atmosphere, snow, and the ground. This exchange drives a continual metamorphism of snow crystals made possible by saturated air in pore spaces and water vapor diffusion throughout a snowpack. The movement of water vapor is controlled by vapor pressure gradients which vary according to temperature, temperature gradient and the curvature of snow crystals.

Single Crystals

The curvature of individual snow crystals creates vapor pressure gradients which exist in the saturated air surrounding such crystals and drive vapor diffusion. The small radius of curvature at a tip of a new snow crystal has a higher vapor pressure than the larger radius of curvature at the core of the crystal or near an adjacent, old, rounded crystal [Colebeck 1980]. For this reason the core of a new snow crystal will gain mass at the expense of the arms on a new snow crystal (Figure 8). Also, larger snow crystals will gain mass at the expense of smaller snow crystals.

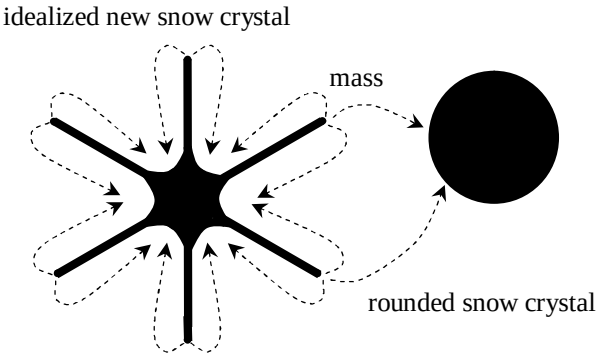

Figure 8. Idealized representation of a new snow crystal and a rounded older snow crystal which shows the mass movement resulting from curvature effects.

In laboratory experiments where temperature has been held constant, curvature effects tend to metamorphose new snow grains into relatively round shapes (Figure 9). Areas of higher vapor pressure (the sharp ends) lose mass to areas of lower vapor pressure (areas with a larger radius of curvature). This same metamorphosis occurs outside laboratory environments, but it is accelerated by temperature gradients which further increase differences in vapor pressure and accelerate the metamorphism.

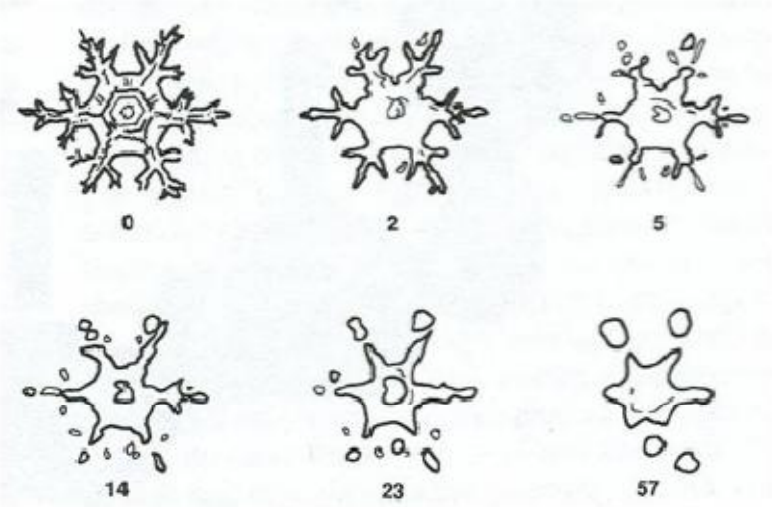

Figure 9. Sketches of a new snow crystal metamorphosing in a constant temperature environment. The number under each crystal represents the time in days. [Reproduced from McClung and Schaerer 1993]

Multiple Crystals

Snow crystals do not exist in isolation in a snowpack, and vapor pressure gradients arising from difference in temperature of a snowpack (Figure 10) tend to dominate the metamorphosis of snow [McClung and Schaerer 1993]. This situation contrasts vapor pressure gradients arising from curvature effects over the scale of a single crystal. In a snowpack, mass moves from warmer regions with higher saturation vapor pressures to colder regions with lower saturation vapor pressures. This mass transfer occurs as water vapor moves across pore spaces from one snow crystal to another (Figure 11). When the temperature gradient increases beyond 20^0C/m, this metamorphosis accelerates and produces faceted snow crystals which have sharp corners and straight edges [Colebeck 1982]. These faceted crystals are also called kinetic growth crystals. The transition to kinetic growth has been defined as a discrete point, but it is most likely a

continuum over which kinetic growth increasingly becomes the dominant metamorphosis [Miller et al. 2003].

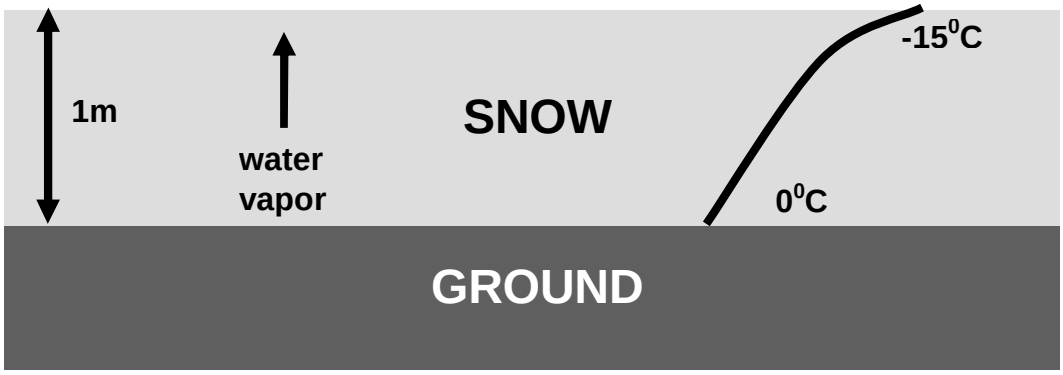

Figure 10. Schematic showing a 15^{0}C/m temperature gradient in a winter snowpack where water vapor moves from warm basal layers through pore spaces to relatively colder overlying layers of snow.

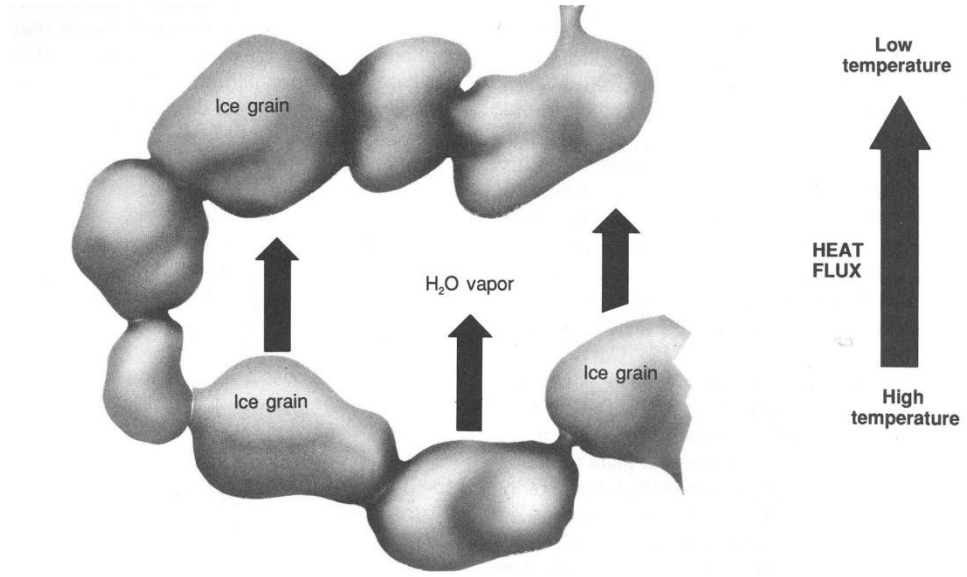

Figure 11. Water vapor movement across a pore space within a snowpack from areas of warmer temperature to areas of colder temperature. The water vapor in this schematic is deposited on the bottom sides of the top ice or snow grains. These snow grains then lose water vapor from their top sides to other, slightly colder, snow grains. [Reproduced from McClung and Schaerer 1993]

The morphologic state of snow grains is particularly important because it largely controls almost all of the material properties of snow [Colebeck 1982]. This morphologic state combined with the manner by which individual grains are connected and arranged is commonly referred to as the microstructure which also largely controls the mechanical and physical properties of snow [Schneebeli 2004]. Other physical properties, such as thermal conductivity and reflectivity are critically important for the energy balance and may possibly accelerate the growth of faceted crystals. With respect to avalanches, the mechanical properties of faceted snow are critically important because such crystals form especially weak and persistent layers in a snowpack.

CHAPTER 3

METHODOLOGY

Study Sites

Two talus covered slopes in southwest Montana have been used in this project for slope scale verification and development of the energy balance model, RadThermRT. These slopes are located at the Yellowstone Club in the Madison Range. The Yellowstone Club (YC) Ski Patrol provided access to these sites and significant assistance in setting up and maintaining these sites. These slopes were the location of previous work by Cooperstein et al. [2004]. They lie below timberline in generally wind protected areas. One slope (Figure 12) is south facing with an elevation of 2757m, and the other (Figure 13) is north facing with an elevation of 2532m. They are situated near a latitude of 45 degrees and have slope angles of roughly 30 degrees.

Instrumentation

Each site contained a weather station which measured:

1. Wind speed and direction (Met One Instruments, Inc. 034B-L)
2. Air temperature and relative humidity (Campbell Scientific, Inc. CS215)
3. Snow depth (NovaLynx Corp.)
4. Snow surface temperature (Everest Interscience Model 4000-4ZL non-contact infrared sensor, accuracy $\pm$ 0.5^0C)
5. Snow temperatures within the top 30cm of snow (an array of Omega Engineering, Inc. type T thermocouples)

6. Snow temperature at the ground (Omega Engineering, Inc, type T thermocouple)
7. Incoming short wave radiation (Eppley Laboratories Precision Spectral Pyranometer, PSP, and Li-Cor Pyranometers LI-200)
8. Reflected short wave radiation (Li-Cor Pyranometers LI-200)
9. Incoming long wave radiation (Eppley Laboratories Precision Infrared Radiometer, PIR).

Measurements were taken every ten minutes, and the average of every half hour was recorded. Additional temperature data were recorded for rock outcrops and vegetation with stand-alone thermistor/datalogger units (Onset Corp., -HOBO dataloggers). The accuracy of these measurements is questionable, as the thermistors were either taped to the rock surface or tied to tree limbs. It is possible that the thermistor on the rocks heated at a different rate from the rocks in response to solar radiation.

Figure 12. South-facing study site with weather station located next to the three skiers. The rock band above the weather station was a notable feature where rock temperature was measured with a stand-alone thermistor/data logger unit.

Additional incoming short wave (Eppley Laboratories PSP) and long wave (Eppley Laboratories PIR) radiation data were recorded at an existing weather station run by the YC Ski Patrol. At every site, the pyranometers and radiometers were mounted level in a horizontal plane several feet above the snow surface.

Figure 13. North-facing study site with meteorlogical station located next to the skier. The shadowing of solar radiation is evident in long shadows of adjacent trees. A small ridge with ski tracks can be seen just behind the weather station.

Data Collection and Maintenance

During the 2005-2006 winter, MSU personnel made weekly visits to each site for data collection and station maintenance. A significant component of this maintenance included sweeping snow off the pyranometers and radiometers, but this task only occurred weekly and radiation data following snowfall were often skewed. During the 2006-2007 winter, the YC Ski Patrol took over part of the maintenance and were able to

keep the pyranometers and radiometers mostly free of snow. Additionally, they took daily observations of snow crystal morphology in the top 5 cm of snow and recorded the number of thermocouples above the snow (Figure 14).

A pyranometer (Eppley Laboratories PSP) was added to an existing weather station near the top of the American Spirit chairlift. This site provided a mostly unobstructed view of the sky. During the last two weeks of the 2006-2007 winter field season, the radiometer (Eppley Laboratories PIR) from the north-facing slope was moved to this site. The data from this two weeks were important because such data were mostly representative of atmospheric conditions and excluded radiation effects from surrounding terrain.

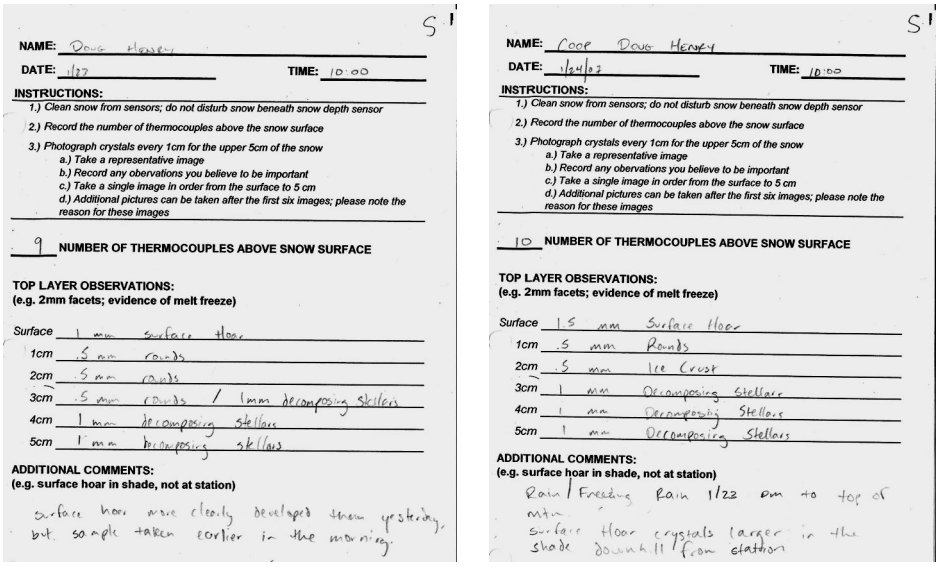

NAME: Doug Henry
DATE: 1/23 TIME: 10:00
INSTRUCTIONS:
1.) Clean snow from sensors; do not disturb snow beneath snow depth sensor
2.) Record the number of thermocouples above the snow surface
3.) Photograph crystals every 1cm for the upper 5cm of the snow
a.) Take a representative image
b.) Record any obervations you believe to be important
c.) Take a single image in order from the surface to 5 cm
d.) Additional pictures can be taken after the first six images; please note the reason for these images
9 NUMBER OF THERMOCOUPLES ABOVE SNOW SURFACE
TOP LAYER OBSERVATIONS:
(e.g. 2mm facets; evidence of melt freeze)
Surface 1 mm surface hoar
1cm .5 mm rounds
2cm .5 mm rounds
3cm .5 mm rounds / 1mm decomposing stellers
4cm 1 mm decomposing stellars
5cm 1 mm decomposing stellars
ADDITIONAL COMMENTS:
(e.g. surface hoar in shade, not at station)
surface hoar more clearly developed than yesterday, but sample taken earlier in the morning.

NAME: Coop Doug Henry
DATE: 1/24/07 TIME: 10:00
INSTRUCTIONS:
1.) Clean snow from sensors; do not disturb snow beneath snow depth sensor
2.) Record the number of thermocouples above the snow surface
3.) Photograph crystals every 1cm for the upper 5cm of the snow
a.) Take a representative image
b.) Record any obervations you believe to be important
c.) Take a single image in order from the surface to 5 cm
d.) Additional pictures can be taken after the first six images; please note the reason for these images
10 NUMBER OF THERMOCOUPLES ABOVE SNOW SURFACE
TOP LAYER OBSERVATIONS:
(e.g. 2mm facets; evidence of melt freeze)
Surface 1.5 mm Surface Hoar
1cm .5 mm Rounds
2cm .5 mm Ice Crust
3cm 1 mm Decomposing Stellars
4cm 1 mm Decomposing Stellars
5cm 1 mm Decomposing Stellars
ADDITIONAL COMMENTS:
(e.g. surface hoar in shade, not at station)
Rain / Freezing Rain 1/22 pm to top of mtn
surface floor crystals larger in the shade downhill from station

Figure 14. Two daily logs taken by the YC Ski Patrol containing observations from January 23 and 24, 2007 for the south site. Surface hoar that began growing on 22nd was observed to have grown more on both days. On the 24th the surface hoar crystals were observed to be larger at the toe of the slope in a shaded location.

Topographic Data

Two sources provided topographic data of the study sites in digital elevation maps (DEM). A DEM is an electronic file containing elevation data for a given region. Such data is publicly available through the United States Geological Survey (USGS) in the National Elevation Dataset (NED). The NED provides national elevation/topographic data in a seamless format. The datum, elevation unit, and projection are consistent within the NED. Information in the NED is updated bi-monthly to take advantage of the best available data [USGS at http://ned.usgs.gov].

At the time of this project, available data from the USGS had a 30m resolution; however, the study sites for this project have length and width dimensions about 100m. For these sites USGS data in the NED only provides a few points of elevation data. Through the Department of Land Resources and Environmental Sciences at Montana State University, LIDAR data were made available for limited use. This data has a 1m resolution, thus thousands of data points were available for each site. Appendix 1 contains detailed instructions on manipulating LIDAR data for use in RadThermRT.

LIDAR stands for Light Detection and Ranging. It works in a manner similar to RADAR, except it uses pulses of light from a laser in place of radio waves to determine distance. Because light has a much shorter wavelength than radio waves, 5 orders of magnitude difference, it can detect smaller objects more precisely. Additionally, light will reflect off many more surfaces such as vegetation. Frequently LIDAR data are collected with airborne lasers which can have vertical accuracies within 0.15 meters

[NOAA 1999]. The resulting product contains latitude, longitude, and elevation for every data point.

Two types of LIDAR data were provided: filtered and unfiltered. Filtered data give ground surface elevations, and unfiltered data give elevations of the initial light reflection, thus a graphical representation of the unfiltered data displays vegetation. The entire watershed for the West Fork of the Gallatin River is covered by this data set including a significant area around the town of Big Sky and the resort of Big Sky.

RadThermRT

The model used in this project, RadThermRT, is a first principles energy balance model commercially available from ThermoAnalytics, Inc (Figure 15). It came from software originally written for the U.S. Army and Air Force to identify the thermal/infrared signatures of vehicles [Johnson, 1991; Johnson 1995; PRISM:3.0, 1991]. The original software codes, Physically Reasonable Infrared Signature Model (PRISM) and Thermal Contrast Model (TCM), were significant in that they included the effects of flat terrain on the thermal/infrared signatures of vehicles. Adams and McDowell [1991] removed the vehicle, added topography, added a first principles model for snow, and used this software in modelling the thermal conditions of terrain.

Simple terrain models were used for validation of the energy balance calculations. Digital elevation maps (DEM) were not readily available to model more complex terrain (Figure 16). Montana State University and ThermoAnalytics, Inc. collaborated to

develop a modified version of this software, RadThermRT, specifically for highway applications in topographically complex terrain [Adams, 1999]. RadThermRT was tested to calculate pavement temperatures [Adams et al., 2004a] and provided reasonable results [McKittrick et al., 2004]. Promising results were also obtained when RadThermRT was applied to a section of the Bridger Mountain Range following the formation of a surface hoar layer. This model produced values for temperature and mass flux that seemed to agree with observed conditions [Adams et al., 2004b].

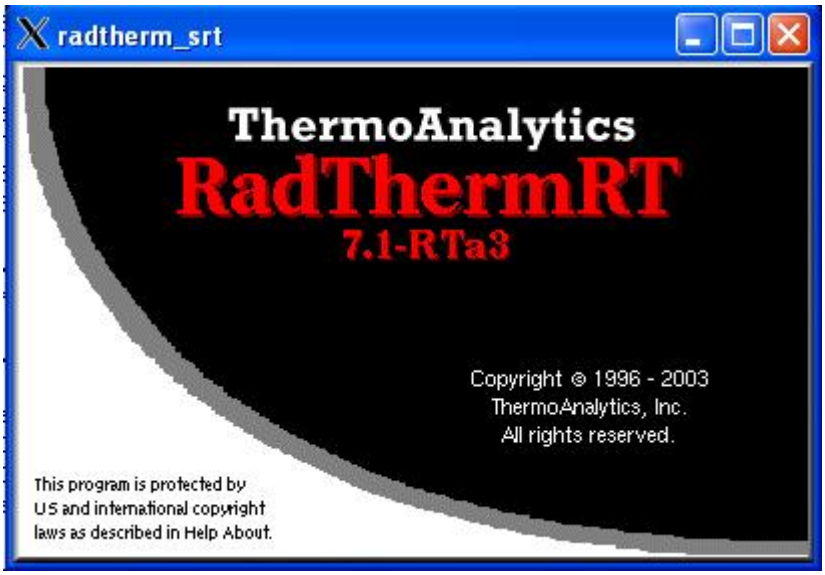

Figure 15. ThermoAnalytics RadThermRT version 7.1-RTa3 contains a calculation of latent heat and the resulting mass flux.

Building the Terrain Model

A connected network of elements/facets represents the topography for a given region of interest defined by a DEM. Every element in this network is a planar, triangular surface overlying subsurface nodes displayed as a terrain mesh in the RadThermRT GUI (Figure 17).

(a) (b)

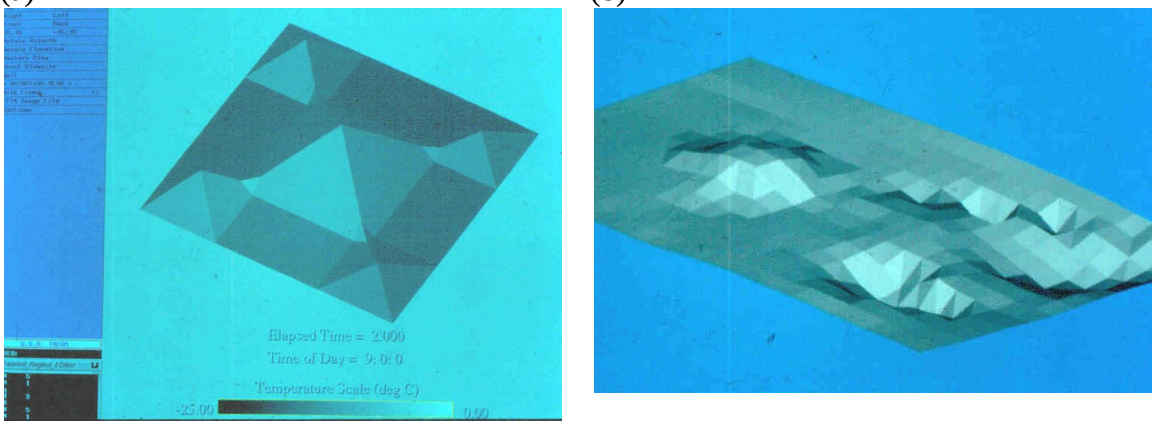

Figure 16. A terrain model of simple geometric shapes (a) shows solar warming on south facing elements and solar shading evident by cooler temperatures on north facing elements. Without readily available DEMs, another simple terrain model (b) was built using topographic data obtained with survey equipment. [Adams and McDowell 1991]

Every element belongs to a part in which all elements have the same material properties. For this project, all parts were classified as terrain surfaces which can include asphalt, concrete, foliage, soil, water, swamp, and snow. These terrain surfaces have further subdivisions allowing a more accurate assignment of material properties (Figure 18). Soil, for example, can be subdivided as average, clay, desert sand, gravel, loam, peat, sandy, or rocky field. In the case of snow, it can be further subdivided as fresh, old dry, rained upon, surface melted, or user specified absorptivity. Snow also needs its depth and core temperature specified. The core temperature is the boundary value at its basal layer and is typically assumed to be zero degrees Celsius.

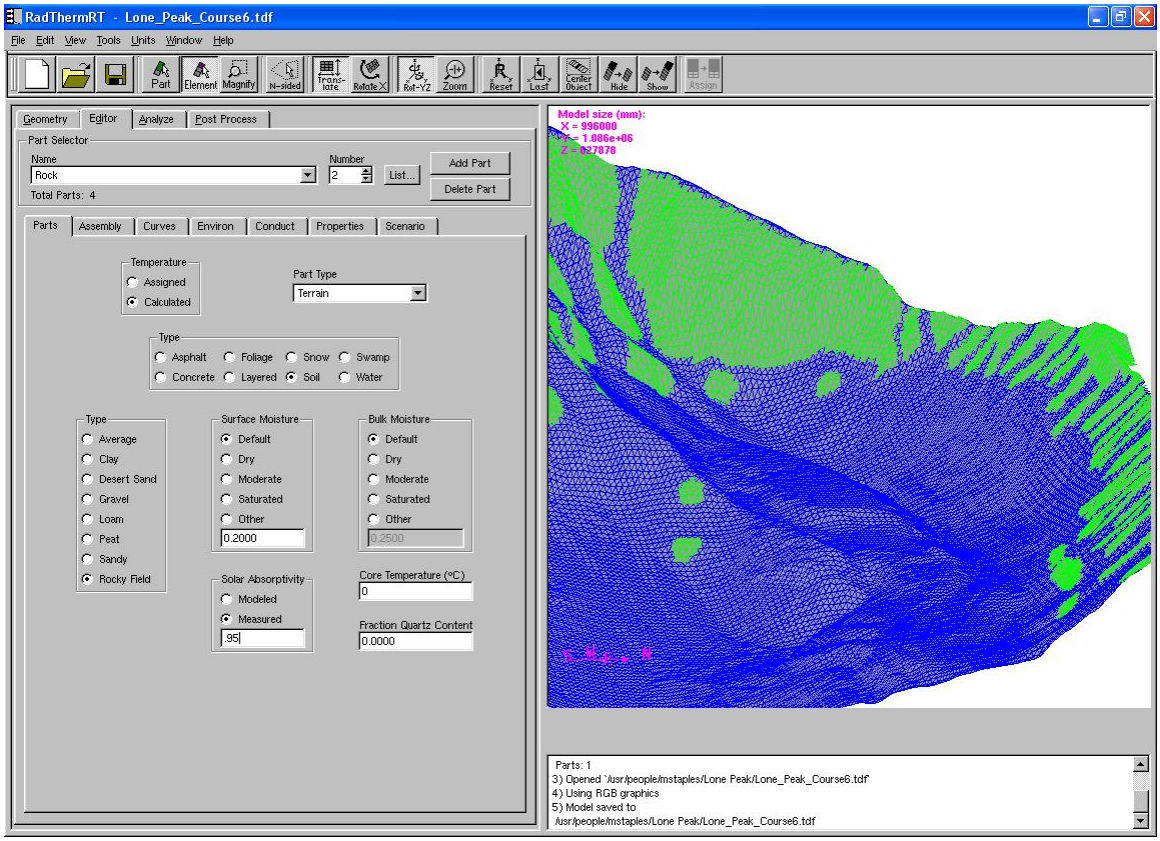

Figure 17. The Graphical User Interface (GUI) for RadThermRT showing a terrain model of the north facing cirque on nearby Lone Peak. The soil/rocky field terrain type has been selected as a part. The elements contained in this part are highlighted in the terrain mesh and represent cliffs and rock faces free of snow on Lone Peak.

The assignment of terrain IDs can be done manually or automatically using a land cover file. The LIDAR data did not have associated terrain IDs, and they were manually assigned. Different terrain types were readily apparent in the fine resolution of this data, and it was easy to identify individual trees at the study sites. Areas of rock not covered by snow were identified in the terrain mesh using the aid of a photo of the site.

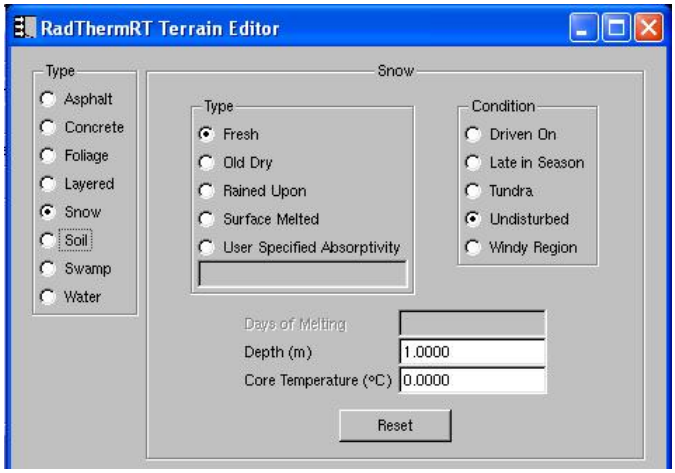

Figure 18. The terrain editor in the RadThermRT GUI showing the selection of snow as a terrain type. A depth of 1m and a core temperature of 0 deg C has been selected. The snow subtypes of fresh, old dry, and rained upon correspond to albedo values of 95%, 85%, and 40% respectively. Surface melted calls a function which is dependent on the days of melt. Snow condition determines snow density. Driven on, late in season, tundra, undisturbed, and windy region refer to densities of 600, 300, 300, 200, and 300 kg/m^3 respectively.

DEMs from the USGS had associated land cover files which were used to automatically assign terrain IDs to each element in the model. Areas labeled as grassy, rock, or shrubs were assumed to be snow covered while areas labeled as trees were assumed to be snow free. Appendix 1 contains a detailed manual describing how to collect DEM data from LIDAR, manipulate it into a usable format, and input it into RadThermRT.

To complete a terrain model after topographic data and land cover data are added, global position, weather, and default terrain must be added (Figure 19). The global position includes the coordinates, time zone, and elevation of the model. The primary need for this data is to know the position of the model relative to the position of the sun. The location of a weather file needs to be specified, and the type of solar and sky inputs need to be specified. When measured values for incoming solar (or short wave) radiation and long wave (sky) radiation have been collected, then such data are considered measured. When only cloud cover data is available, then solar and sky data are modeled

by RadThermRT. Lastly, the default terrain must be specified. The default terrain is an assumed terrain type which surrounds the terrain model.

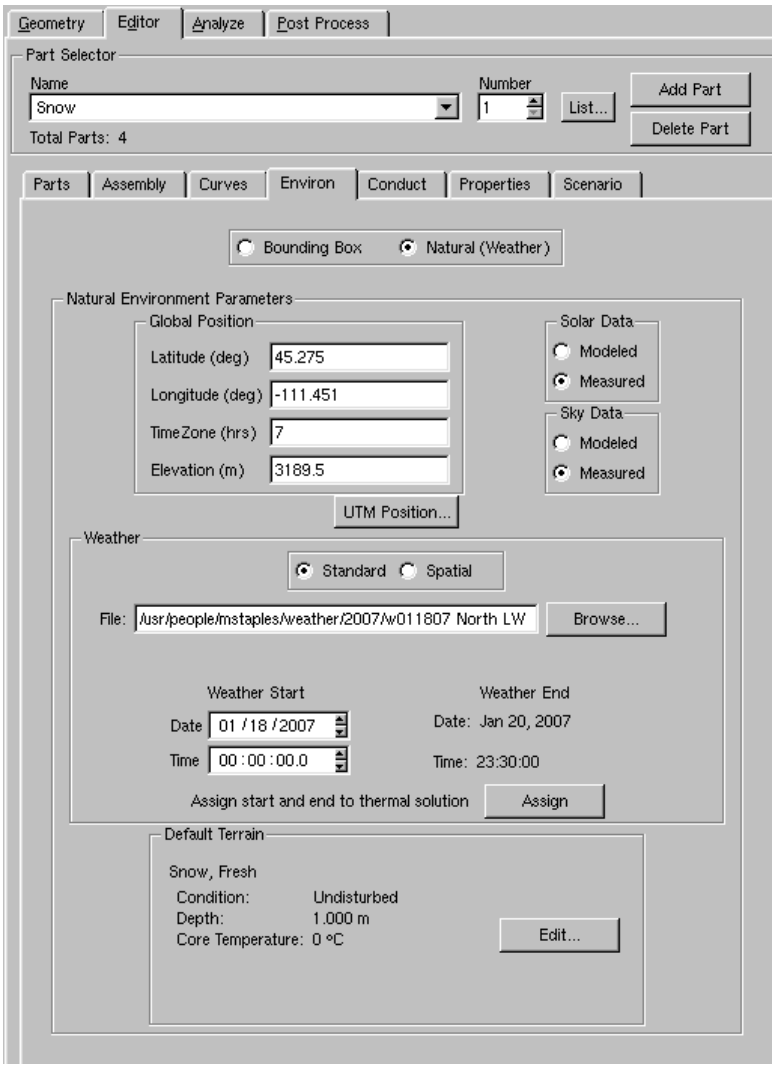

Figure 19. This window in the RadThermRT GUI provides space for the inputs of global position, weather, and default terrain. Measured solar data and sky data have been selected and mean that the weather file contains input values for solar radiation and long wave radiation. In the absence of these measurements, the weather file can contain the fraction of cloud cover, and solar and sky data will be modeled.

Ray Tracing Algorithm

A view factor file must be built based on the terrain model to calculate radiation exchange. These view factors are a necessary step to calculate the radiation exchange which is a unique strength of RadThermRT [Adams et al. 2004b]. A view factor describes the fraction of total radiation leaving a given element and striking a portion of the total surroundings. The sky, other elements, and default terrain make up the total surroundings for a given element. Because view factors are geometrical relationships between terrain elements and surroundings, they do not change and must be calculated only once. The sun does change position relative to each element, and the apparent area for direct solar radiation on each element must be repeatedly calculated.

View factors are calculated with a ray tracing algorithm that provides the necessary view factors and apparent areas in RadThermRT. View factors are later used to calculate the exchange of long wave radiation and reflected solar radiation, and apparent areas are used at each time step to calculate the direct solar radiation striking each element. In this algorithm a hemisphere is placed on the centroid of each element from which rays are cast outward (Figure 20). The ray tracing algorithm then subdivides this hemisphere so that the greatest concentration of rays is near the normal direction of each element. The fraction of the total number of rays intersecting other elements determines the view factor.

To increase the view factor accuracy, the number of rays can be increased. Each element can be subdivided so that a hemisphere is placed on each subdivision, and then rays are cast outward from each hemisphere. Creating two view factor subdivisions for

each element would then double the number of rays. To calculate apparent areas for direct solar radiation calculations, rays are cast outward from the centroid of each element. The number of rays striking the estimated solar position determines the apparent area. This number of rays can be increased by changing the settings for Apparent Area Resolution. Five different settings are possible for each component of the algorithm (Table 1).

Table 1. Settings for each component of the ray tracing algorithm can be varied to increase accuracy. Computation time increases accordingly.

Settings	View Factor Rays	View Factor Subdivisions	Apparent Area Resolution
Low	512	1	1
	1152	2	16
Medium	2048	3	32
	3200	4	48
High	4608	5	64

(a) (b)

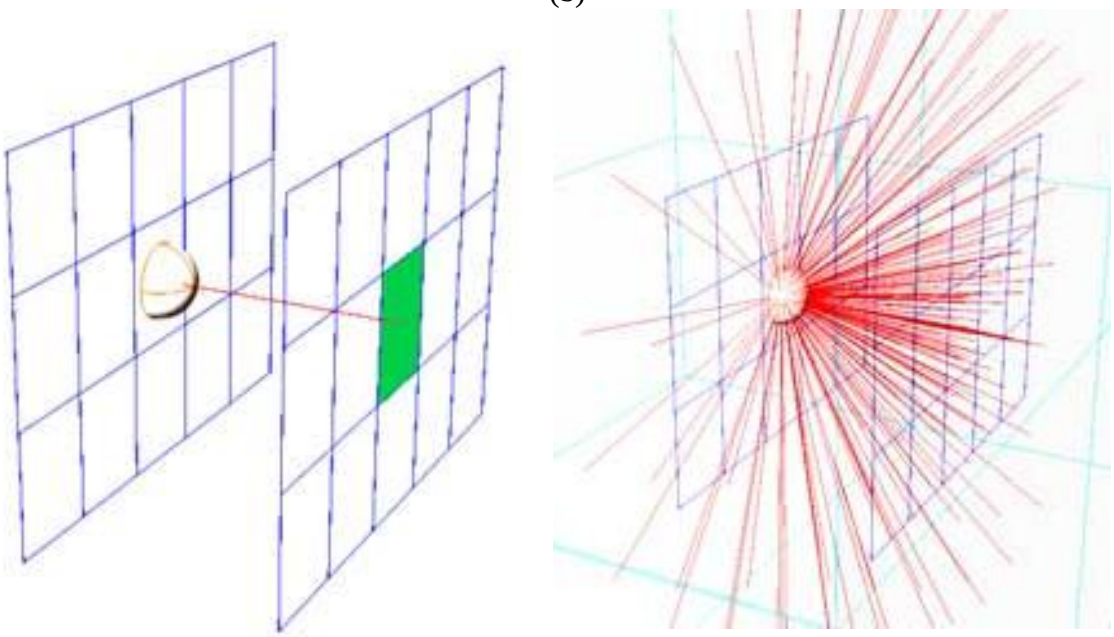

Figure 20. Image a shows the placement of a hemisphere on the centroid of an element, and the intersection of a ray with another element. Each hemisphere can have thousands of rays cast outward (b). (Images from Thermoanalytics, Inc.)

Weather File

Weather data collected in the field provide the necessary information to build a weather file (Figure 21). The following information is included in a weather file:

1. Time (in a format hhmm)
2. Air Temperature (degrees C)
3. Solar Radiation (W/m^2)
4. Wind (m/s)
5. Relative Humidity (%)
6. Cloud Cover (%)
7. Long Wave Radiation (W/m^2)
8. Wind Direction (degrees)
9. Rain Rate

The header for the weather file consists of two lines. The first should have the two digit year followed by the letter a, and the second should include the headings for the weather data (Figure 21). The weather file is then named with a "w" to designate it a weather file and followed by the date in a mmddyy format, and the letter "a" to signify that long wave radiation was recorded. Because the long wave radiation (LWIR) data were collected for this project, the cloud cover (CLOUD) data is not necessary and was set to zero. Additionally the rain rate (RAINRATE) was set to zero, thus the advective heat component to the energy balance was removed.

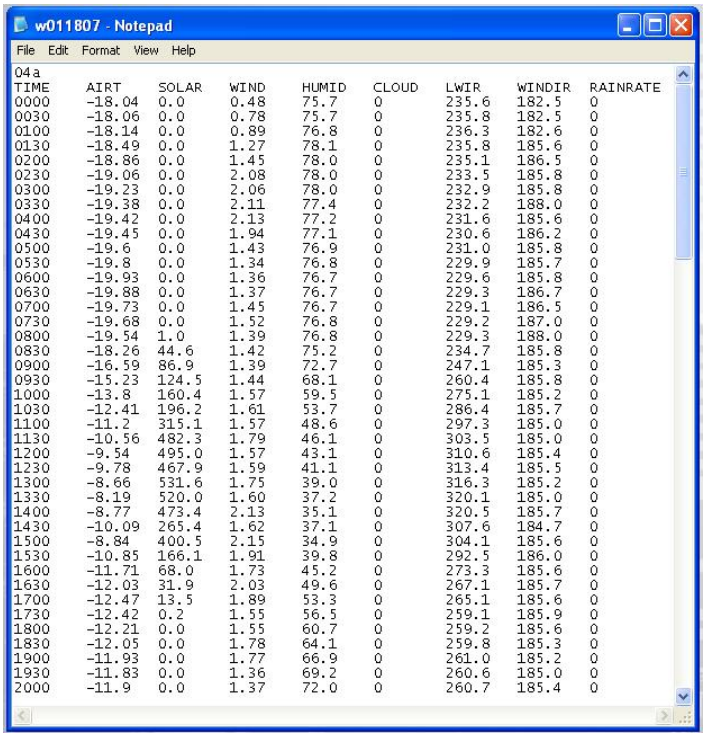

w011807 - Notepad

File Edit Format View Help

04a

TIME	AIRT	SOLAR	WIND	HUMID	CLOUD	LWIR	WINDIR	RAINRATE
0000	-18.04	0.0	0.48	75.7	0	235.6	182.5	0
0030	-18.06	0.0	0.78	75.7	0	235.8	182.5	0
0100	-18.14	0.0	0.89	76.8	0	236.3	182.6	0
0130	-18.49	0.0	1.27	78.1	0	235.8	185.6	0
0200	-18.86	0.0	1.45	78.0	0	235.1	186.5	0
0230	-19.06	0.0	2.08	78.0	0	233.5	185.8	0
0300	-19.23	0.0	2.06	78.0	0	232.9	185.8	0
0330	-19.38	0.0	2.11	77.4	0	232.2	188.0	0
0400	-19.42	0.0	2.13	77.2	0	231.6	185.6	0
0430	-19.45	0.0	1.94	77.1	0	230.6	186.2	0
0500	-19.6	0.0	1.43	76.9	0	231.0	185.8	0
0530	-19.8	0.0	1.34	76.8	0	229.9	185.7	0
0600	-19.93	0.0	1.36	76.7	0	229.6	185.8	0
0630	-19.88	0.0	1.37	76.7	0	229.3	186.7	0
0700	-19.73	0.0	1.45	76.7	0	229.1	186.5	0
0730	-19.68	0.0	1.52	76.8	0	229.2	187.0	0
0800	-19.54	1.0	1.39	76.8	0	229.3	188.0	0
0830	-18.26	44.6	1.42	75.2	0	234.7	185.8	0
0900	-16.59	86.9	1.39	72.7	0	247.1	185.3	0
0930	-15.23	124.5	1.44	68.1	0	260.4	185.8	0
1000	-13.8	160.4	1.57	59.5	0	275.1	185.2	0
1030	-12.41	196.2	1.61	53.7	0	286.4	185.7	0
1100	-11.2	315.1	1.57	48.6	0	297.3	185.0	0
1130	-10.56	482.3	1.79	46.1	0	303.5	185.0	0
1200	-9.54	495.0	1.57	43.1	0	310.6	185.4	0
1230	-9.78	467.9	1.59	41.1	0	313.4	185.5	0
1300	-8.66	531.6	1.75	39.0	0	316.3	185.2	0
1330	-8.19	520.0	1.60	37.2	0	320.1	185.0	0
1400	-8.77	473.4	2.13	35.1	0	320.5	185.7	0
1430	-10.09	265.4	1.62	37.1	0	307.6	184.7	0
1500	-8.84	400.5	2.15	34.9	0	304.1	185.6	0
1530	-10.85	166.1	1.91	39.8	0	292.5	186.0	0
1600	-11.71	68.0	1.73	45.2	0	273.3	185.6	0
1630	-12.03	31.9	2.03	49.6	0	267.1	185.7	0
1700	-12.47	13.5	1.89	53.3	0	265.1	185.6	0
1730	-12.42	0.2	1.55	56.5	0	259.1	185.9	0
1800	-12.21	0.0	1.55	60.7	0	259.2	185.6	0
1830	-12.05	0.0	1.78	64.1	0	259.8	185.3	0
1900	-11.93	0.0	1.77	66.9	0	261.0	185.2	0
1930	-11.83	0.0	1.36	69.2	0	260.6	185.0	0
2000	-11.9	0.0	1.37	72.0	0	260.7	185.4	0

Figure 21. An example of a weather file for RadThermRT for January 18, 2004.

Heat Transfer in RadThermRT

Conduction governs the transfer of heat within subsurface snow layers, and its lower boundary conditions is core temperature of the basal layer. Heat transfer for the surface layer is more complex and includes radiation and convection. Unique characteristics of the snow that create a complicated surface energy balance include [Hock 2005]:

- A fixed temperature of 0^0C during melting
- Penetration of SW radiation
- A large and highly variable albedo (reflectivity of short wave radiation)
- High thermal emissivity
- Variable surface roughness

The components of energy at the snow surface layer are conductive heat, sensible heat, latent heat, solar radiation, long wave radiation, and advective heat (Figure 22). Each of these has been calculated except advective heat which is provided by rain or snowfall which was excluded.

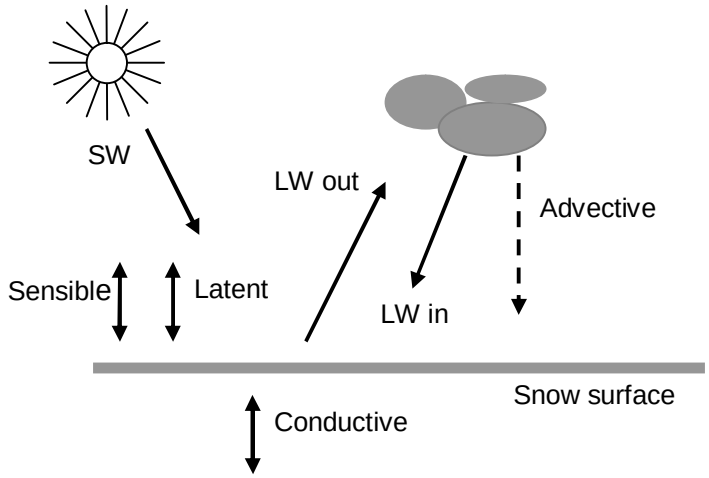

Figure 22. Energy components at the snow surface. Underlying snow provides energy through conduction. Long wave radiation is exchanged between the atmosphere, surrounding terrain, and the snow surface. Short wave radiation is supplied by the sun and surrounding terrain which reflects such radiation. Advective energy is supplied by precipitation. Sensible and Latent energy are exchanged between the snow and the air.

Conduction: The transfer of heat within a snowpack is not trivial but is approximated by conductive heat flux using Fourier's Law:

$$q_{cd_i} = -k_{eff} \frac{dT}{dz} \quad (1)$$

The q_{cdi} is the conductive heat flux (W/m^2) for element i, k_{eff} is the effective thermal conductivity ($W/m \cdot K$), T is temperature (K), and z is distance in the normal direction (m). Snow conducts heat through its ice lattice, stationary air in its poorly connected pore spaces, and vapor diffusion. The effective thermal conductivity accounts for each of these three modes [Adams and Sato 1993]. This effective thermal conductivity is

calculated as a function of snow density. Snow density is determined by setting the snow condition in the Terrain Editor of the GUI (Figure 18). Another boundary condition is insulation between adjacent elements. This condition limits conduction to the slope normal direction.

Convection: Sensible Heat: Sensible heat accounts for the heat exchange resulting from differences in temperature between snow and air, a convective heat transfer mechanism. Air temperature gradients near the snow surface can be steep and will often create strong downslope winds [Hock 2005]. Newton's Law of Cooling is used to calculate this heat flux:

$$q_{sh_i} = \bar{h}_c (T_a - T_{snow}) \tag{2}$$

$$\bar{h}_c = c_{p_a} \rho_a U_a K_c \tag{3}$$

Where q_{shi} is the sensible heat flux for element i (W/m^2), $\bar{h}_c$ is the average convective heat transfer coefficient ($W/m^2 \cdot K$), T_a is air temperature (K), T_{snowi} is the surface temperature of element i (K), c_{pa} is the specific heat of air ($J/g \cdot K$), ρ_a is the density of air (g/m^3), U_a is wind speed (m/s), and K_c is a dimensionless heat transfer coefficient. The air density is determined as a function of air temperature and elevation, and specific heat is determined as a function of air temperature.

Convection: Latent Heat: Latent heat accounts for the heat exchange as a result of phase change and the bulk motion of mass from one body to another. Snow can lose heat when water vapor sublimates away from the snowpack or gain heat when water vapor is deposited onto the snowpack. An important component in calculations of latent heat is

the calculation of mass flux, as this can produce surface hoar. The mass flux is calculated as:

$$F_{m_i} = 0.622 \rho_a U_a K_m \frac{(e_a - e_s)}{p_a} \quad (4)$$

Where F_{mi} is the mass flux ($g/m^2 \cdot s$) for element i, 0.662 is a ratio of the dry air gas constant over the water vapor gas constant, K_m is set equal to K_c, e_a is the air vapor pressure (Pa), e_s is the vapor pressure over snow (Pa), and p_a is the air pressure (Pa) [Ishikawa et al. 1999; Price et al. 1976; Adams et al. 2004b]. The Goff-Gratch equation is used to calculate the vapor pressure over snow [Goff and Gratch 1946; List 1968; Adams et al. 2004b]. The vapor pressure in air is calculated using weather inputs for air temperature and relative humidity as well as global position for air pressure. The mass flux is then used to calculate the latent heat flux:

$$q_{lh_i} = L_m F_{m_i} \quad (5)$$

Where q_{lhi} is the latent heat flux (W/m^2) for element i, and L_m is the latent heat of phase change (J/g).

Solar Radiation: Short wave (SW) or solar radiation can have a wavelength range of 0.1μm to 5.0μm. This range includes some ultraviolet (UV), all visible, and all near-infrared radiation (NIR). Solar radiation data used in this project had a wavelength range of 0.4μm - 1.1μm (LI-200) or 0.285μm - 2.8μm (Eppley PSP). The pyranometers measure solar radiation in these ranges because such radiation is strongest in these ranges. Mostly the PSP data were used. LI-200 data were only measured at the north site and used only as comparison data.

All incoming radiation, upon striking some surface, must be absorbed, reflected, or transmitted such that:

$$\alpha + \rho + \tau = 1 \quad (6)$$

Where α is the absorptivity, ρ is the reflectivity, and τ is the transmissivity. Each of these can have values ranging from 0 to 1, and they can be defined for a specific wavelength or a range of wavelengths. Within the range of solar radiation, the reflectivity for snow can be called the albedo which is often expressed as a percentage ranging from 0% - 100%. Albedo varies primarily with spectral wavelength, solar zenith angle, impurity concentrations, snow grain size, and snow depth [Wiscombe and Warren 1980]. Generally snow has a higher albedo for shorter wavelengths, larger solar zenith angles, fewer impurities, smaller grain sizes, and deeper snow depths. Additionally, new snow typically has an albedo near 100%, and a large portion of the energy from solar radiation does not necessarily affect the snowpack. Some SW radiation, depending on wavelength, is transmitted to deeper layers of snow where it is ultimately absorbed or reflected. Transmittance of SW radiation is significant because underlying layers of snow can absorb SW radiation, thus converting it to heat. A result of this transmittance is that melting can occur below the snow surface while the surface remains below freezing [Hock 2005], and large temperature gradients near the snow surface can occur. Currently in RadThermRT, all solar radiation not reflected is absorbed by the snow surface layer, and no transmittance occurs.

Components of the solar heat flux are direct solar radiation, diffuse solar radiation, and reflected solar radiation expressed in the following equation:

$$q_{sw_i} = \alpha\left(\frac{A_p}{A} I_n + F_{is} I_d\right) + \sum_{j=1}^{n} \left\{B_{ij}(1-\alpha) q_{sw\,j}\right\} \quad (7)$$

Where q_{swi} is the solar radiation heat flux (W/m^2) for element i, α is absorptivity, A_p is the projected apparent area (m^2) of element i, A is the area (m^2) of element i, I_n is direct solar radiation (W/m^2), F_{is} is the sky view factor for element i, I_d is diffuse solar radiation (W/m^2), and B_{ij} is a view factor for elements i and j. A portion of the ray tracing algorithm recalculates A_p at each time step to account for changing solar position. In RadThermRT, solar radiation reflected out of each element is guessed. Then the reflected solar radiation received by each element can be calculated and used to recalculate a new value. This process is repeated until a convergence within a defined tolerance is reached.

Long Wave Radiation: Long wave (LW) radiation is a surface phenomenon and is emitted by all matter with a temperature above zero Kelvin. Radiation emitted by most terrestrial objects can be classified as long wave and is described by the Stefan-Boltzman law:

$$E = \varepsilon\sigma T_s^4 \quad (8)$$

Where E is the emissive power or irradiance (W/m^2), ε is the emissivity (dimensionless) σ is the Stefan-Boltzman constant ($\sigma = 5.67*10^{-8}$ $W/m^2 \cdot K^4$), and T_s is the surface temperature (K). Theoretical objects know as black bodies define the upper limit of LW radiation emission for a given temperature. All other objects emit some fraction of this radiation: the emissivity ($0 \leq \varepsilon \leq 1$). Black bodies have both an emmissivity and absorptivity of 1. The wavelength of emitted radiation is also a function of temperature

as described by Wien's Law which relates the peak radiation emission to the inverse of temperature. For this reason, solar radiation is mostly short wave, and radiation emitted by natural objects in a winter environment is mostly long wave. Common sources of LW radiation that affect the snow surface are other snow surfaces, vegetation, rock outcrops, and the atmosphere, which usually is the largest source [Hock 2005]. The range of wavelengths for LW radiation is 5.0μm to 100μm, and the range measured by the Eppley PIR is 3.5μm to 50μm. This range of LW data was used as input data for calculations of sky temperature. Under cloudy skies and relatively warm sky temperatures, the snow surface can experience a net gain of LW radiation, while the snow surface can experience a net loss of LW radiation under clear skies. This exchange of LW radiation is significant for snow which has both an emissivity and absorptivity of almost one for these wavelengths.

The exchange of long wave radiation between the sky and an element as well as the exchange of this radiation between an element and all other elements is calculated with the following equation:

$$q_{lw_i} = F_{is}\left(q_{Li} - \sigma\varepsilon_i T_i^4\right) + \sigma \sum_{j=1}^{n} F_{ij}\left(\varepsilon_j T_j^4 - \varepsilon_i T_i^4\right) \qquad (9)$$

Where q_{LWi} is the net long wave radiation heat flux (W/m^2), F_{is} is the sky view factor for element i, q_{Li} is the incident long wave heat flux from the atmosphere (W/m^2), ε_i is the emissivity for element i, T_i and T_j are the surface temperatures of elements i and j (K), σ is the Stefan-Boltzman constant ($W/m^2 \cdot K^4$), and F_{ij} is the view factor between elements i and j.

Computation of Thermal Conditions

For snow RadThermRT assigns 20 layers. Of these, one is a surface node, 18 are interior nodes, and one is a bottom node with an assigned core temperature. Soil and rock elements have 13 layers, and vegetation has one canopy layer placed over 13 soil layers. Each layer has a thermal node associated with its upper and lower surface, and half the volume of each layer is assigned to the associated node. For each volume assigned to a thermal node a uniform temperature is assumed over that space. Boundary conditions include temperature of the bottom node (core temperature), temperature of airflow above the surface layer, and insulation from conduction with adjacent elements [Martilla 1999].

The final governing equations contain the transient energy equation and the net-radiation enclosure equation [Martilla 1999]. The transient energy equation is simplified because no work is done on or by any layer, thus it reduces to the following form where changes in internal energy for a differential element equate to the total heat inputs.

$$\frac{\partial E}{\partial t} = mc_p \frac{\partial T}{\partial t} = \sum Q \tag{10}$$

Where E is used to represent the internal energy (J), m is mass (g), c_p is specific heat capacity (J/g·K), T is temperature (K), t is time (s), and Q is the heat rate (W). The heat flux for each node is easily converted to heat rate because the area of each element is known. For the surface node, the sum of heat inputs is:

$$\sum Q = A(q_{cd} + q_{sh} + q_{lh} + q_{sw} + q_{lw}) \tag{11}$$

Where A is the surface area (m^2) for a given element, and each q is a heat flux (W/m^2). For all interior nodes the only heat flux is conduction, and equation 13 can be reduced to

a function of temperature and adjacent nodal temperatures. For surface nodes, q_{sw} is calculated separately as described above in an iterative process. Solar radiation does not affect interior nodes at this time. The terms q_{cd} , q_{sh} , and q_{lh} are functions of temperature, and equation 13 is then solved for q_{lw}.

To generate a second equation for q_{lw}, the net-radiation method is used. In this method, an enclosure with N surfaces is assumed to surround every element. This assumption is the same used to calculate view factors and equation 12 is then written for each of these surfaces. For each element the two resulting equations are combined to eliminate the radiative heat flux term, and the only remaining variables in the final governing equation are temperatures. This equation is solved with the Crank-Nicholson implicit finite difference scheme. A complete development of the numerical solution is given in Marttila [1999].

CHAPTER 4

RESULTS AND DISCUSSION

2005-2006 Winter

The 05/06 winter season was the first for this specific project. As such there were many unknowns, and significant time was required to get RadThermRT running and obtain and manipulate data into useable formats. The results of that season, aside from modeled thermal conditions included:

- Establishing the weather stations
- Obtaining LIDAR data
- Learning how to manipulate LIDAR data in Surfer 8
- Configuring LIDAR and weather data to input into RadThermRT
- Installing necessary software to run RadThermRT
- Building the terrain model in RadThermRT
- Assigning terrain ID's in RadThermRT
- Running RadThermRT for selected dates for both study sites
- Identifying potential sources of error

These results were the initial necessary steps in order to get RadThermRT running in order to model the thermal conditions of both study sites. This modeling was accomplished for selected dates within the 05/06 winter season including two periods in March when surface hoar formed on the snow surface.

Choosing Elements

Once weather data were available, and the terrain model was built, RadThermRT was used to calculate thermal conditions of the north-facing site and the south-facing site. These thermal conditions included a calculation of temperature and mass flux for each element of the model; however, for verification purposes, the primary focus was on temperature values of several specific elements. The most important of these was an element at the location of the weather station. The modeled snow surface temperature values for this element could be compared directly to measured values taken by the station. Other elements of snow were chosen to illustrate the effects of terrain on snow surface temperature. At the south-facing site, measured values of temperature were taken on a rock outcrop, an east-facing tree, and a north-facing tree. At these locations elements were chosen to make direct comparisons between modeled and measured temperatures.

Temperature Differences Across Terrain

An initial goal was to demonstrate the capability of RadThermRT to model thermal conditions across the snow surface and show the effects of local topography. Highly accurate LIDAR data made this feasible, as such results were not previously possible with the courser resolution of USGS digital topographic data. Many features at the study sites were not apparent in USGS data which had a resolution of 30 meters. The dimensions of the study sites are on the same order of magnitude as the 30m x 30m resolution; therefore, each study site was represented by only a few elements (Figure 23). Using the LIDAR data, each study site was represented by thousands of elements.

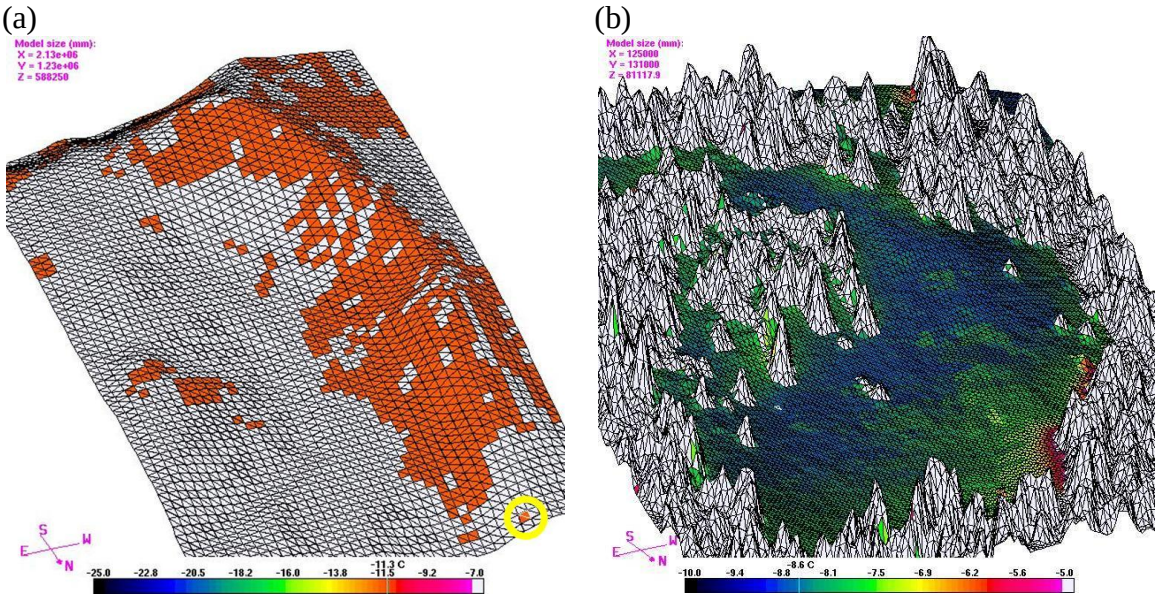

Figure 23. Images of terrain models in RadThermRT are shown. Image (a) displays Pioneer Mountain and was built using USGS 30 meter topographic data. The circled elements represent the area contained in image (b) which is the north-facing site built with LIDAR topographic data.

Surface temperatures and surface mass fluxes were calculated for each element in the model. Differences in temperature between selected elements of snow in the sun and in the shade as well as elements of rock and trees have been compared to show the effects of local topographic differences and influences of material thermal properties (Figure 24). As expected, snow surface temperatures in the shade were cooler than those exposed to direct sun.

Snow in direct sun receives significantly more heat energy from solar radiation than shaded snow which only receives diffuse and reflected solar radiation. The shaded snow, while shielded from direct solar radiation, possessed a relatively clear view of the cold sky at night. Having a clear view of the night sky is important for a material like snow with a high emissivity because it can emit a large amount of longwave radiation, lose heat energy, and experience a drop in temperature. Snow under the canopy of a

forest would be limited in its ability to lose such heat energy. While the forest canopy may have a seemingly cold surface temperature, it is warm compared to a clear night sky in winter.

Surface temperatures of a south facing rock element and a tree element (Figure 24) reached much higher values than the nearby snow surface during midday. These higher temperatures are a direct result of different material properties. The primary difference affecting these temperatures is the reflectivity or albedo. Trees and rocks can absorb significantly more solar radiation than snow, and the high reflectivity of snow means that more solar radiation is available for such trees and rocks to absorb. The absorptivity of tree and rock elements in RadThermRT was set at 70% or higher while the absorptivity for snow was set at 10% or lower. The heat capacity for rock and vegetation is lower than that for ice, and this property should also allow such terrain features to experience a more rapid rise in temperature than snow (Equation 10).

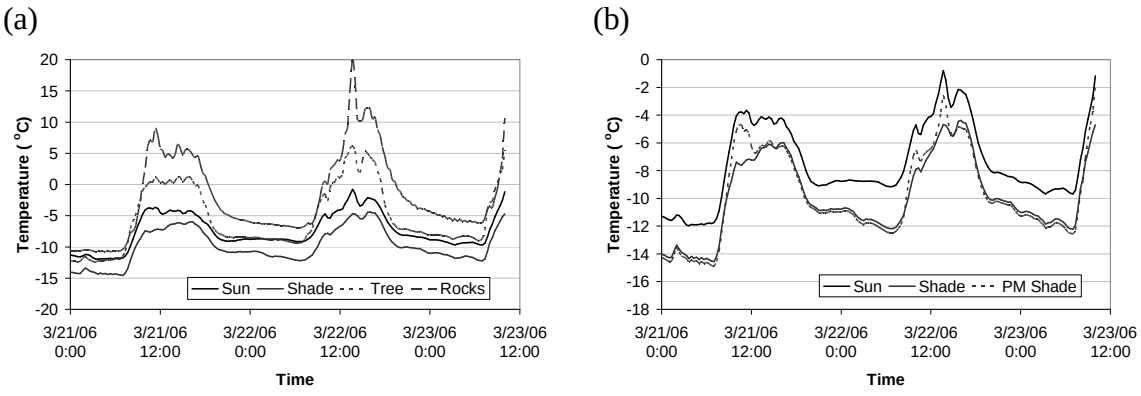

Figure 24. A comparison of modeled surface temperatures for selected elements of snow, south-facing rock, and a north-facing tree at the south-facing study site are shown. In (a) shaded snow remains at the lowest temperatures while snow experiencing direct sun is warmer, followed by a tree element and a rock element with the highest temperatures. In (b) the same snow elements as in (a) are compared with a snow element that only receives morning direct sun.

The temperature of a snow surface element subjected to afternoon shade was compared to snow elements in full sun and snow elements in full shade (Figure 24). The partially shaded snow surface maintained temperatures similar to those of fully shaded snow, but experienced higher temperatures just before the shadowing by adjacent trees took effect. Figure 25 shows surface shading on the south facing slope evident in variations in temperature. The shaded snow surface remained cooler than the snow surface exposed to direct sun as a result of such shading.

The actual snow surface temperature of the shaded snow may have been even less than the modeled values. This shaded snow receives some direct solar radiation which would have a lesser effect under real conditions than modeled conditions. Currently in RadThermRT, the absorption of direct solar radiation by snow is a function of absorptivity independent of incidence angle; however, this independence is not physically accurate [Wiscombe and Warren 1980]. More solar radiation is absorbed as it strikes snow in the normal direction. Less is absorbed as the incidence angle approaches 90 degrees. Also, snow exhibits an anisotropic reflection of solar radiation and is dependent on both viewing zenith and azimuth angles [Hudson et al. 2006]. Direct solar radition experiences forward-directed scattering once reflected by snow [Wiscombe and Warren 1980]. This preferential reflectance would lead to actual conditions being different from modeled conditions. RadThermRT assumes snow acts as a Lambertian surface and reflects direct solar radiation equally in all directions.

(a) (b)

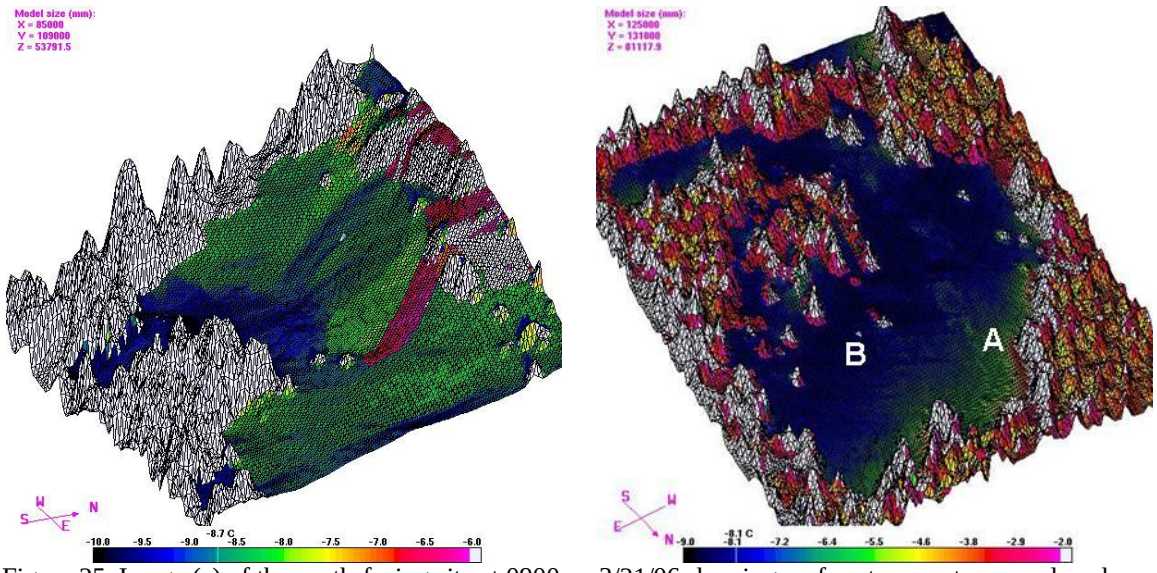

Figure 25. Image (a) of the south-facing site at 0900 on 3/21/06 showing surface temperatures, and cooler regions of snow can be seen by darker colors in shaded areas. Image (b) of the north-facing site at 10:40 on 3/21/06, and a warmer region of snow can be seen in the northwest corner. Elements A and B are labeled for reference to the plot of snow surface temperatures.

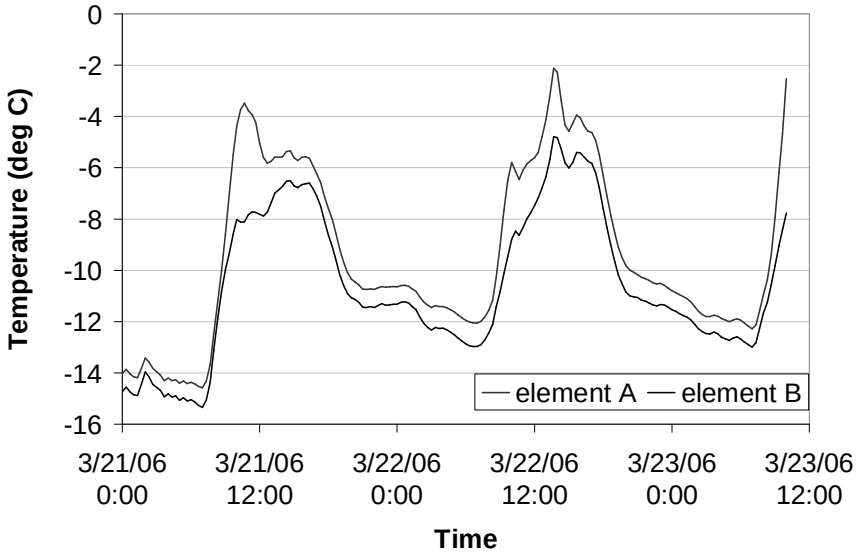

Figure 26. Modeled snow surface temperature is plotted for two elements on the north-facing site. The location of elements A and B is seen in Figure 25.

The north facing slope received little direct sun, but the northwest corner of this slope received more solar input in the morning than other areas (Figure 25). The snow surface temperatures for a fully shaded element (element B) with a clear view of the sky and a partly shaded element (element A) with a sky view partly obstructed by trees can be seen in Figure 26. The temperatures of element A show the effects of increased solar input as well as long wave radiation exchange with adjacent trees. The effect of long wave radiation is especially evident in Figure 26 during the night time hours when the snow surface of element A remained warmer than element B.

Comparison between models built with LIDAR data and USGS data

Results from LIDAR models and USGS models were compared to validate future use of RadThermRT in areas where only USGS topographic data are available (Figure 27). The course grid of the model built with USGS data only allows the selection of an element containing a large area of the selected study site. As a result, elements in the USGS model are best compared to elements in the LIDAR model exposed to a clear view of the sky and free of effects from local topographic features. Such elements of the LIDAR model should be affected less by local topographic features than elements adjacent to these features as seen in Figure 26; consequently, it is not surprising that the two plots in Figure 27 match very well.

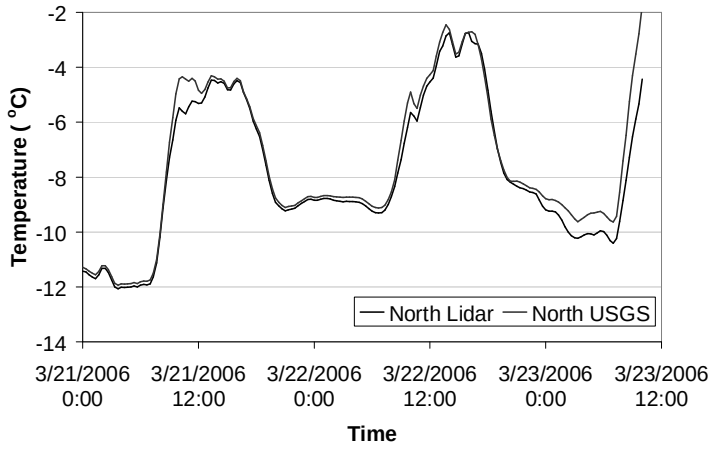

Figure 27. Comparison of modeled snow surface temperatures for carefully chosen elements on the north facing site with models built with high resolution LIDAR topographic data and much courser USGS topographic data. Comparable results were obtained in a similar comparison for the south facing site.

Measured and Modeled Temperatures

Measured and modeled temperatures have been compared for elements located in positions where surface temperatures were continuously measured and recorded. At this point in the model development, measured values of temperature are assumed to be correct despite possible instrumentation error. Such error is assumed to be minimal compared to the differences between modeled and measured values. Figure 28 shows a plot of measured and modeled temperature values for the south facing slope during the two periods in March.

(a)

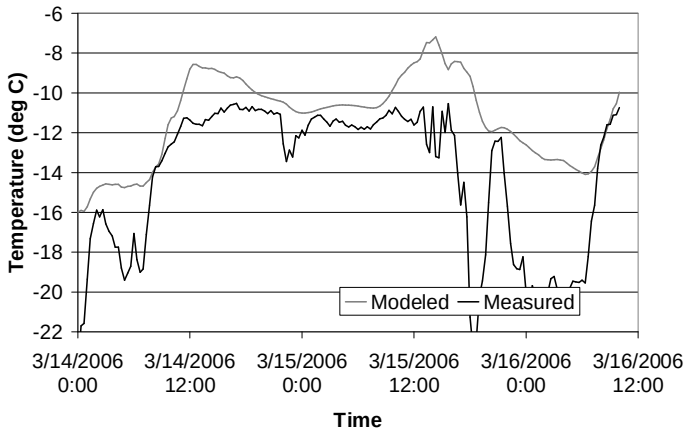

(b)

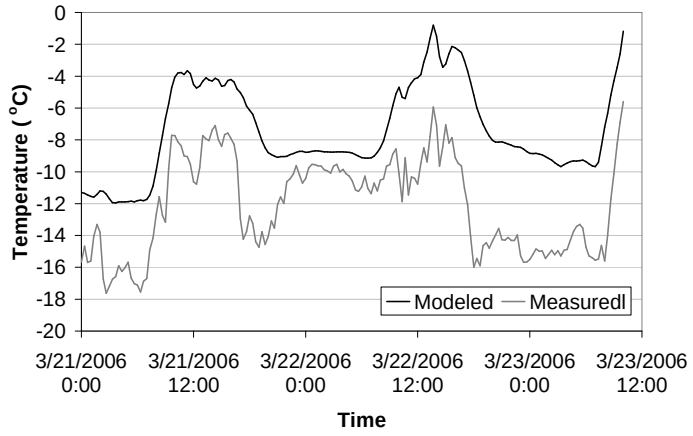

Figure 28. Comparison of modeled and measured snow surface temperatures during March 14 to 16, 2006 (a) and March 21 to 23, 2006 (b) on the south facing slope at the location of the weather station.

Although modeled values of temperature produce a smoother curve than measured values, they do indicate the trends of measured values and major spikes in temperature. During these two periods in March (Figure 28), measurable snow accumulated at both sites and covered upward facing instruments. On March 14, 2006 approximately 25cm of snow fell, and on March 21, 2006 approximately 5cm of snow fell. This new snow altered the surface conditions of the snowpack. As a result of this new snow, it is difficult to accurately determine the exact cause for error between the

modeled and measured temperatures; however, it is speculated that snow covering the radiometers may have caused the instruments to record higher values for incident long wave radiation. This same snow would have reduced the amount of measured incoming short wave radiation and effected lower modeled snow surface temperature. Because modeled temperatures were higher than measured values (Figure 28), the primary source of error in modeled snow surface temperature may have been incorrect values for long wave radiation. For the rock outcrop located at the south facing site, RadThermRT was able to more accurately calculate surface temperatures than for snow (Figure 29).

The measured incoming short wave and long wave radiation values used as input data for the period of March 21 to March 23 are presented in Figure 29. The daily peaks in long wave radiation were influenced by snow on the instruments. This snow likely warmed with increases in short wave radiation. In the following section on results from the 2006-2007 winter season, similar increases in long wave radiation were observed when no snow covered the instruments. These increases were attributed to the effects of surrounding terrain.

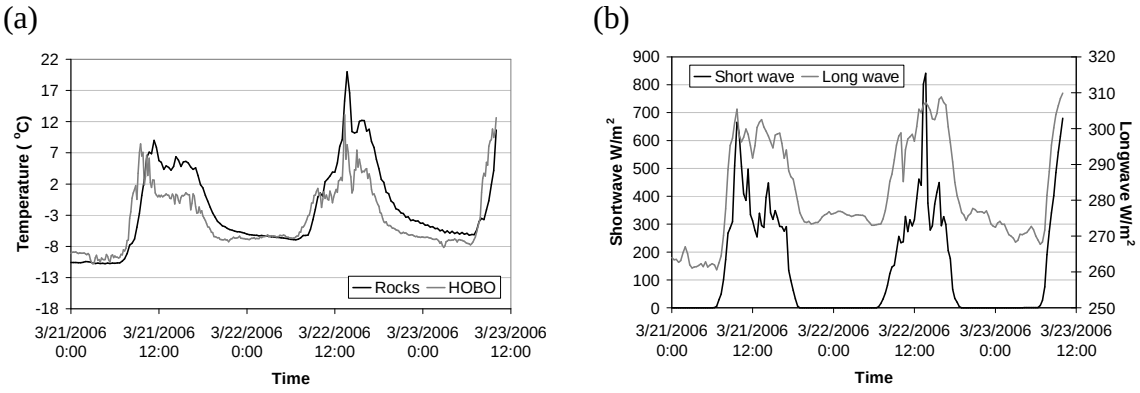

Figure 29. Comparison of modeled temperatures and measured temperatures on a rock surface with a HOBO thermistor/datalogger unit during March 21 to 23, 2006 on the rock outcrop at the south facing slope (a). Measured values for incoming short wave and long wave radiation during the same time period (b).

Mass Flux

Mass flux was continuously calculated for each surface element. A negative value indicates a loss of mass from the snowpack, and a positive value indicates a gain of mass (Equation 4). Such a gain of mass occurs in the form of condensation/deposition and is assumed to be evident as surface hoar. Quantitative measurements are difficult to obtain, and it was hoped that observations of surface hoar growth would correspond to periods of time when modeled mass flux values were positive. Surface hoar crystals of 1.5 mm were observed on March 23, 2006 at 11:00AM, and the YC Ski Patrol reported that these crystals began forming the evening between March 21 and 22. However, colder snow surface temperatures were recorded the following night when the modeled temperature values were much higher (Figure 28). For this period in March, a modeled mass flux with positive values did not correlate with observations of surface hoar growth (Figure 30). Because the long wave radiation input data were assumed to be high, they were reduced by 10% to demonstrate their potential influence. This change pushed parts

of the mass flux curve over zero as well as producing better results for temperature (Figure 30).

(a) (b)

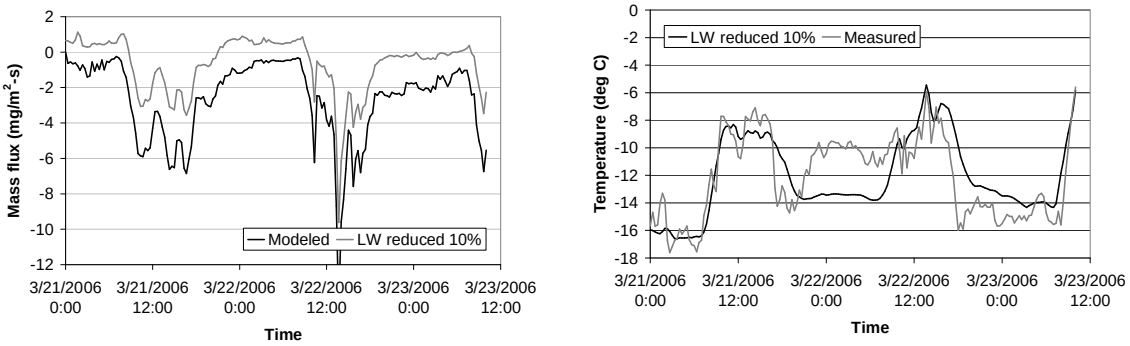

Figure 30. Modeled values for mass flux and snow surface temperature on the south facing slope (a). To investigate the effects of long wave (LW) radiation, the input values for incident LW radiation were reduced by 10% to account for snow accumulation on the radiometers. This change pushed mass flux into positive values when it is believed a layer of surface hoar formed. Using the same reduced input values of LW radiation, modeled values for snow surface temperature at the south facing slope have been plotted with measured values (b). Similar results were obtained for mass flux and temperature for the north facing slope.

2006-2007 Winter

Snow Surface Temperature at Weather Stations

Weather data from the 06/07 winter were significantly improved with help from the Yellowstone Club (YC) Ski Patrol as they worked to keep upward facing instruments mostly free of snow. These instruments were swept clean once a day; therefore, some inaccurate data from snowfall was possible for brief periods. As discussed for the previous winter season, it was believed that snow covering the radiometers was a significant source of error in calculating thermal conditions. During a storm, the temperature of new snow is often relatively close to air temperature. If such snow remains on a radiometer after a storm, the measured values of long wave radiation will

likely be representative of a potentially warmer, cloudy sky. In some scenarios the sky may be significantly colder; consequently, modeled values of snow surface temperature would be artificially high (Figure 31).

Solar data were available from the American Spirit weather station beginning January 26, 2007. Besides having a relatively clear view of the sky, this weather station had the advantage of being constantly swept clear of snow by wind. The problem of snow covered instruments was alleviated for solar data, but good long wave radiation data proved to be illusive and was measured at American Spirit weather station only from March 29, 2007 to April 12, 2007. The mostly unobstructed view of the sky was the key component for this station and allowed it to measure solar and LW radiation data without additional radiation inputs from surrounding terrain features. In addition to the effects of LW radiation, snow albedo was found to have a large effect on snow surface temperature.

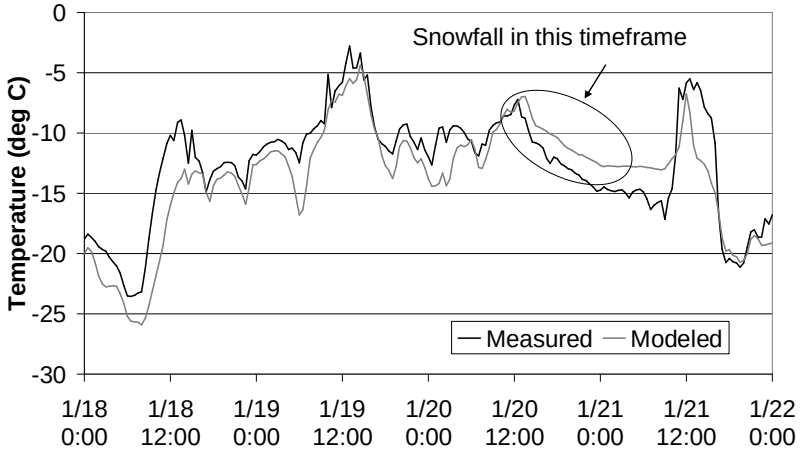

Figure 31. Measured values for snow surface temperature at the south site weather station were consistently warmer than modeled values except for the period of snowfall. These modeled temperatures were calculated using long wave radiation data from the north site and a snow albedo of 90% . The YC Ski Patrol reported snow covered instruments on the morning of January 21st from snow that fell the previous night.

Long Wave Radiation: Incident long wave (LW) radiation is used to calculate radiation exchange with the sky and the resulting heat flux. Because calculations of this heat flux include temperature to the fourth power, accurate measurements are critical for calculating snow temperature. As previously mentioned, radiometers needed to be kept clear of snow, but they also needed to be well located for good input data. Measured values of LW radiation are used to calculate sky temperature; therefore, only one set of incident LW data is needed for this project. Ideally three radiometers could have been available: one with an unobstructed view of the sky on a ridgetop, and one at each study site. The one on a ridgetop could be used for input data. Once the radiation exchange was calculated, modeled values of incident radiation could be compared to measured values at each site.

The effects of surrounding terrain on snow near the weather station at each site were apparently minimal, and sky temperature seemed to dominate the effects from LW radiation. The strong effect of sky temperature was seen in the close match between modeled values of incident LW radiation and measured values (Figure 32). The effects of surrounding terrain appeared to have a more noticeable effect on the radiometers. LW radiation recorded at the south site has noticeable peaks during the midday hours (Figure 32). These peaks seem to arise from the daily temperature spikes of surrounding terrain and the resulting increase in LW radiation emission.

(a) (b)

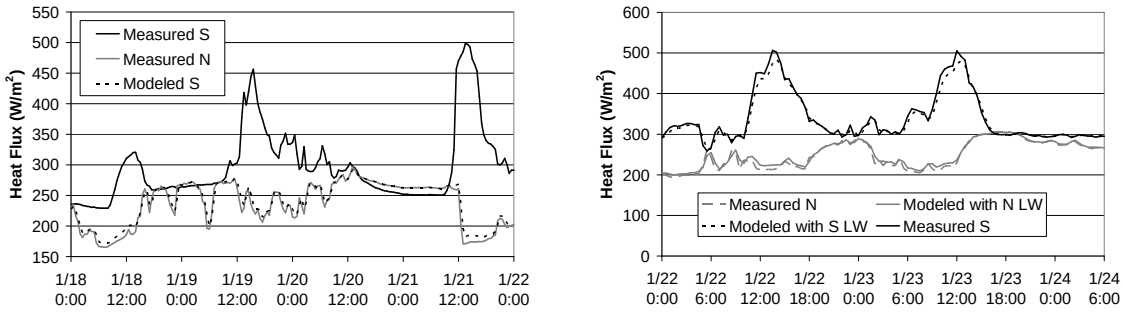

Figure 32. Each graph shows measured LW radiation at the south site (S) and the north site (N). The influence of terrain is seen in daily spikes in measured values from the south site. Modeled LW radiation incident to snow at the south weather station is shown in both graphs. LW input data included values from the N site (a) and both the N and S sites (b). Because the sky may have such a greater influence than terrain, modeled values of incident radiation differ little from the input values.

The strong solar warming of surrounding terrain likely increased the total LW radiation incident to the radiometer at the south-facing site to a greater degree than the snow underneath. The primary terrain feature of the south-facing site was a large section of steep rock (Figure 12) that was rarely covered in snow and sometimes 20°C warmer than nearby snow temperatures. To investigate the effects of local terrain, LW radiation from the north site was used to model the thermal conditions of the south site. Modeled incident and outgoing LW radiation for these rocks was plotted with the measured values of incident LW radiation from both sites (Figure 33). This south facing rock outcrop increases LW radiation measured by the radiometer, and it appears to increase LW radiation incident to snow surface to a much lesser degree. This result may have occurred for two reasons: the radiometer was placed over a meter above the snow surface, and the radiometer was placed level and not tilted in the orientation of the underlying snow.

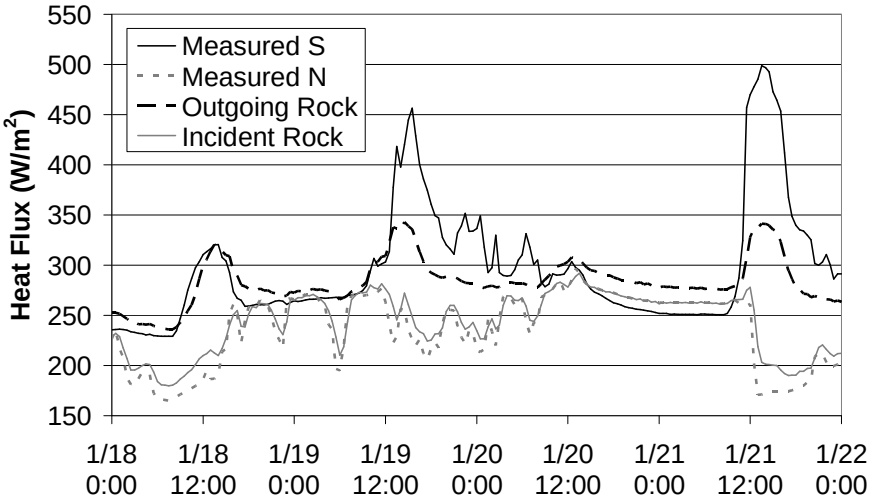

Figure 33. This graph shows the modeled LW radiation incident to snow at the weather station and rocks just above the weather station. Also plotted are measured values of LW radiation from the north and south weather stations. Outgoing LW radiation from the rocks appears to affect the incident LW radiation measured at the south weather station.

Modeled incident LW radiation for different snow surfaces was then investigated to further explore the effects of terrain. Four different elements of snow were chosen: one at the weather station (#5473), near large east facing trees (#2818), near the base of the rocks (#2137), and next to a sapling (#2946) (Figure 34). Differences in incident LW radiation calculated for these elements were less than expected (Figure 35), and similar results were seen in surface temperature and mass flux. Calculated values for mass flux during January 22-24, 2007 varied between these elements by a maximum of 0.93 mg/m^2-s. These results seem to suggest that the effects by terrain features on long wave radiation incident to the snow surface are overshadowed by the effects of atmospheric conditions.

Accurate input data for LW radiation are critical for the most accurate results for snow surface temperature. During most of the 06/07 winter, incident LW radiation data were measured at the north and south sites, and both were used as input data for modeling of the south site. To quantify differences between modeled and measured snow surface temperatures, mean absolute error was used. In all cases, using long wave data from the north site produced better results (Table 2 and Figure 36).

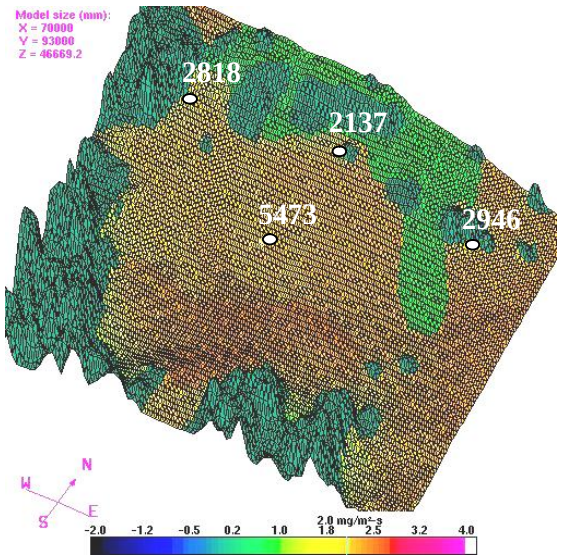

Figure 34. The image shows the relative location of elements used in Figure 35. Colors represent variations in mass flux in units of mg/m^2-s. Elements 5473 and 2137 had values of 2.0. Element 2946 has a value of 1.84, and element 2818 has the lowest value of 1.75

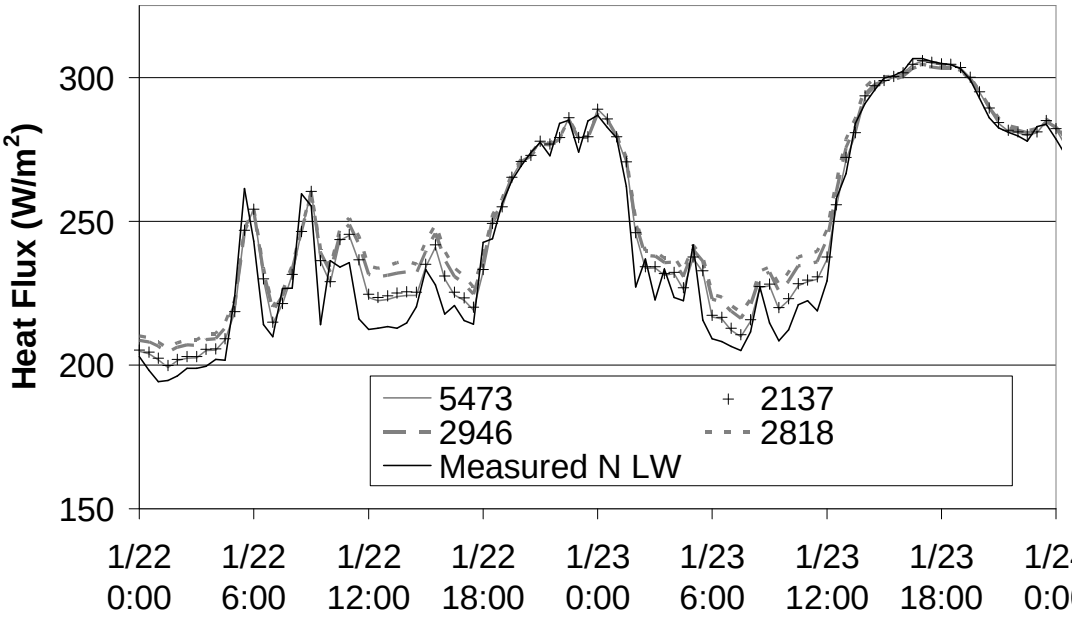

Figure 35. Incident long wave (LW) radiation for the south site is shown. Modeled values for selected elements (Figure 34) are plotted with the measured values from the north site (N). These measured values were used as input data. Element 5473 is located at the south weather station.

Use of LW radiation data from the north site continued for modeling of the south site until such data were available from the American Spirit weather station (Figure 37). It is unclear whether or not this American Spirit data provided an advantage. Because the radiometer from the north site was moved to the American Spirit weather station, a comparison of temperatures using LW data from both the north site and American Spirit was not possible.

Table 2. The mean absolute error was calculated for snow surface temperature values modeled for the south site with long wave (LW) radiation data from the south site and the north site. In each case modeled temperatures more closely matched the measured values when LW radiation data from the north site was used.

Dates	Using south LW data, mean absolute difference in degrees	Using north LW data, mean absolute error in degrees
Jan 18-21	2.57	1.92
Jan 20-22	6.12	2.26
Jan 22-24	4.76	2.13
Jan 27-30	9.92	6.62
Feb 2-4	3.27	1.16
Feb 19-21	3.06	1.74
Mar 16-18		0.94
Using LW data from the American Spirit weather station		
Mar 30 –Apr 1	2.60	
Apr 1-3	0.73	
Apr 3-5	1.77	

To investigate the effects of LW radiation on the north site, measured values for incident LW radiation were manually adjusted up and down by 5%. The resulting snow surface temperatures shifted up for increased LW values and down for decreased LW values (Figure 38). The average change in temperature was +/-1.3 degrees Celsius for the 5% changes in LW radiation.

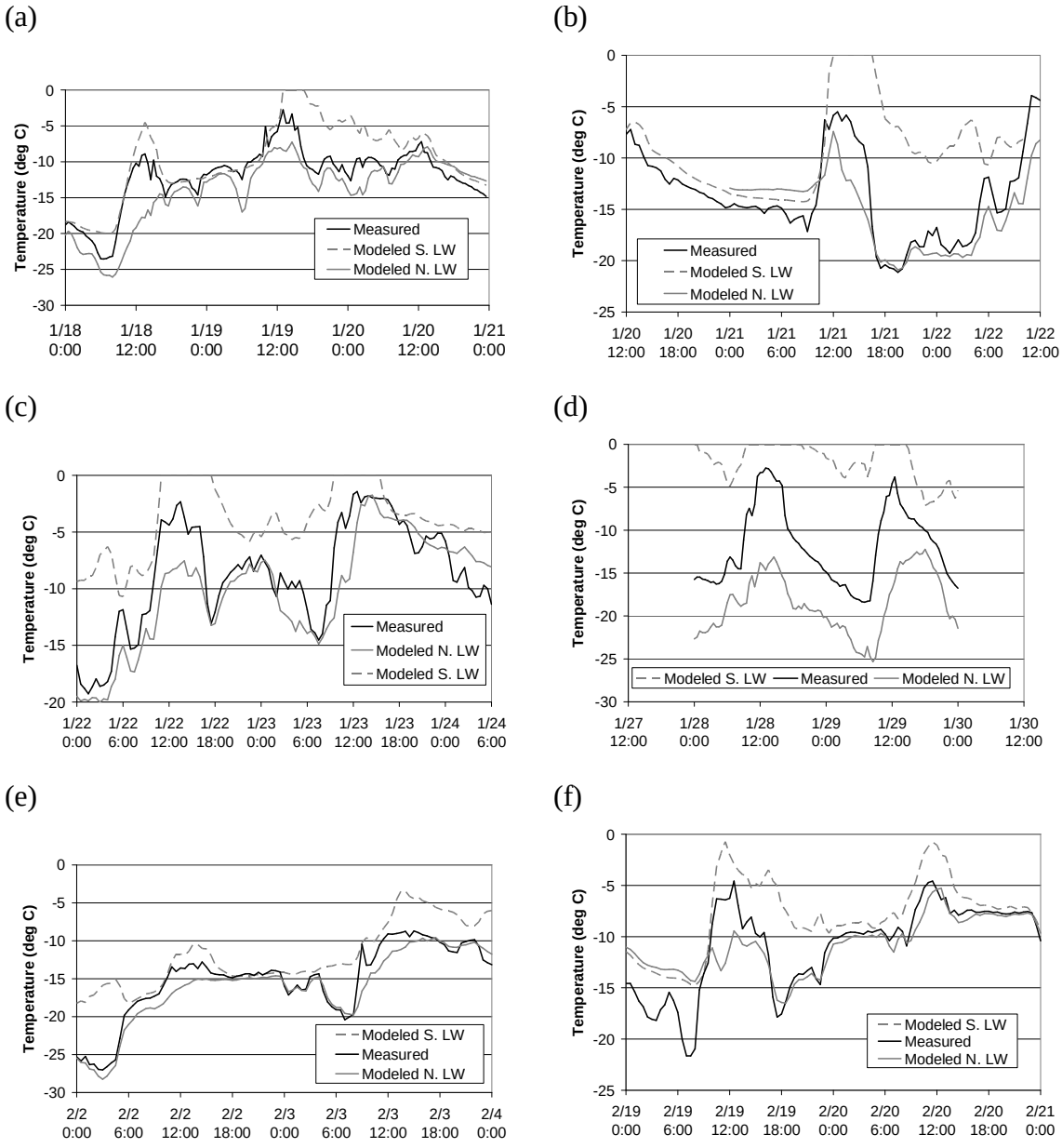

Figure 36. Each of these graphs shows the effects on modeled snow surface temperature for the south site using long wave radiation data from both sites. The reason for significant errors in graph (d) was undetermined. In graphs (a), (b), and (c), solar radiation data came from the south site. For graphs (d), (e), and (f), solar data came from the American Spirit station.

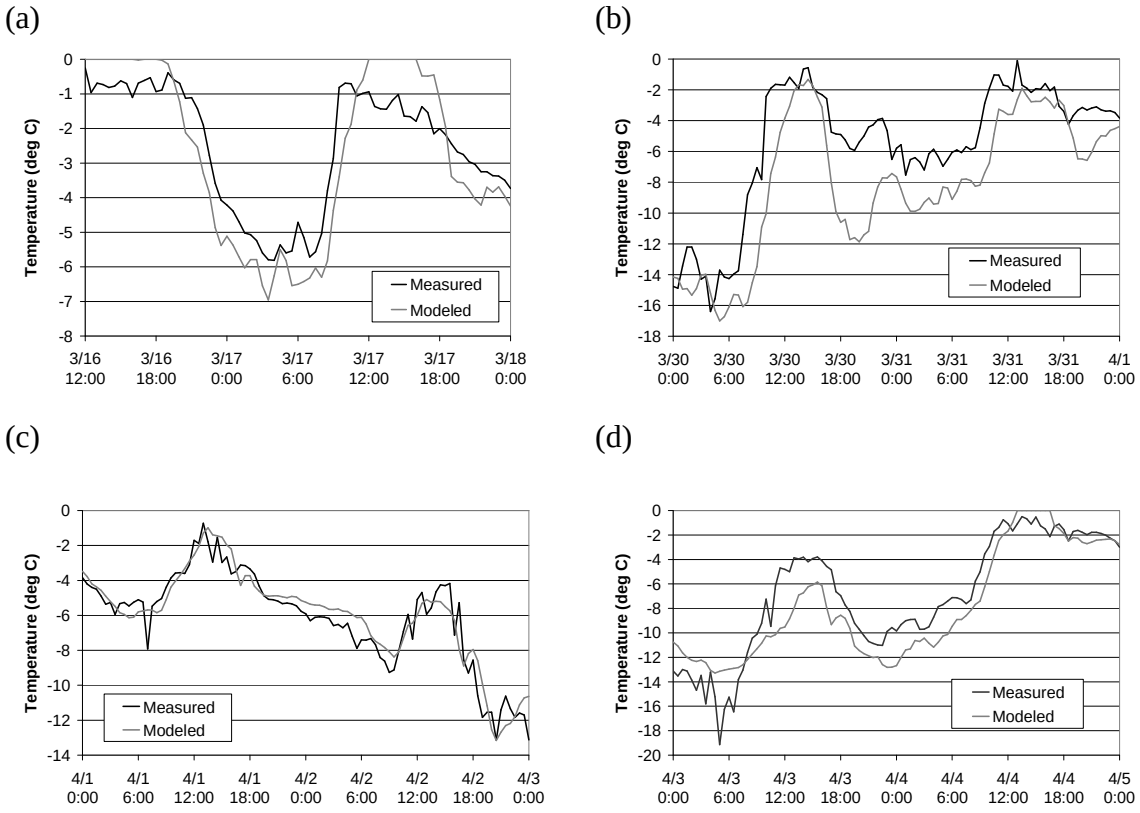

Figure 37. Each graph shows a comparison of modeled and measured snow surface temperatures for the south site. Long wave radiation data from the north site was used to produce graph (a) and long wave radiation data from the American Spirit station was used for (b), (c), and (d). Solar radiation data from the American Spirit station was used in all cases.

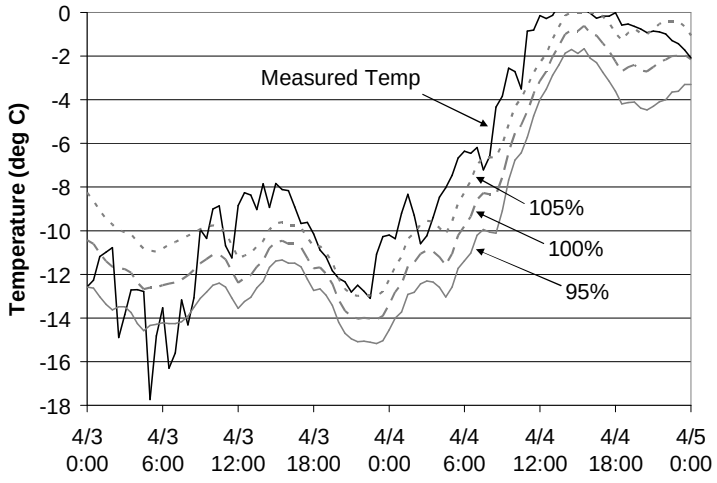

Figure 38. Modeled snow surface temperatures for the north site using 95%, 100%, and 105% of the measured incident long wave radiation at the American Spirit weather station.

Snow Albedo: Changes in snow albedo produce changes in temperature because the snow absorbs more or less solar radiation. This effect was most pronounced during midday hours when solar radiation was at a maximum. Snow albedo values of 99% typically led to snow surface temperatures colder than measured values during midday hours. In many cases an albedo of 90% produced the most accurate snow surface temperature values (Table 3). This effect occurred on model runs for January 18-22 (Figure 31), February 19-21 (Figure 39), March 30-April 1, and April 3-5 (Figure 40). The mean absolute error using a 90% albedo was lower in all cases than using a 99% albedo.

Table 3. Mean absolute errors in snow surface temperature for model runs using different albedo values.

Date of model run	99% Albedo	95% Albedo	90% Albedo
January 18-22 South Site	2.45		1.92
February 19-21 South Site	2.23		1.74
March 30-April 1 South Site	3.69		2.60
April 3-5 North Site	1.94	1.52	1.35

This result does not mean the actual albedo was 90%; instead, it means that this value modeled the most accurate snow surface temperatures, and more importantly it demonstrates the effects of albedo. This value may have compensated for some other unknown error in the modeling. One possible source of error could be the use of snow albedo in RadThermRT. It has been shown (e.g. Wiscombe and Warren, 1980; Morstad 2004) how snow albedo varies with such factors as spectral wave length, snow grain size, impurity concentration, solar zenith angle, snow density, snow depth, etc. In this work,

the albedo has been fixed through time and across space, and it has been applied in a broad spectrum manner. The specified albedo has been used regardless of the solar zenith angle and represents an average reflectance over the entire solar spectral band. These assumptions may not be correct in all cases.

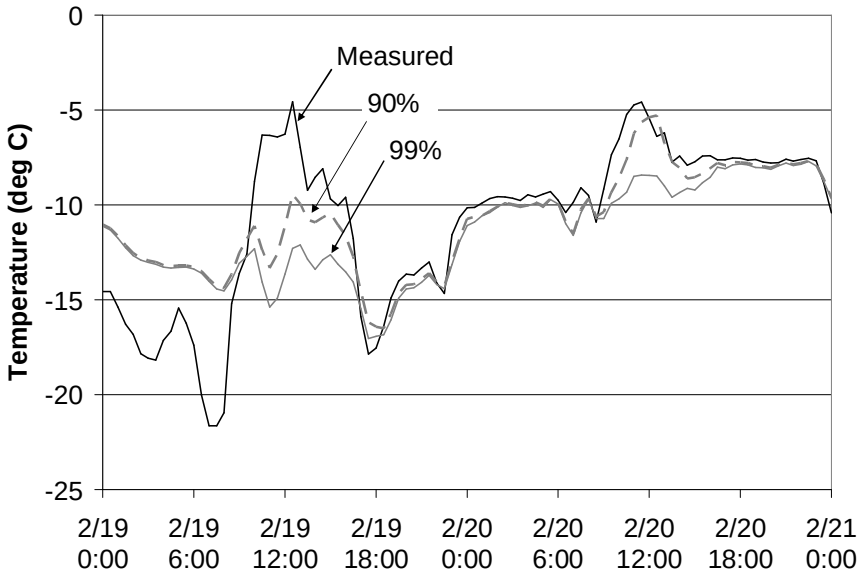

Figure 39. Snow surface temperature results for the south site showing the effects of different values of snow albedo.

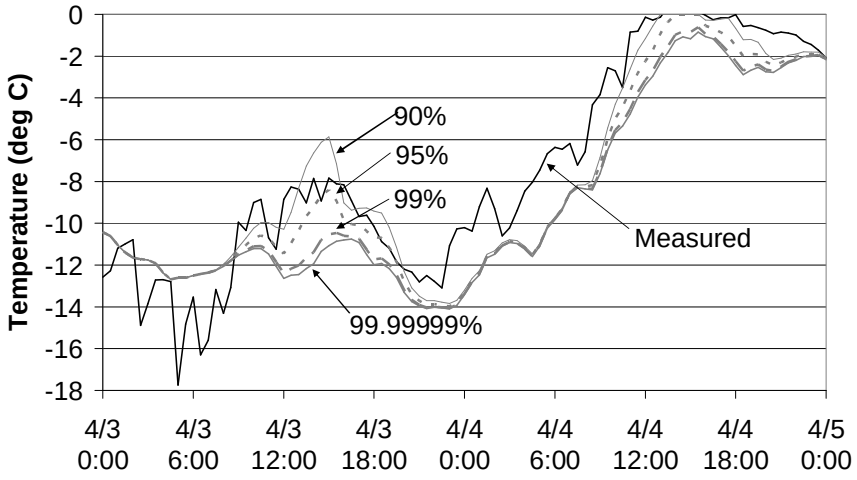

Figure 40. Snow surface temperature results for the north site showing the effects of different values of snow albedo.

Solar Radiation

Incident solar radiation for the north and south site was calculated using input data from the American Spirit station and compared with incident solar radiation measured on the slope (Figure 41). This comparison was done to check the accuracy of solar position, shadowing, and radiation reflection in RadThermRT. In most cases modeled solar radiation was less than measured, and it was thought that this artificially high input data was the reason snow albedo values reduced from 99% to 90% produced better snow temperature results. However, on April 3, 2007, modeled solar radiation was larger than the measured (Figure 41d), and again a snow albedo of 90% led to the best results for snow surface temperature than a higher albedo (Figure 42).

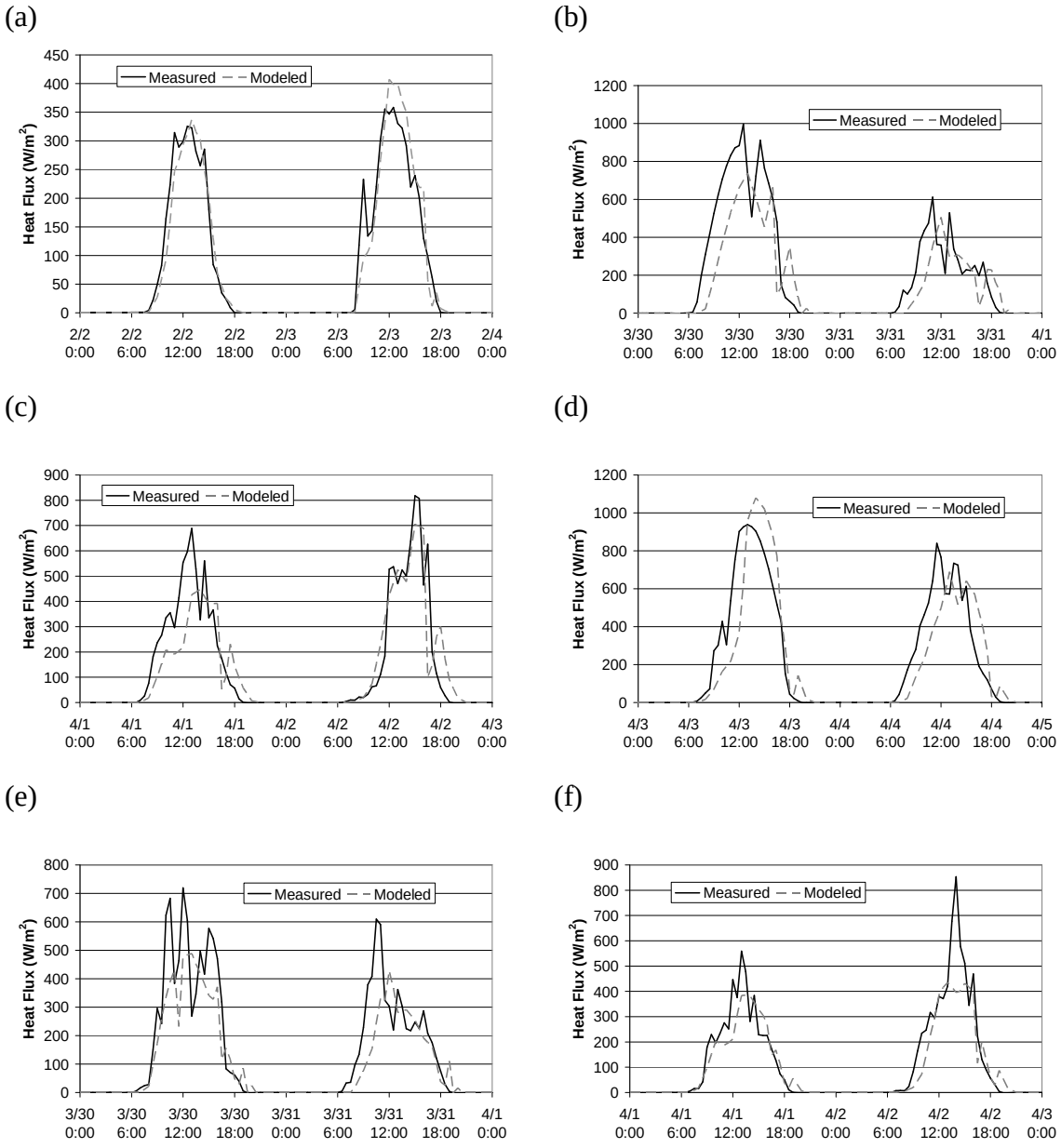

Figure 41. Modeled and measured results of incident solar radiation from the south site (a-d) and the north site (e, f). Measured values were recorded at the south site with an Eppley PSP and at the north site with a Li-Cor LI-200. Modeled values were calculated using input data from the American Spirit station with an Eppley Laboratories PSP.

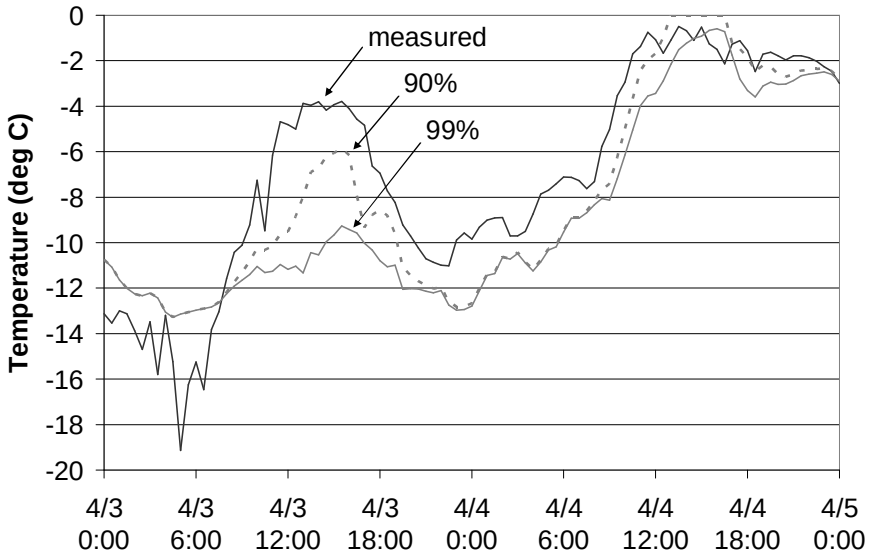

Figure 42. Snow surface temperature for the south site. Modeled values are shown for snow albedo values of 90% and 99%. On 4/3 the modeled values for solar radiation were higher than the measured values (Figure 41d), and it was suspected that higher values of albedo would have produced better results by compensating for the artificially high values of solar radiation. This was not the case.

Core Temperature

The lower boundary value of the snow cover is a set temperature called the core temperature. For a snow pack, this is often assumed to be zero degrees Celsius, but it is not always true. The ground surface at both the north and south sites is covered in talus, and temperatures below freezing were commonly recorded. During January 18-20, the average snow temperature at the ground interface was -9.5 degrees Celsius, and for one model run this value was set as the core temperature. Only minor differences in snow surface temperature were seen between this model run and one using 0 degrees Celsius as the core temperature (Figure 43). The mean absolute difference between temperature values from the two model runs was 0.14 degrees Celsius.

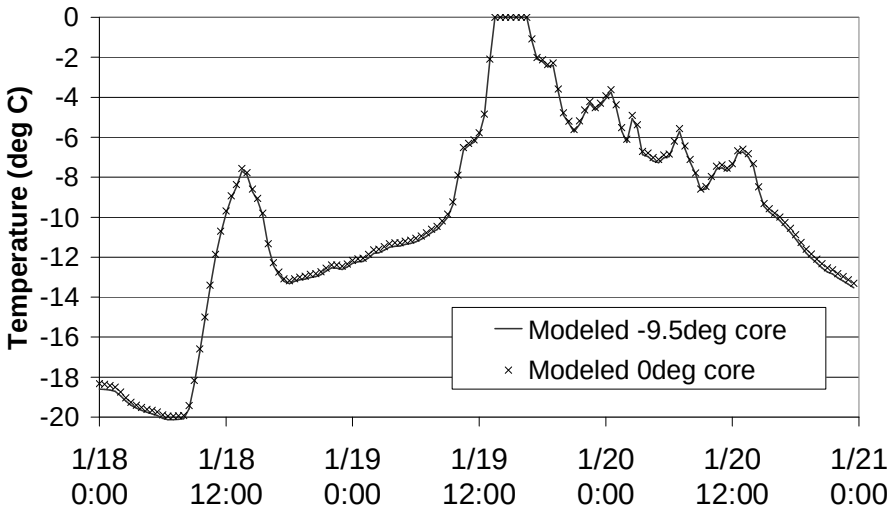

Figure 43. Modeled snow surface temperatures for the south site using core temperature values of 0 and -9.5 degrees Celsius.

Settings for Ray Tracing Algorithm

Settings for the ray tracing algorithm were reduced from medium to low to reduce the computation time. Differences between these settings are found in Table 1. While some differences for select elements would be expected between medium and low settings, the differences in snow temperature at the weather station were minimal (Figure 44). Similar results were achieved during other model runs.

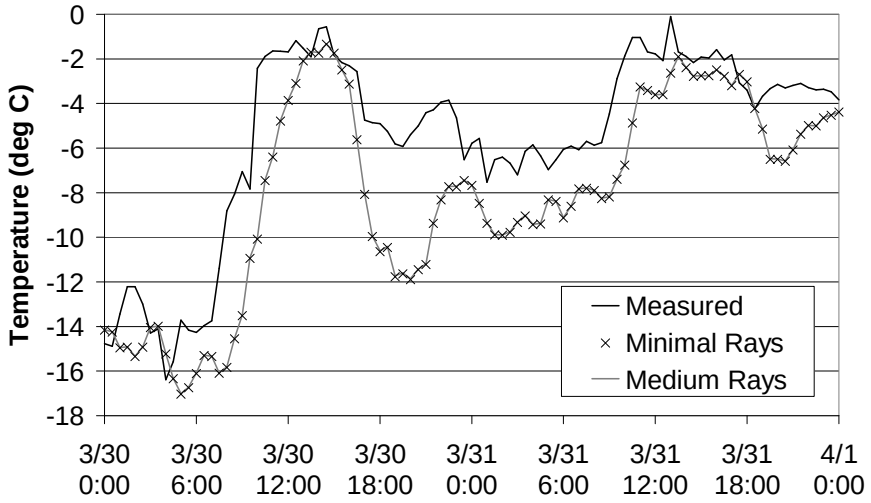

Figure 44. Modeled snow surface temperature at the south weather station using minimal and medium settings for the ray tracing algorithm.

Relative Humidity

Relative humidity (RH) was varied in the model to investigate its effects on snow surface temperature. For simplicity, relative humidity in the weather file was varied from the measured values to constant values of 95% and 5%. While these values of RH were held constant, changing air temperatures caused absolute values of humidity to vary. The sensible heat flux was unaffected, as the heat transfer coefficient used in RadThermRT is not a function of humidity; however, changes in humidity altered the mass flux which directly altered the latent heat flux (Figure 45). As expected, high humidity increased the mass flux and snow surface temperature. Low humidity had the opposite effect where the snow surface sublimated while temperature decreased. Between January 22 and 24, the maximum mean difference in snow surface temperature between weather with 95% and 5% RH was 5.9^0C and the mean absolute difference was 3.1^0C.

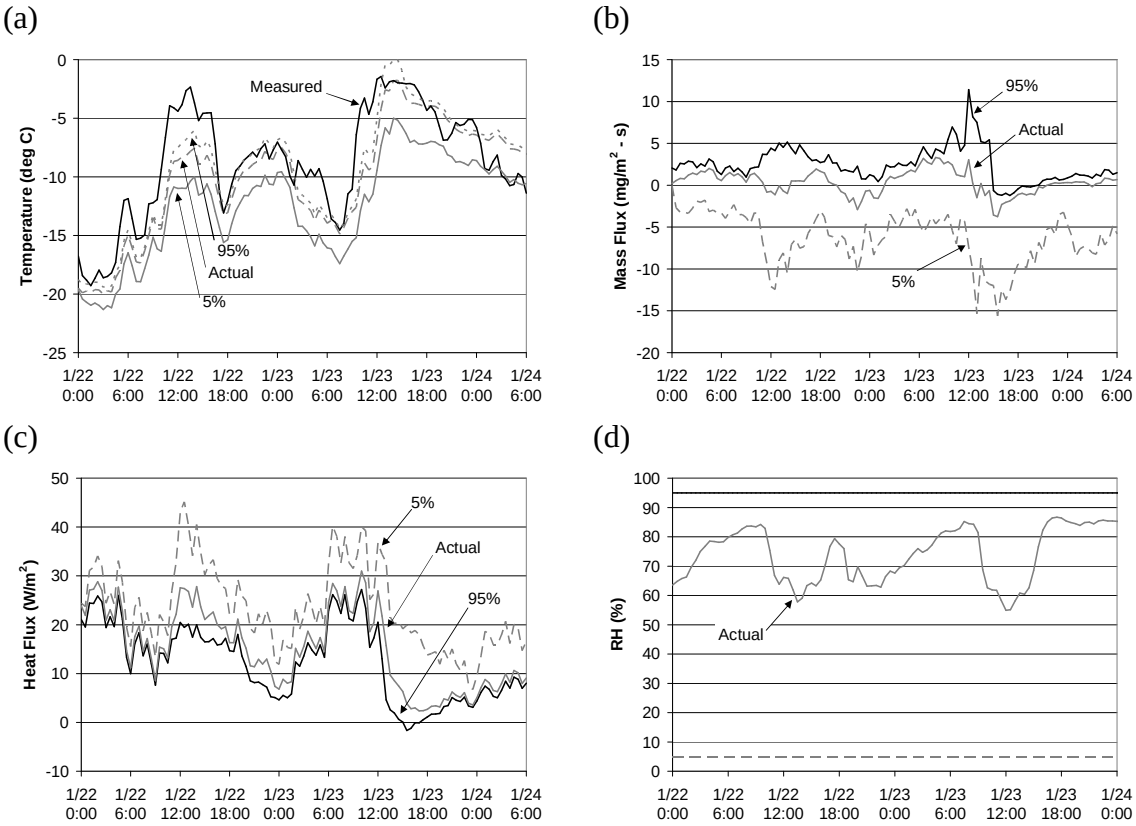

Figure 45. For the south site three different inputs for relative humidity were used: a constant 5%, the Actual measured values, and a constant 95%. Changes in relative humidity on the south site in January 2008 affected snow surface temperature (a), mass flux (b), and the convective heat flux (c). Positive heat flux is heat added to the snow. Measured relative humidity and the artificial constant values of 95% and 5% are plotted in (d)

Wind

Wind was also varied to investigate its effects on snow surface temperature, and similarly to changes in humidity, wind altered the convective heat flux (Figure 46). Both the sensible and latent heat fluxes were affected, as each is a function of wind speed. Wind values in the weather file were varied between 0 m/s and 10 m/s and held constant through each model run. Because the air temperature was warmer than snow surface temperature during this time period, increases in wind increased the convective heat flux to the snow and the snow surface temperature. The effect on mass flux varied. During

conditions favorable for a generally negative mass flux (sublimation), higher winds increased sublimation. During conditions favorable for a generally positive mass flux (deposition), the effect of wind speed becomes more difficult to generalize. Additionally, it becomes difficult to surmise in what form this deposition will take. Two possible forms of deposition are surface hoar and rime.

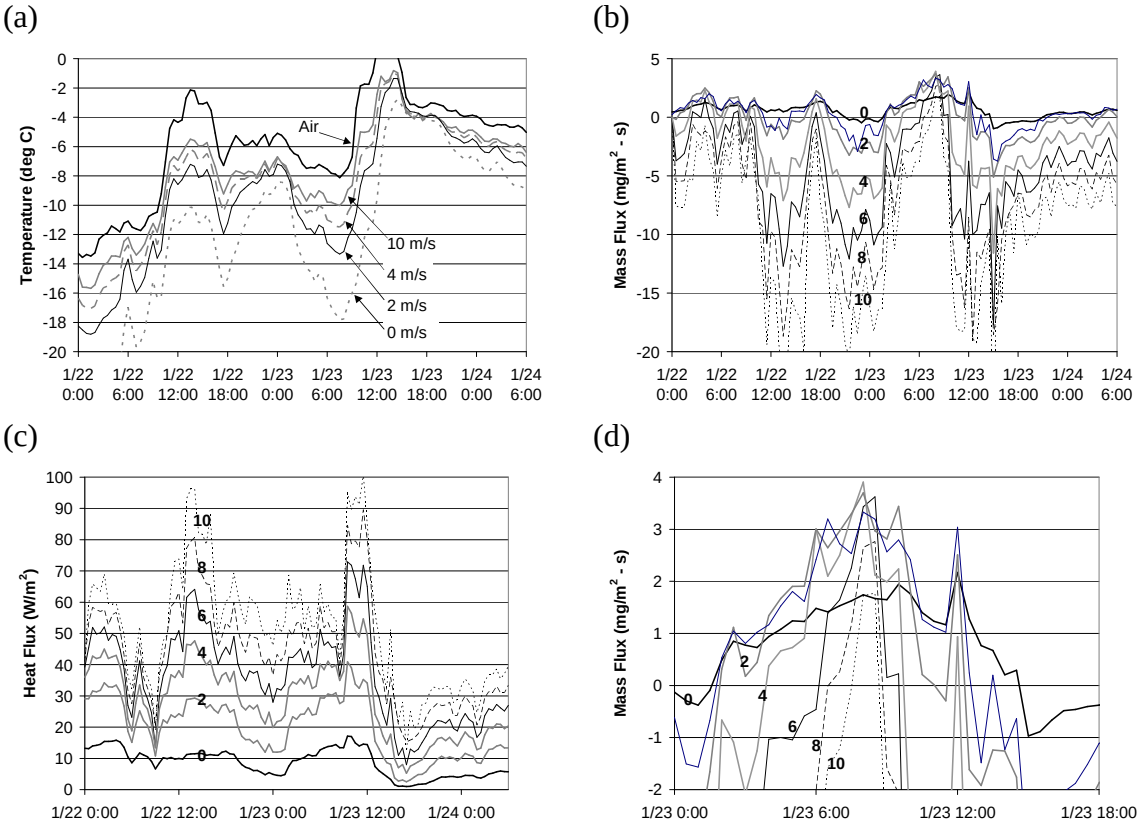

Figure 46. Changes in wind on the south site in January 2008 affected snow surface temperature (a), mass flux (b), and the convective heat flux (c). A section of the mass flux plot for the day of January 23 has been plotted on a different scale (d) to show the effects of wind speed on positive mass flux. Positve heat flux is heat added to the snow.

Albedo Effects across Terrain

As snow albedo was varied, resulting temperature changes on surrounding terrain were investigated. Three features were studied: a south facing rock outcrop, an east

facing tree, and a north facing tree. Each of these locations contained a stand-alone thermistor/datalogger unit with the thermistor taped to the rock face and the trunk of each tree. The accuracy of this measured temperature data is undetermined, but it assumed to be a reasonable representation for these terrain features. This temperature data has been compared with modeled temperature results from RadThermRT. Decreasing albedo allowed the snow surface to reflect less and absorb more solar radiation, and the snow experienced higher temperatures (Figure 47). With a higher temperature, the snow surface emitted more LW radiation. Surrounding terrain then received more LW radiation and less reflected solar radiation. RadThermRT provides a means to investigate these effects.

The south facing rock outcrop experienced a decrease in temperature, and it is assumed this occured because it received less reflected solar radiation (Figure 47). Similarly, the east facing tree experienced a decrease in temperature, presumably for the same reason (Figure 48). The temperature of these two features is strongly affected by direct solar radiation.

The effects on temperature of a north facing tree were also investigated, and the opposite situation occurred (Figure 48). A decrease in snow albedo, which produced higher snow temperatures, led to an increase in temperature of the north facing tree. Because it is north facing, this tree does not receive any direct solar radiation; instead, it receives diffuse solar radiation and reflected solar radiation. In calculating reflected solar radiation, RadThermRT assumes all elements are a Lambertian surfaces reflecting radiation equally in all directions. In reality, snow displays a strong forward scattering,

especially for high zenith angles (Rees 2006). For a north facing tree on a south facing slope, this property means much of direct solar radiation reflected off the surrounding snow would be directed away from the tree. For this reason, such a tree would be less affected by reflected solar radiation than other terrain features.

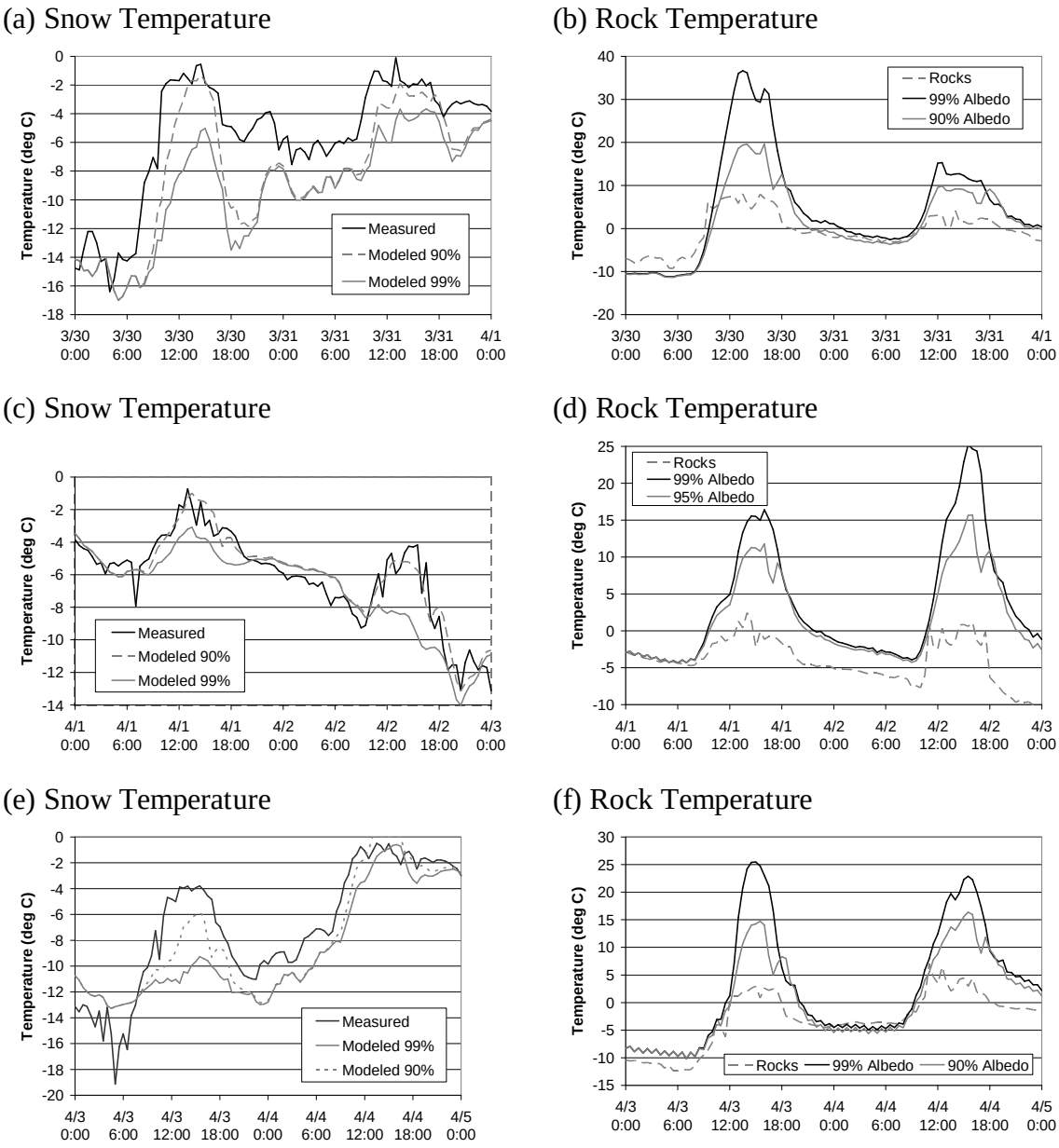

Figure 47. Snow temperature and rock temperature at the south site during March 30, 2008 to April 5, 2008 for varied snow albedo.

(a) East Facing Tree Temperature

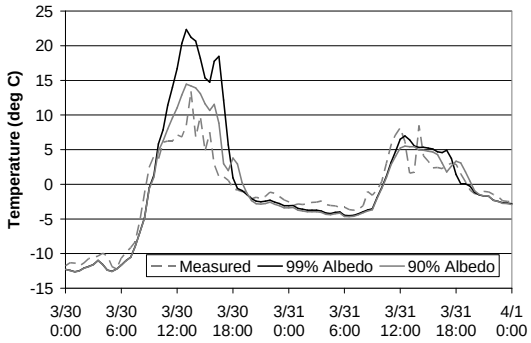

(b) North Facing Tree Temperature

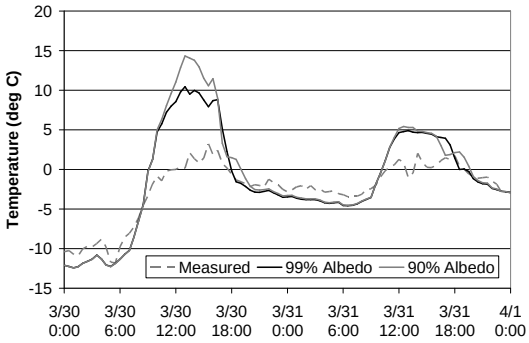

(c) East Facing Tree Temperature

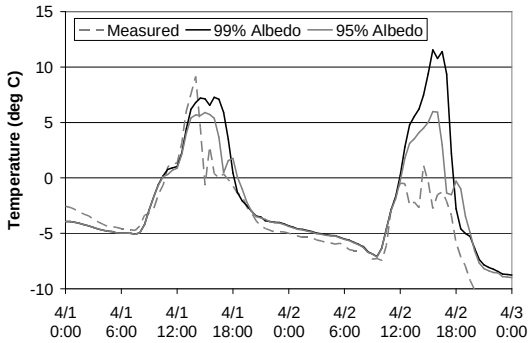

(d) North Facing Tree Temperature

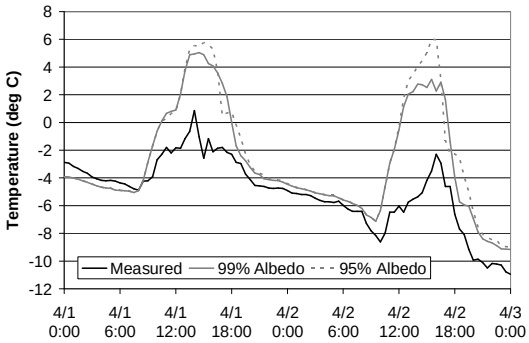

(e) East Facing Tree Temperature

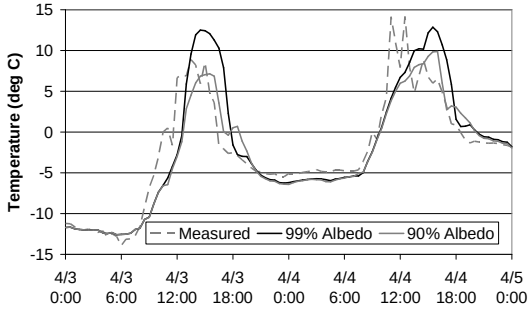

(f) North Facing Tree Temperature

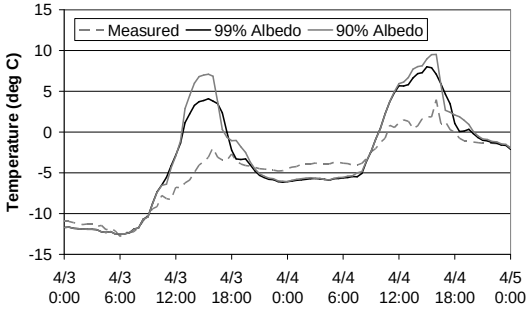

Figure 48. East and north facing tree temperatures at the south site during March 30, 2008 to April 5, 2008 for varied snow albedo.

Mass Flux

Föhn [2001] recorded mass flux values in the field, including those from surface hoar deposition (Table 4). Lightweight plastic pans were buried in the snow with an electronic scale placed under them to measure changes in mass. These changes were recorded twice a day and covered one 8 hour day period and one 16 hour night period.

Table 4. Average field values of mass flux recorded by Föhn [2001].

Average Mass Flux (mg/m^2-s)	Time Period
2.17	16 hr night
2.31	24 hr day & night
4.77	16 hr night
2.6	8 hr day

Because mass flux values from this study were averaged over extended periods, they do not represent the peak values. It is unclear to what magnitude the peak values may have reached. These average values have a comparable order of magnitude with peak values for the south and north site calculated in RadThermRT. Correlations with surface hoar observations (Table 5) also suggest mass flux calculations in RadThermRT have the correct sign. Positive mass flux values should correspond to surface hoar deposition or growth. Because snow surface temperature and mass flux are key variables in the surface energy balance, it is supposed that accurate values for snow surface temperature should indicate accurate mass flux results (Figure 49).

During four periods in January and February, mass flux was modeled for the north site at times when surface hoar deposition and growth occurred (Figure 49 and Figure 50). In three of these cases, either the 48 or 32 hour average mass flux was a positive value.

Table 5. Recorded observations of surface hoar crystals by the YC Ski Patrol during 2007.

Date	South Site Surface Hoar Observation	North Site Surface Hoar Observation
1-22	0.5 mm	1.0 mm
1-23	1.0 mm	1.0 mm
1-24	1.5 mm	1.5 mm
1-25		2.0-3.0 mm
1-26		2.0-3.0 mm
1-29		2.0 mm
2-10	0.5-1.0 mm	
2-17	0.5 mm	
2-18	0.5 mm	1.0 mm
3-4	4.0 mm	1.0-3.0 mm
3-5	2.0 mm	3.0 mm
3-6	2.0 mm	2.0 mm
3-7		3.0 mm
3-16	2.0 mm	
3-20		1.0 mm
3-21		0.25-0.5 mm
3-24		
3-29	0.5-1.0 mm	
4-8		1.0-2.0 mm

(a) South Site Mass Flux
Average = 0.36 mg/m^2-s

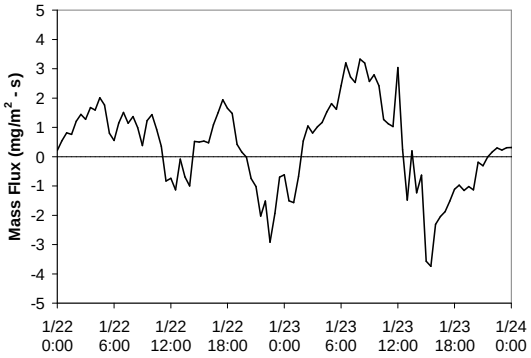

(b) South Site Snow Surface Temperature

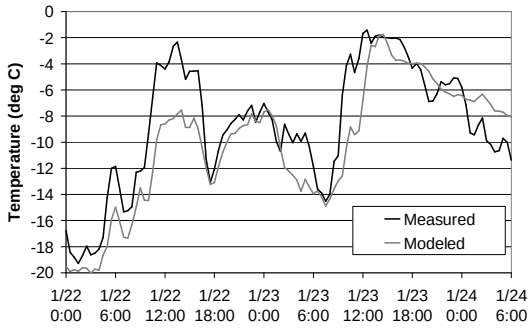

(c) North Site Mass Flux
Average = 1.4 mg/m^2-s

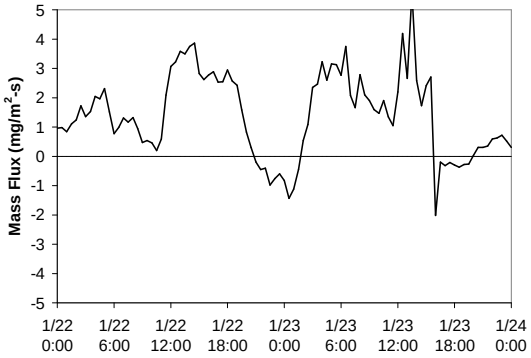

(d) North Site Snow Surface Temperature

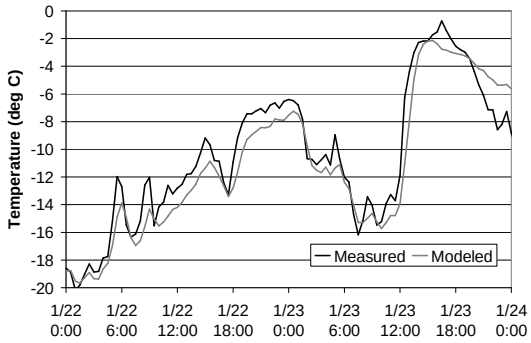

(e) South Site Mass Flux
Average = -5.4 mg/m^2-s

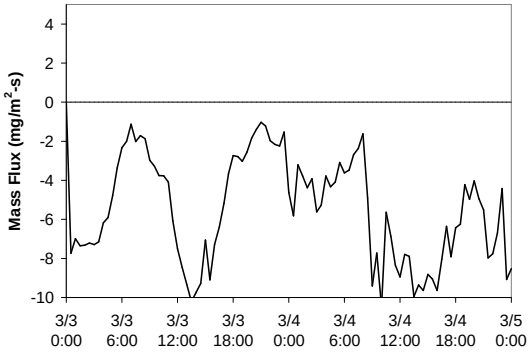

(f) South Site Snow Surface Temperature

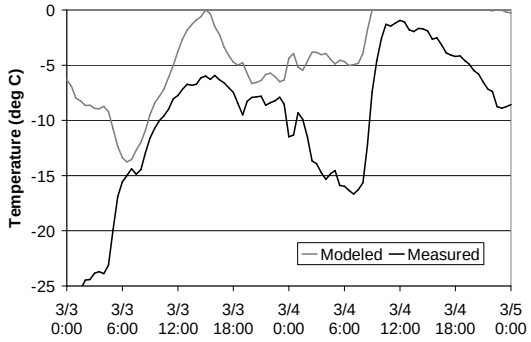

Figure 49. From January 22-24, 2007 at both the north and south sites surface hoar deposition and growth was recorded by the YC Ski Patrol. Modeled snow surface temperatures matched well with measured values (b,d), and modeled values of mass flux reached positive values (a,c). From March 3-5, 2007 surface hoar deposition was recorded at the south site, but modeled values were all negative (e), and modeled surface temperature did not match with measured temperatures (f).

(a) North Site Mass Flux (1.33 deg C)
Average = 0.99 mg/m^2-s

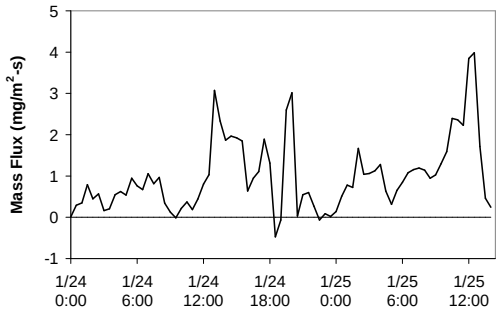

(b) North Site Mass Flux (1.08 deg C)
Average = -0.85 mg/m^2-s

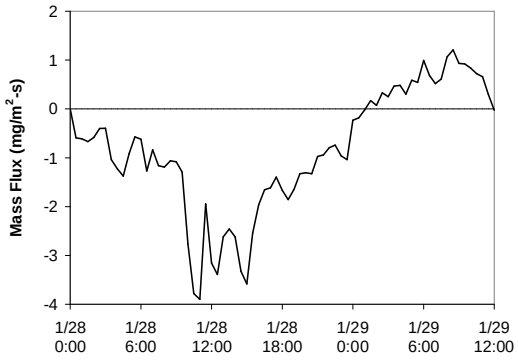

(c) North Site Mass Flux (0.91 deg C)
Average = 0.91 mg/m^2-s

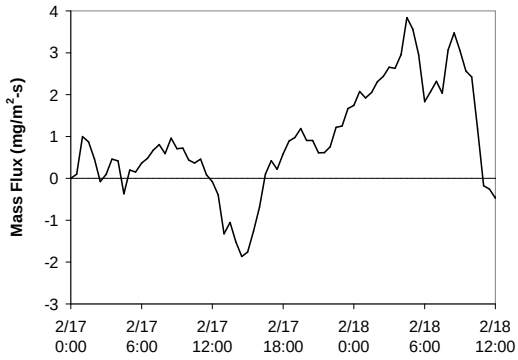

Figure 50. Mass flux results for the north site are plotted during periods of time when surface hoar deposition and growth was recorded by the YC Ski Patrol. For each time period, surface hoar was observed near the end of the plot. The mean absolute error for modeled surface temperature results is given in parentheses.

In the fourth case, significant sublimation followed by deposition caused the average mass flux to be negative; however, the model indicated a positive mass flux for the 10 hours prior to the observation of surface hoar. During five periods in January, February, and March, mass flux was modeled for the south site at times when no surface hoar was observed (Figure 51). In each of these cases, either the 48 or 32 hour average mass flux was negative.

(a) South Site Mass Flux (2.00 deg C)
Average = -0.43 mg/m^2-s

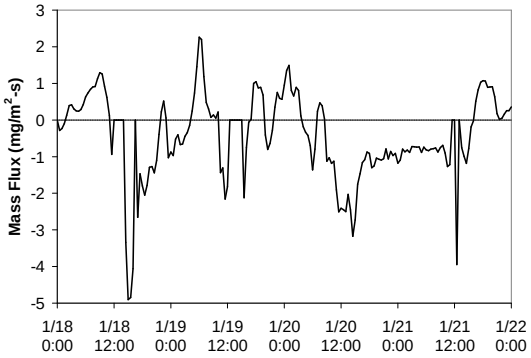

(b) South Site Mass Flux (1.16 deg C)
Average = -1.77 mg/m^2-s

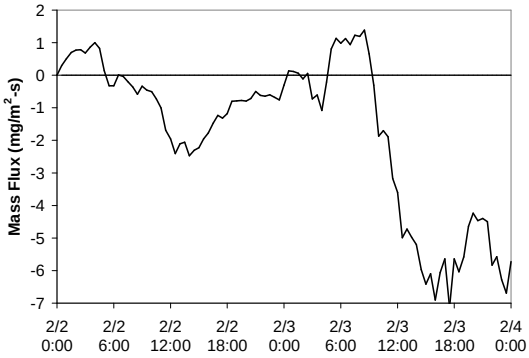

(c) South Site Mass Flux (1.74 deg C)
Average = -2.88 mg/m^2-s

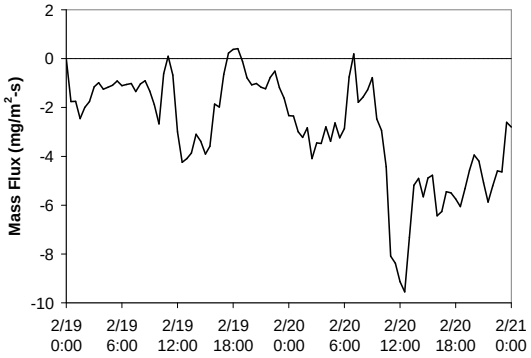

(d) South Site Mass Flux (0.94 deg C)
Average = -4.53 mg/m^2-s

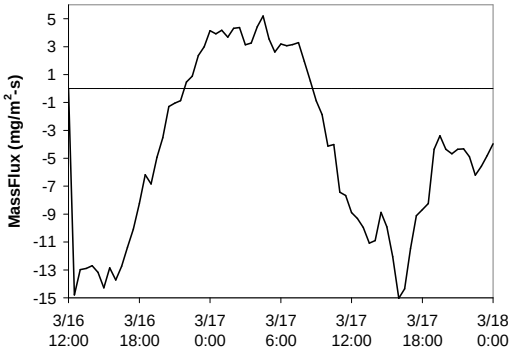

(e) South Site Mass Flux (2.60 deg C)
Average = -1.63 mg/m^2-s

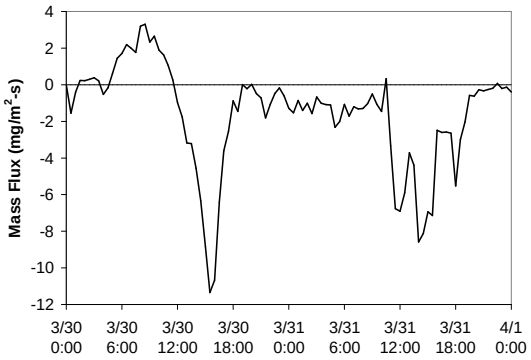

Figure 51. Mass flux results for the south site are plotted during periods of time when surface hoar deposition and growth was NOT recorded by the YC Ski Patrol. The mean absolute error for modeled surface temperature results is given in parentheses.

On January 24, 2007 the YC Ski Patrol observed 1.5mm surface hoar crystals at the south site, and they noted "surface hoar crystals larger in the shade downhill from station." Modeled conditions for the previous day reinforced this observation with larger values of mass flux and colder surface temperatures near element #10130 (Figure 52 and Figure 53). From January 23 at 0000 to January 24 at 0600, the average mass flux for element #5473 at the weather station was 0.31 mg/m^2-s. The average mass flux for element #10130 downhill of the weather station was 0.48 mg/m^2-s, and the average mass flux for element #7468 next to east facing trees was 0.00 mg/m^2-s. A similar trend for these three elements was seen in snow surface temperature with colder temperatures associated with higher values for mass flux.

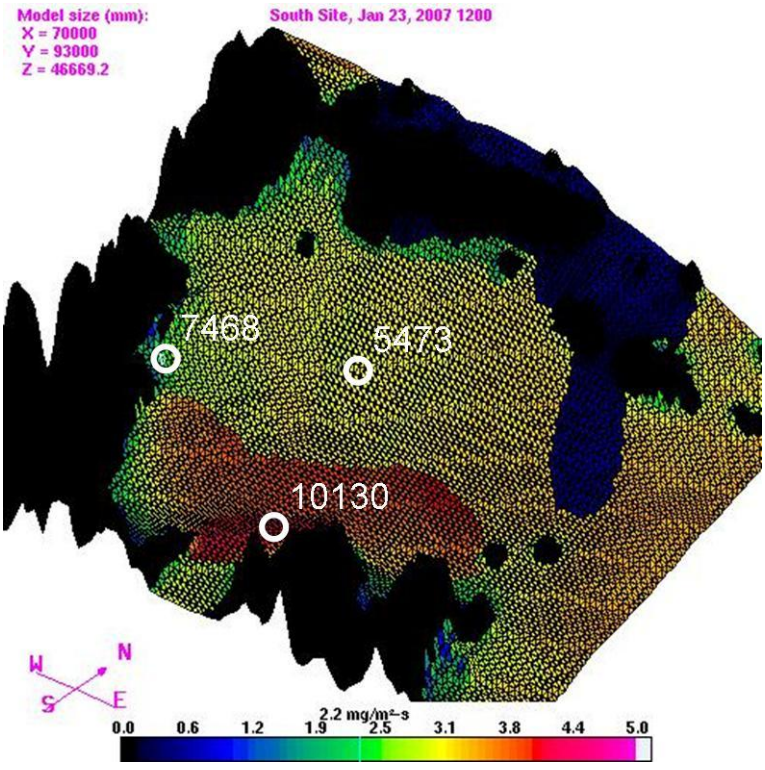

Figure 52. This image of the south site shows variations in mass flux on January 23, 2007 at 1200. The following day larger surface hoar crystals were noted on lower portions of the slope in the same area where mass flux values are highest. The locations of three elements are noted on the image.

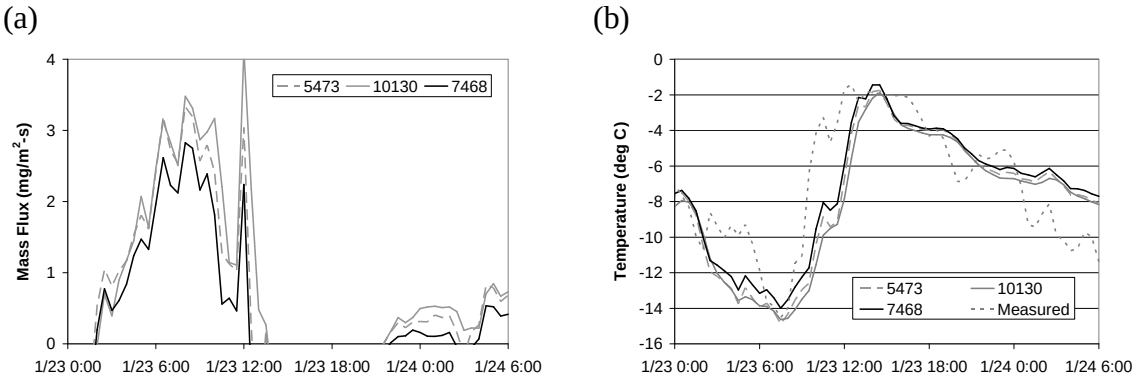

Figure 53. Modeled values of mass flux (a) and snow surface temperature (b) are plotted for three different elements at the south site.

Variations in size of surface hoar crystals present on the south site on January 23 and 24, 2007 are unknown except they were larger near element 10130 than near element 5473. Additionally, it is unknown how variations in mass flux would correspond to variations in surface hoar deposition and growth. Variations could be expected in size, shape, or spacing between crystals. More importantly the ability to model variations in mass flux has been shown and the location of these variations generally corresponds with recorded observations.

CHAPTER 5

CONCLUSIONS AND RECOMMENDATIONS

A first principles energy balance model, RadThermRT, has been used to calculate snow surface temperature and mass flux. Because this temperature plays a significant role in snow metamorphism and weak layer formation, the ability to accurately calculate snow surface temperature using meteorological and topographic data has important implications. RadThermRT has also been used to calculate variations in the snow surface energy balance across terrain, and these variations were evident changes in temperature and mass flux. Variations in temperature have also been seen across different terrain elements having different material properties.

Modeled surface temperatures for different elements have been compared to measured values. Initially, modeled temperatures did not match the measured temperatures very well, but better results were obtained during the 06/07 winter season when better long wave radiation data were recorded. The YC Ski Patrol improved this data by keeping the radiometers mostly free of snow. Additional improvements came from using LW data at the north site for modeling of the south site, and later using data from the north radiometer which had been moved to the top of the American Spirit lift. The purpose of measuring LW radiation for this project was to calculate sky temperature. RadThermRT is then used account for the effects of terrain and vegetation. Poor results were obtained when the LW radiation input data included the effects of both the sky and surrounding terrain.

LW data from the north site were probably less affected by terrain than data from the south site, and data from the American Spirit lift were even less affected by terrain. While terrain appeared to strongly affect LW radiation received by the radiometer on the south site, it did not appear to affect the snow surface as strongly at the weather station. The primary reason for this difference may be the positioning of the instruments because snow is nearly a black body for LW radiation and should absorb most of this emitted radiation if the snow surface is oriented such that it faces the emitting surface to some degree. Orienting the radiometers parallel to the slope may provide LW data more representative of LW radiation received by the underlying snow for comparison with calculated values of incoming LW radiation at that location. Accurate calculations of sky temperature were required to accurately calculate snow surface temperature, and the best means of obtaining such sky temperature is by placing a radiometer with an unobstructed view of the sky.

Aside from obtaining good input data for LW radiation, setting the snow albedo to 90% also improved results for snow surface temperature. More importantly, albedo was shown to have a large effect on snow temperature and the temperature of surrounding terrain. The effects of albedo were most apparent during midday hours of peak solar radiation. The modeling of direct and reflected solar radiation appeared to work well. When solar data were used from the American Spirit lift, modeled solar radiation for a site closely matched solar radiation measured at that site. Core temperature did not noticeably affect snow surface temperature results. Wind and relative humidity data were assumed to be accurate, but they were varied to investigate their effects on temperature.

As expected they had direct effects because convection is a function of both wind and humidity.

Variations across terrain in both temperature and mass flux were shown. Temperature variations were shown over different terrain elements such as snow and rock, and over different elements of snow experiencing varied levels of direct solar radiation. Additionally, some variations in snow temperature and mass flux were attributed to variations in LW radiation. Snow with a clear, north facing view of the sky experienced different thermal conditions from snow with an obstructed view of the sky.

Terrain models were built with both USGS topographic data and LIDAR topographic data. Terrain models built with LIDAR data allowed an investigation of terrain effects at a much smaller scale than terrain models built with USGS data. The larger scale variations were seen in previous work [Adams et al. 2004b]. In this work temperature results from models built with LIDAR data and USGS data were compared and very closely matched. Elements chosen in the LIDAR built model were located in generally open locations where the effects of local terrain were at a minimum.

The effects of snow albedo on surrounding terrain were also investigated. As albedo was changed artificially, snow temperature and reflected solar radiation changed. Terrain elements heavily influenced by direct solar radiation appeared to be more heavily affected by changes in reflected solar radiation as albedo changed. Terrain elements shaded from direct solar radiation appeared to be more heavily affected by changes in snow surface temperature and the resulting changes in emitted LW radiation.

Lastly, mass flux values were compared to measured ones from Föhn [2001], and peak modeled values had the same order of magnitude as the average measured ones. The YC Ski Patrol observed surface hoar deposition and growth throughout the 06/07 winter season. Mass flux was calculated reasonably well during these noted periods because it was generally positive and its peak values were the correct order of magnitude for surface hoar. On one instance, observed variations in surface hoar size across a slope seemed to agree with modeled variations.

Calculating accurate temperature and mass flux values for the snow surface across complex terrain with RadThermRT has been shown to be possible. Good meteorological data are necessary as is detailed topographic data. These data sets were made possible by separate weather stations at the Yellowstone Club and by costly LIDAR data from the Department of Land Resources and Environmental Sciences. Within this data the primary difficulty was obtaining incoming LW radiation data free from the effects of terrain. A pyranometer and radiometer were placed near the top of the American Spirit lift, and reasonable results for temperature were achieved. This LW data was the most important factor followed by snow albedo. Others such as core temperature and settings for the ray tracing algorithm had minimal effects. Thus, with good input data and correct settings in RadThermRT, accurate calculations of surface temperature and mass flux are possible.

REFERENCES CITED

Adams, E.E., Gauer, P., McKittrick, L.R., and Curran, A.R., 2004a. A first principles pavement thermal model for topographically complex terrain. Transportation Research Board of the National Academies, *Transportation Research Circular*, Number E-C063, ISSN 0097-8515. 422-432.

Adams, E.E., McKittrick, L.R., Gauer, P., Curran, A.R., and D.S. Levanen., 2004b. Modeling snow temperature in complex topography. *International Symposium on Snow Monitoring and Avalanches.* Manali, H.P., India.

Adams, E.E., 1999. Proof of concept for prediction of pavement temperature: A tactical decision aid for highway safety. Final Report FHWA/MT-99-003/8117, for the State of Montana Department of Transportation.

Adams, E.E. and A. Sato., 1993. Model for effective thermal conductivity of a dry snow cover composed of uniform ice spheres. *Annals of Glaciology* 18, 300-304.

Adams, E. and S. McDowell,. 1991. Thermal model for snow on three dimensional terrain. Proceedings of Japan-U.S. *Symposium on Snow Avalanche, Landslide, Debris Flow Prediction and Control*, Tsukuba, Tsukubi-shi, Ibaraki-ken, Japan pp75-84.

Birkeland, K.W., 1998: Terminology and predominant processes associated with the formation of weak layers of near-surface faceted crystals in the mountain snowpack. *Arctic and Alpine Research*, 30, 2 193-199.

Colbeck, S. C., 1980. Thermodynamics of snow metamorphism due to variations in curvature. *Journal of Glaciology* 26.

Colbeck, S.C., 1982. An Overview of Seasonal Snow Metamorphism. *Reviews of Geophysics and Space Physics* 20 (1), 45-61.

Colorado DOT Fact Book 2007-2008. Retrieved 4 August 2008 from: http://www.dot.state.co.us/topcontent/annualreports.asp

Colorado DOT Fact Book 2006-2007. Retrieved 4 August 2008 from: http://www.dot.state.co.us/topcontent/annualreports.asp

Cooperstein, M.S., Birkeland, K.W., and Hansen, K.J., 2004. The effects of slope aspect on the formation of surface hoar and diurnally recrystallized near-surface faceted crystals: Implications for avalanche forecasting. *International Snow Science Workshop. Jackson, WY.*

Fierz, C., Riber, P., Adams, E.E., Curran, A.R., Fohn, P.M.B., Lehning, M., and Pluss, C., 2003. Evaluation of snow-surface energy balance models in alpine terrain. *Journal of Hydrology*, 282, 76-94.

Fohn, P.M.B., 2001. Simulation of surface-hoar layers for snow-cover models. *Annals of Glaciology*, 32(1), 19-26.

Fukuzawa, T. and E. Akitaya. 1993. Depth-hoar crystal growth in the surface layer under high temperature gradient. *Annals of Glaciology*, 18, 39-45.

Gallatin National Forest Avalanche Center (GNFAC), 2008. 2007-2008 Annual Report.

Greene, E., and G. Johnson, 2002. Characterization of a deep instability. *International Snow Science Workshop*, Penticton, British Columbia, Canada.

Goff, J. and S. Gratch. 1946. Low-pressure properties of water from -160 to 212 F. *Transactions of the American Society of Heating and Ventilating Engineers*, 52, 95-122. 52nd Annual Meeting, New York, 1946.

Hock, R., 2005. Glacier melt: a review of their processes and their modeling. *Progress in Physical Geography*, 29 (3), 362-391.

Hudson, S.R., Warren, S.G., Brandt R.E., Grenfell, T.C. and D. Six. 2006. Spectral bidirectional reflectance of Antarctic snow: Measurements and parameterization. *Journal of Geophysical Research*, 111, D18106.

Incropera, F. and D. Dewitt, 2002. Introduction to Heat Transfer (5th ed.). John Wiley & Sons.

Ishikawa, N., Narita, H., and Kajiya, Y., 1999. Contributions of heat from traffic vehicles to snow melting on roads. *Transportation Research Record*, 1672, 28-33. Paper No. 99-0572.

Jamieson, B., and P. Langevin, 2004. Between a slab and a hard layer: Part 3—Two field studies of facets growing above wet layers. *Avalanche News*, 72, 48–51.

Johnson, K.R., 1995. A methodology for rapid calculation of computational thermal models. SAE International Congress & Exposition, Underhood Thermal Management Session, Paper Number 951012, Detroit, MI.

Johnson, K.R., 1991. Technical Reference Guide for TCM2, Interim Report to Wright Laboratory Avionics Directorate, Wright-Patterson AFB, OH, May.

List, R. 1968. Smithsonian Meteorological Tables. The Smithsonian Institution, Washington, D.C., 6th edition.

Marks, D. and J. Dozier, 1992. Climate and Energy Exchange at the Snow Surface in the Alpine Region of the Sierra Nevada 2. Snow Cover Energy Balance. *Water Resources Research* 28(11), 3043-3054.

Marttila, Eric A., 1999. A multi-mode heat transfer code for thermal analysis of automobile exhaust systems. Master's Thesis, Michigan Technological University, Houghton, MI.

McClung, D. and P. Schaerer, 1993. The Avalanche Handbook. The Mountaineers, 272pp.

McKittrick, L.R., Adams, E.E., Gauer, P., Mewes, J., and Curran, A.R., 2004. Forecasting terrain dependent weather conditions: details of a model-chain sequence. Transportation Research Board of the National Academies, *Transportation Research Circular*, Number E-C063, ISSN 0097-8515. 95-108.

Miller, D.A., E.E. Adams and R.L. Brown, 2003. A microstructural approach to predict dry snow metamorphism in generalized thermal conditions. *Cold Regions Science and Technology*, 37, 213-226.

Morstad, Blake W., 2004. Analytical and Experimental Study of Radiation-Recrystallized Near-Surface Facets in Snow. Master's Thesis, Montana State University, Bozeman, MT.

NASA, Earth Observatory, http://earthobservatory.nasa.gov/, Retrived 26 June 2008 from: http://earthobservatory.nasa.gov/Newsroom/NewImages/images.php3?img_id=16452

NOAA, Coastal Services Center, 1999. South Carolina's Coast: A Remote Sensing Perspective, Volume 1, Retrieved 11 June 2008, from NOAA's Coastal Services Center website at: http://www.csc.noaa.gov/products/sccoasts/html/tutlid.htm

Price, A., Dunne, T., and Colbeck, S. C., 1976. Energy balance and runoff from a subarctic snowpack. U.S. Army Cold Regions Research and Engineering Laboratory, Report 76-27.

Prism 3.0 User's Manual, 1991, Keweenaw Research Center, Michigan Technological University, Houghton, MI, USA, 3.0 edition.

Rees, G.W. 2006. Remote Sensing of Snow and Ice. Taylor and Francis Group, CRC Press. Boca Raton, FL.

Schneebeli, M., 2004. Numerical simulation of elastic stress in the microstructure of snow. *Annals of Glacio*logy 38, 339-342.

Stull, R.B., 1988. An Introduction to Boundary Layer Meteorology. Kluwer Academic Publishers, Dordrecht, The Netherlands.

Tremper, B., 2001. Staying Alive in Avalanche Terrain. The Mountaineers, 284pp.

USDA, Beltsville Agricultural Research Center, Electron Microscopy Unit. Electron Microscopy Unit Snow Page. Beltsville, MD, Retrieved 27 June 2008, from http://emu.arsusda.gov/snowsite/default.html

Wagnon, P., Kaser, G. and P. Berton, 1999. Energy balance and runoff seasonality of a Bolivian glacier. *Global and Planetary Change*, 22, 49–58.

Wiscombe, W.J. and S.G Warren. 1980. A Model for the Spectral Albedo of Snow. I: Pure Snow. Journal of the Atmospheric Sciences 37, 2712-2733

Washington State DOT, 2008. Measures, Markers and Mileposts, The Gray Notebook for the quarter ending March 31, 2008 :: Edition 29. Available at: http://www.wsdot.wa.gov/accountability

APPENDIX A

MANIPULATING LIDAR TOPOGRAPHIC DATA FOR USE BY THERMAL SOFTWARE

LIDAR topographic data was manipulated with a mapping program from Golden Software. A demo version of Surfer Version 8, February 2002 (Figure 54), was used to extract portions of the LIDAR data and manipulate it into a usable format. The demo version was used because it was free and provided access to necessary data manipulation tools. Output functions such as printing are disabled in the demo version, but these were not necessary. More information, the free demo download, and the full version are available at http://www.goldensoftware.com.

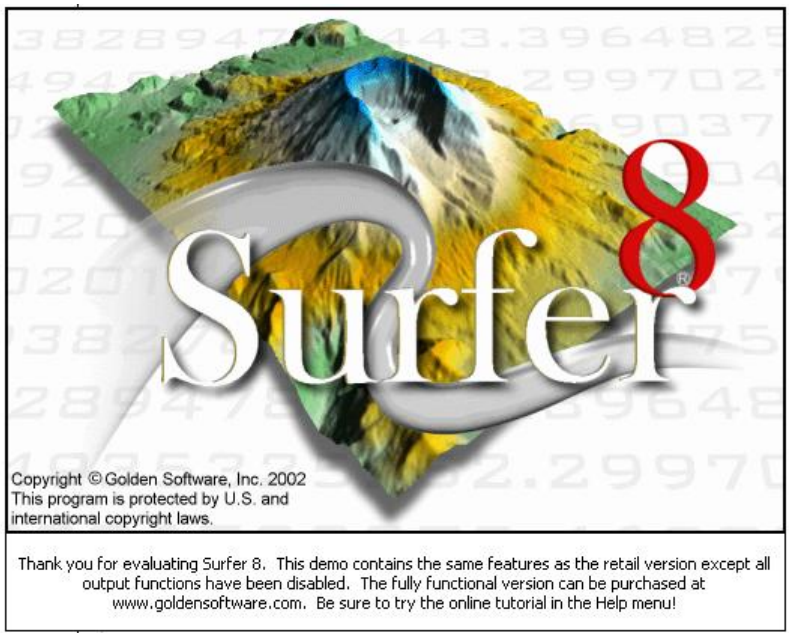

Figure 54. Demo version of the Surfer 8 mapping program from Golden Software. (http://www.goldensoftware.com)

Overview of data preparation:

STEP 1: Find the coordinates that bound the area of interest. These will be maximum and minimum x coordinates and maximum and minimum y coordinates.

STEP 2: Determine which file or files contain the required data set.

STEP 3: Convert .dat files to .grd files (usually not necessary).

STEP 4: If the data is contained in multiple files, combine these files.

STEP 5: Extract the data for the area of interest from one file.

STEP 6: Transform the data by flipping it on the x axis.

STEP 7: Change .grd files to .asc files.

STEP 8: Add header with necessary information about the data set for the thermal software.

STEP 1. Find the coordinates that bound the area of interest.

The most difficult step in using the LIDAR data is locating the area of interest. Knowing the coordinates of a given site greatly simplifies the process, and could be accomplished using handheld GPS units. Without this knowledge, one will have to manually find the coordinates. Several large files known as Mosaics (Figure 56) contain large regions of the data, and a file named "3M_unf.grd" contains the area covered by all of the mosaics. Other mosaic files contain portions of the total area and are named with the first three digits of the UTM easting coordinates bounding the region contained in that file These large files can be viewed as a topographic map in Surfer 8, allowing one to zoom in and find the area of interest. These files, however, do not contain every data

point representing the topographic data, and they should primarily be used to locate the area of interest and determine the coordinates that bound the area. In the Big Sky area, identifiable features include:

- Lone Mountain
- Pioneer Mountain
- Wilson Peak
- Cedar Mountain
- 1st, 2nd, and 3rd Yellowmule drainages
- Beehive Peak
- Beehive Basin
- Middle Basin
- Bear Basin

These topographic features can then allow one to locate a specific slope, meadow, chute, etc. Several cirques and faces of Lone Peak are easily identifiable once Lone Peak is found within the data (Figure 55).

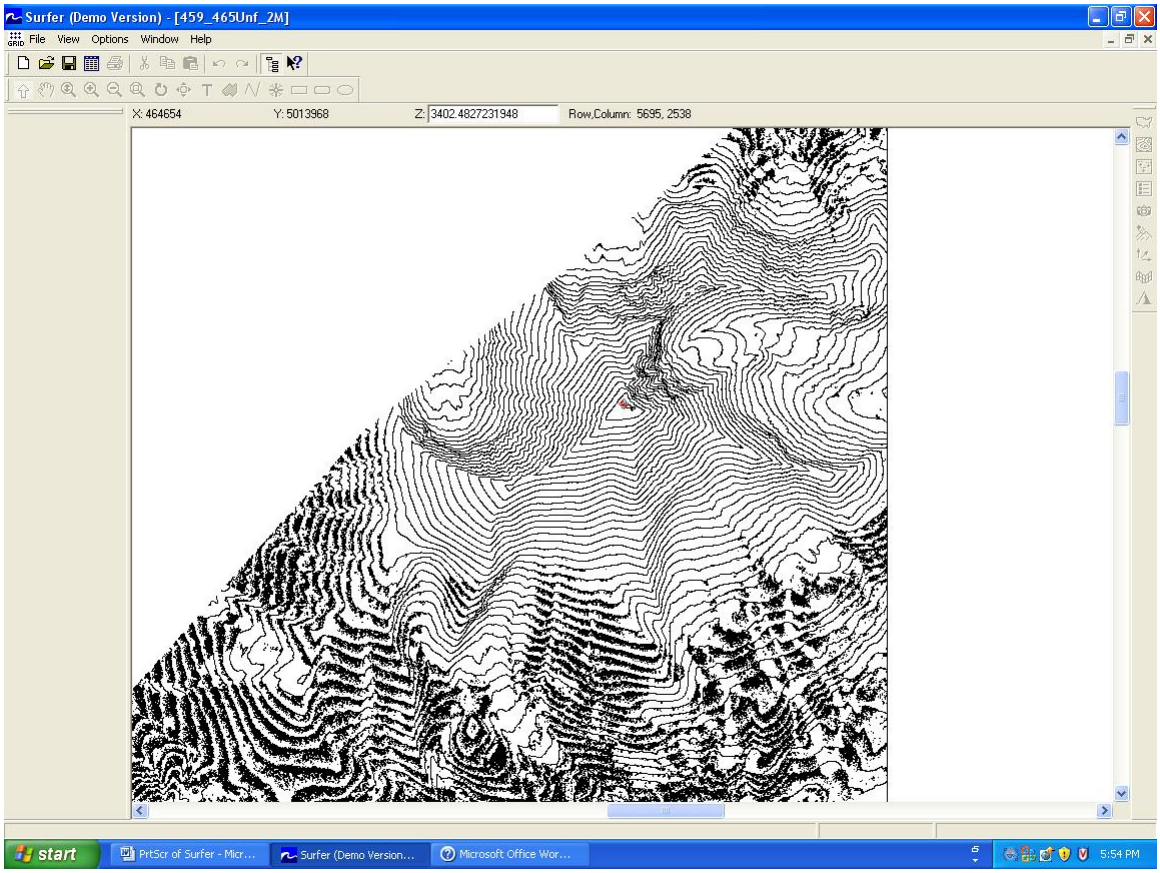

Figure 55. Surfer 8 displaying the topography of Lone Peak, Big Sky, MT in Mosaic file "459_465Unf_2M". The summit of the peak has a small dot for identification.

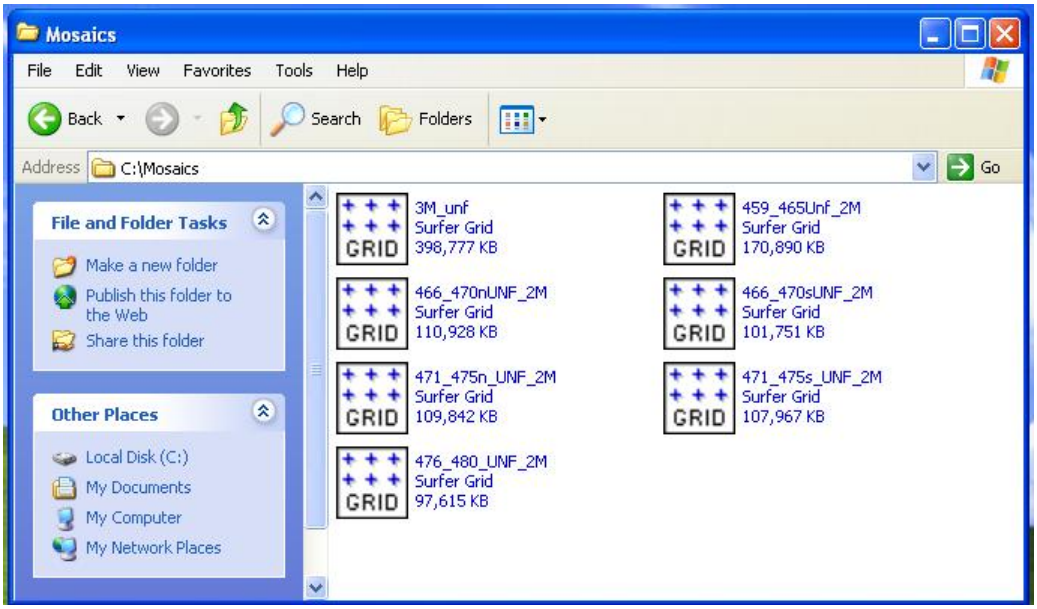

Figure 56. Mosaic files which contain large regions of the topographic data around Big Sky. These files are extremely useful in locating a specific area, but do not contain the entire set of data. They should not be used be used as a source of data from which a smaller set can be extracted when the highest level of detail is desired. They are named with the UTM Easting coordinates bounding the region in that file.

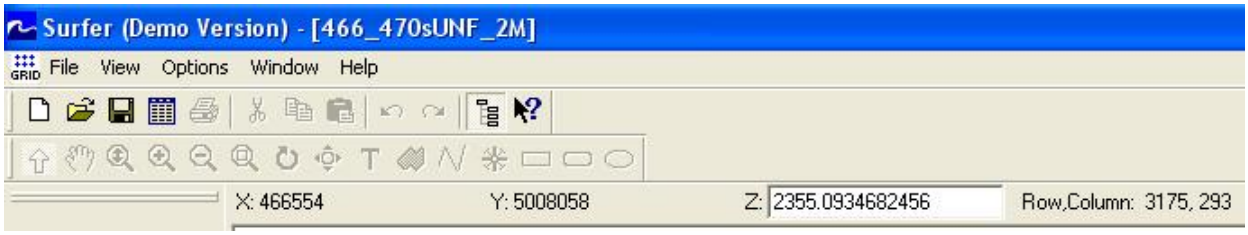

Figure 57. Toolbars of the Surfer 8 window which contains the x, y, and z coordinates for a point selected by the mouse pointer within the mosaic file "466_470sUNF_2M" and seen in Figure 56.

Once the area of interest is located, the x and y coordinates for specific points can be determined by clicking the mouse on them. These coordinates are displayed in the main

window just below the toolbars (Figure 57). Several options in Surfer 8 allow one to adjust the display to more easily see specific features.

1. Select View, click on Zoom In or Zoom Out (Figure 58).
2. To show or hide nodes, right click on the map and select Show Nodes (Figure 58).
3. To adjust the contour lines, right click on the map and select Contour Levels (Figure 58) and another window will open (Figure 59). The most useful adjustment is to change the contour interval. This is not obvious. Double click the column heading labeled "Level", and a new window will appear (Figure 60). From this new window change the contour interval.

A typical sequence involves hiding the nodes, decreasing the contour interval to see major features, zooming in on a major feature, decreasing the contour interval, zooming in more, decreasing the contour interval, and identifying the area of interest (Figure 61). Then the x and y coordinates which bound the area of interest are determined.

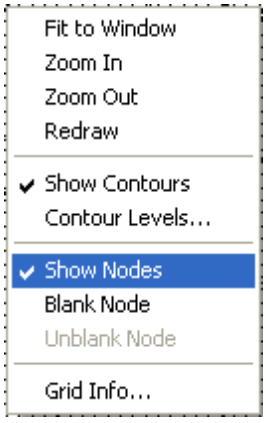

Figure 58. In Surfer 8 right clicking on the displayed map brings up this window. To show or hide nodes, check or uncheck Show Nodes. One can zoom in or out using this window as well as adjusting the contour levels.

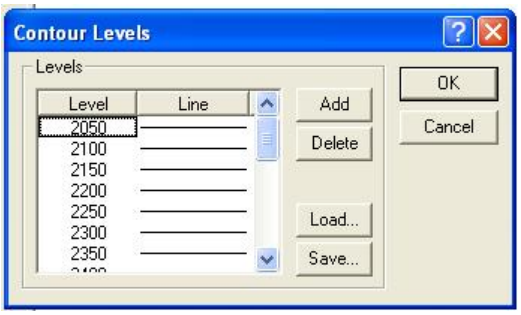

Figure 59. Selecting Contour Levels from the window in Figure 58 brings up this window in which the contour levels can be changed. To adjust the contour interval, double click the column heading "Level".

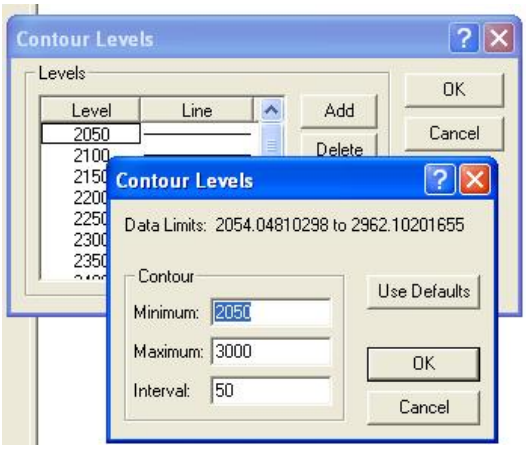

Figure 60. As one zooms in on a map in Surfer 8, decreasing the contour interval makes features more identifiable.

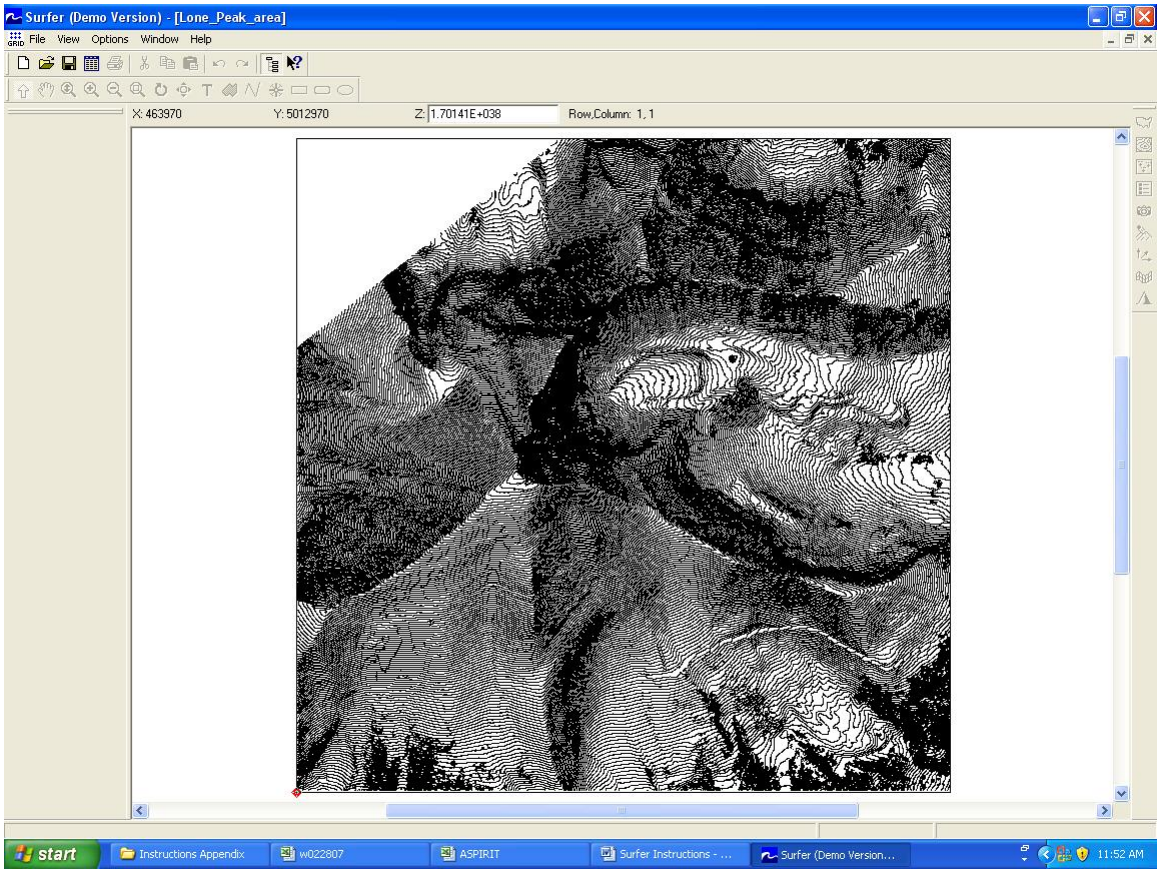

Figure 61. The same map from Surfer 8 of Lone Peak as shown in Figure 55 with the nodes hidden, but the contour interval has been significantly decreased. Certain features become more identifiable such as the road which cuts under the right side of the south face of the mountain and terminates just past the upper terminal of the Shedhorn chair lift.

STEP 2. Determine which file or files contain the required data set.

LIDAR data were provided in two file types. Filtered data were provided as a .dat file (Figure 62), and unfiltered data were provided as a .grd file (Figure 63). Both of these are recognized by Surfer, but the .dat files were converted to .grd files before the necessary data could be extracted and manipulated. The .dat files contain data in a three

column format with each row containing the x coordinate, the y coordinate, and the elevation for a given point (Figure 64).

Both file types have been given names which references the x and y coordinates contained within each file (Figure 62 and Figure 63). The names consist of a series of numbers in which the first three are the first three values of the x coordinate and the next four are the first four values in the y coordinate. For example, the file "459_5008.grd" contains x coordinates that start with 459 and y coordinates that start with 5008. These are UTM coordinates.

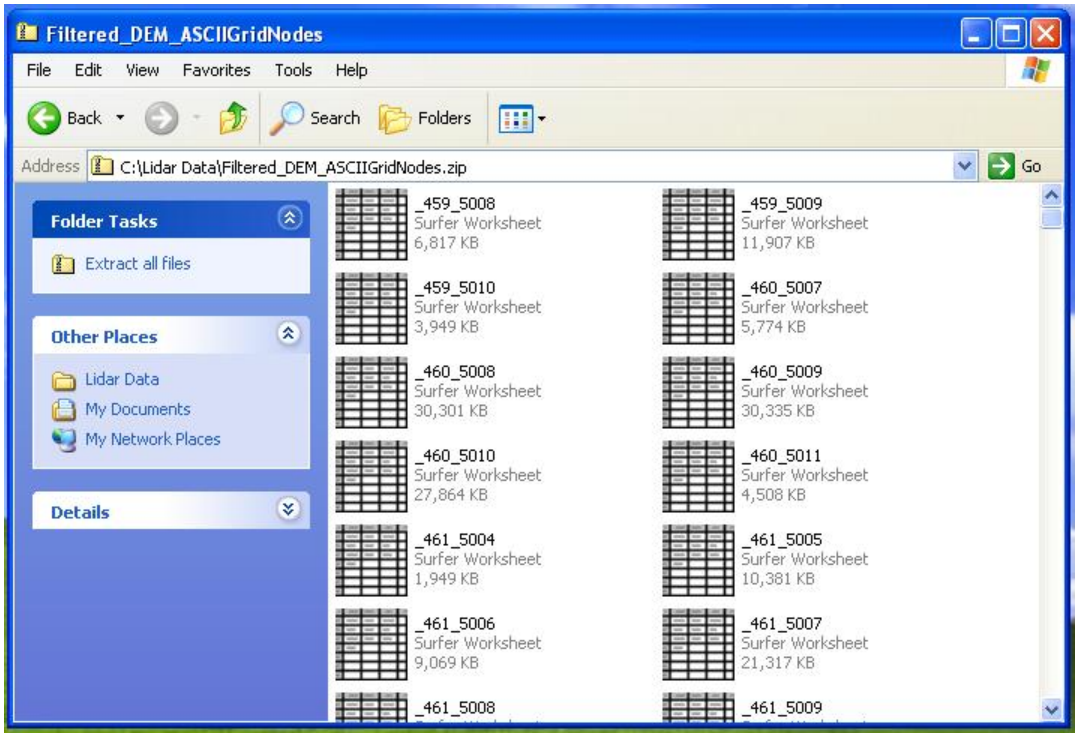

Figure 62. Surfer 8 files containing filtered LIDAR topographic data. They are labeled by the x and y coordinates contained within each file. These files have the .dat extension.

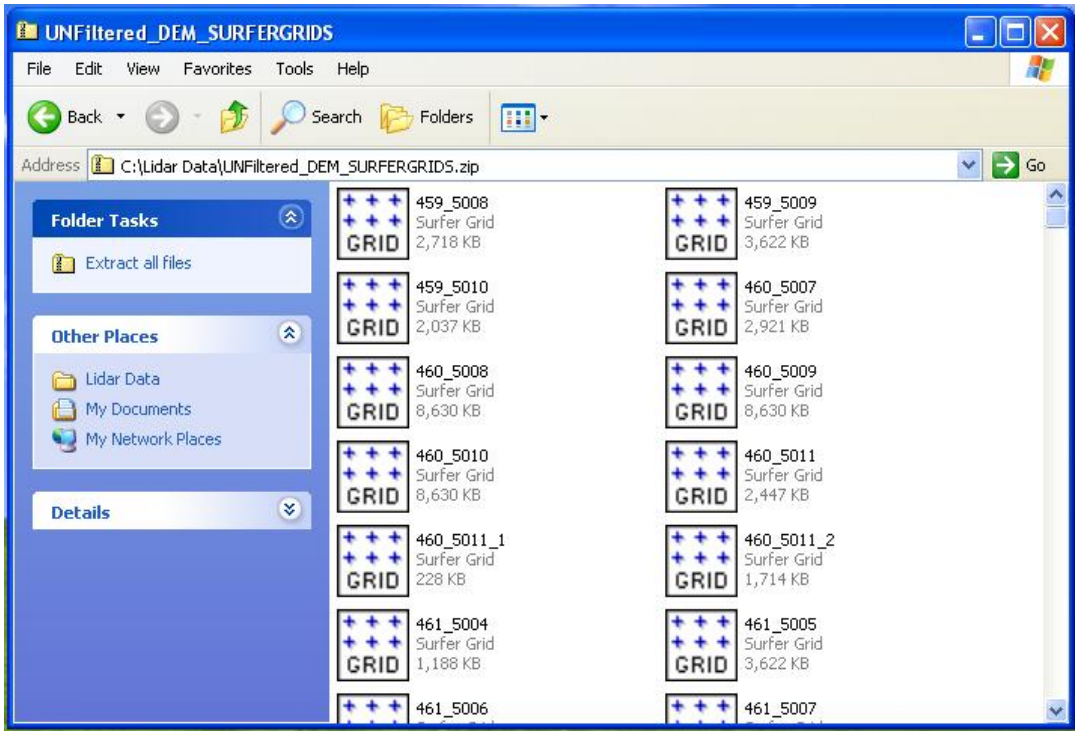

Figure 63. Surfer 8 files containing unfiltered LIDAR topographic data. They are labeled by the x and y coordinates contained within each file. These files have the .grd extension.

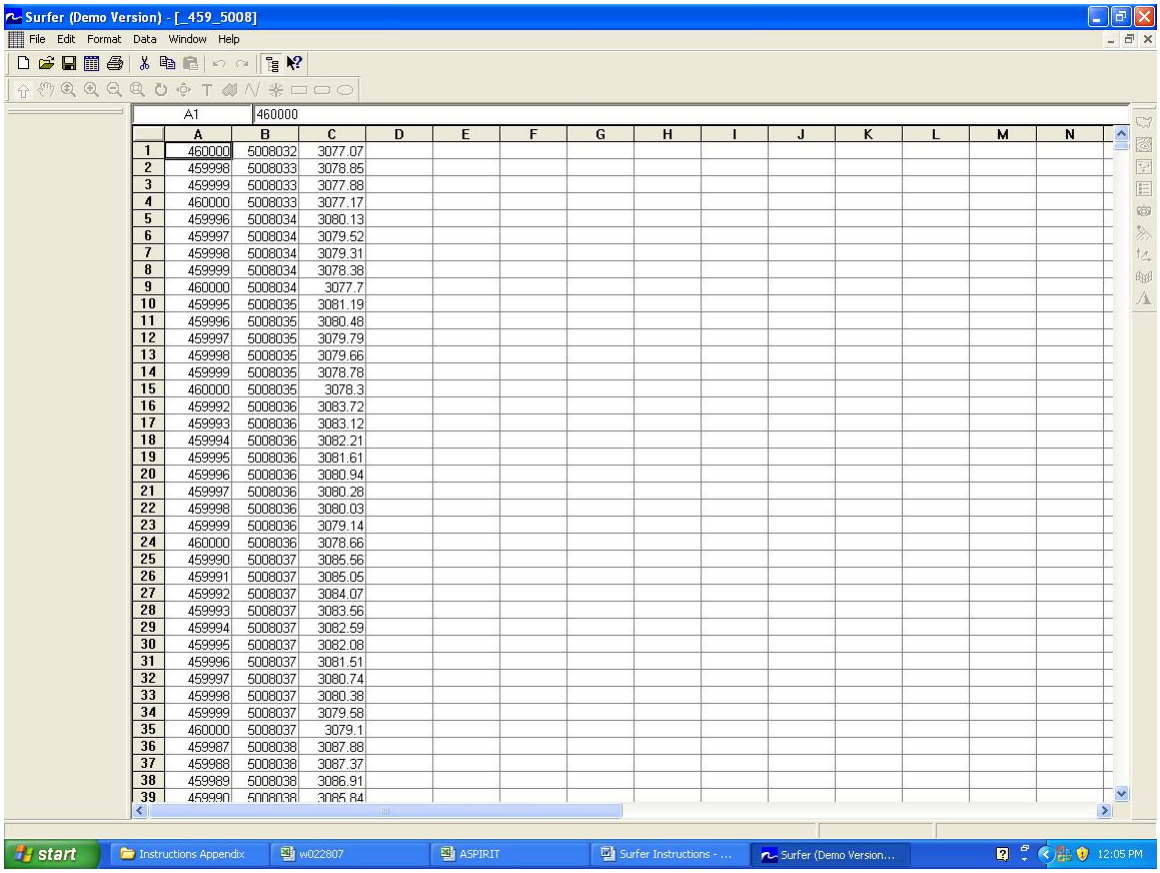

	A	B	C
1	460000	5008032	3077.07
2	459998	5008033	3078.85
3	459999	5008033	3077.88
4	460000	5008033	3077.17
5	459996	5008034	3080.13
6	459997	5008034	3079.52
7	459998	5008034	3079.31
8	459999	5008034	3078.38
9	460000	5008034	3077.7
10	459995	5008035	3081.19
11	459996	5008035	3080.48
12	459997	5008035	3079.79
13	459998	5008035	3079.66
14	459999	5008035	3078.78
15	460000	5008035	3078.3
16	459992	5008036	3083.72
17	459993	5008036	3083.12
18	459994	5008036	3082.21
19	459995	5008036	3081.61
20	459996	5008036	3080.94
21	459997	5008036	3080.28
22	459998	5008036	3080.03
23	459999	5008036	3079.14
24	460000	5008036	3078.66
25	459990	5008037	3085.56
26	459991	5008037	3085.05
27	459992	5008037	3084.07
28	459993	5008037	3083.56
29	459994	5008037	3082.59
30	459995	5008037	3082.08
31	459996	5008037	3081.51
32	459997	5008037	3080.74
33	459998	5008037	3080.38
34	459999	5008037	3079.58
35	460000	5008037	3079.1
36	459987	5008038	3087.88
37	459988	5008038	3087.37
38	459989	5008038	3086.91
39	459990	5008038	3085.84

Figure 64. Surfer files with the .dat extension contain three columns which contain x coordinates, y coordinates, and elevations. These file types must be converted to .grd files in which data is stored in a matrix of elevation data which can be displayed as a map image in Surfer 8 (Figure 61) or as an asc **file** using software such as WordPad or Notepad (Figure 71)

STEP 3. Convert .dat files to .grd files.

To convert *.dat files to *.grd files (Figure 65):

1. Open Surfer 8.
2. Click Grid on the menu bar.
3. Select Data from the drop down menu.
4. Open the file to be converted.
5. Select the columns which contain the x, y, and z values.
6. Name the output file and choose the file type GS ASCII (*.grd). Do this by clicking on the folder icon to the right of the name of the output file.
7. Adjust the # of Lines so that the Spacing for the Grid Line Geometry is 1.
8. Click OK

(Note: The filtered data, thus the *.dat files should only be used if topographic data which excludes vegetation is desired)

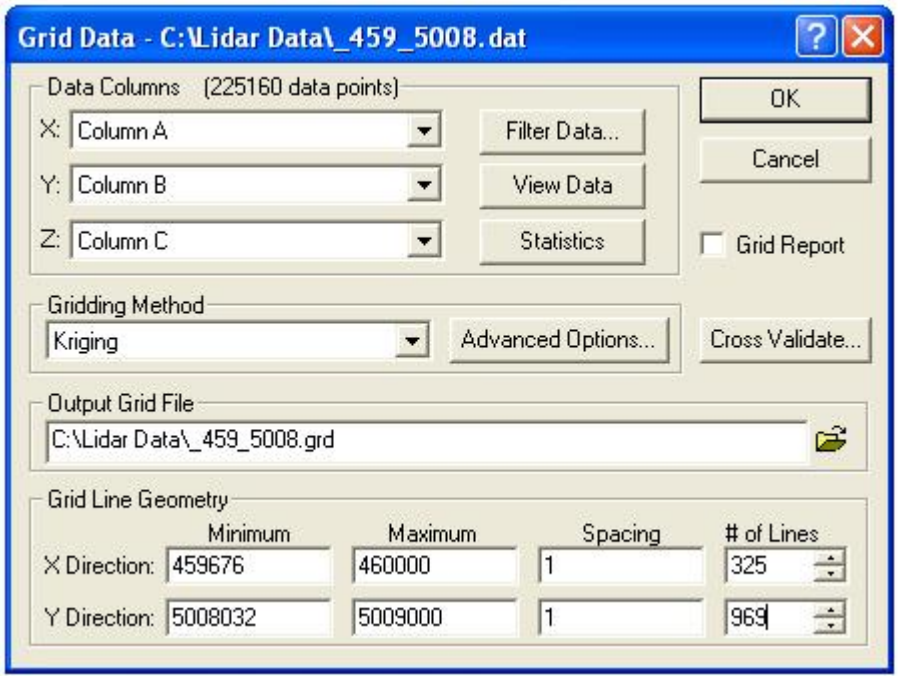

Figure 65. Data window in Surfer 8 allowing .dat files to be converted to .grd files.

STEP 4. If the data is contained in multiple files, combine these files.

Individual files of data can be combined in a similar fashion by clicking Grid on the menu and selecting Mosaic from the drop down menu (Figure 66). Combining files would be necessary if the area of interest overlapped several files.

1. Open Surfer 8.
2. Click Grid on the menu bar.
3. Select Mosaic from the drop down menu, and the "Grid Mosaic" window opens (Figure 66).
4. Open one of the files to be combined
5. Click on the Add button to add other files to be combined. The relative location of grids of data to each other will be shown in a box in the lower right corner of the window
6. Name the output file and choose the file type GS ASCII (*.grd). Do this by clicking on the folder icon to the right of the name of the output file.
7. Click OK

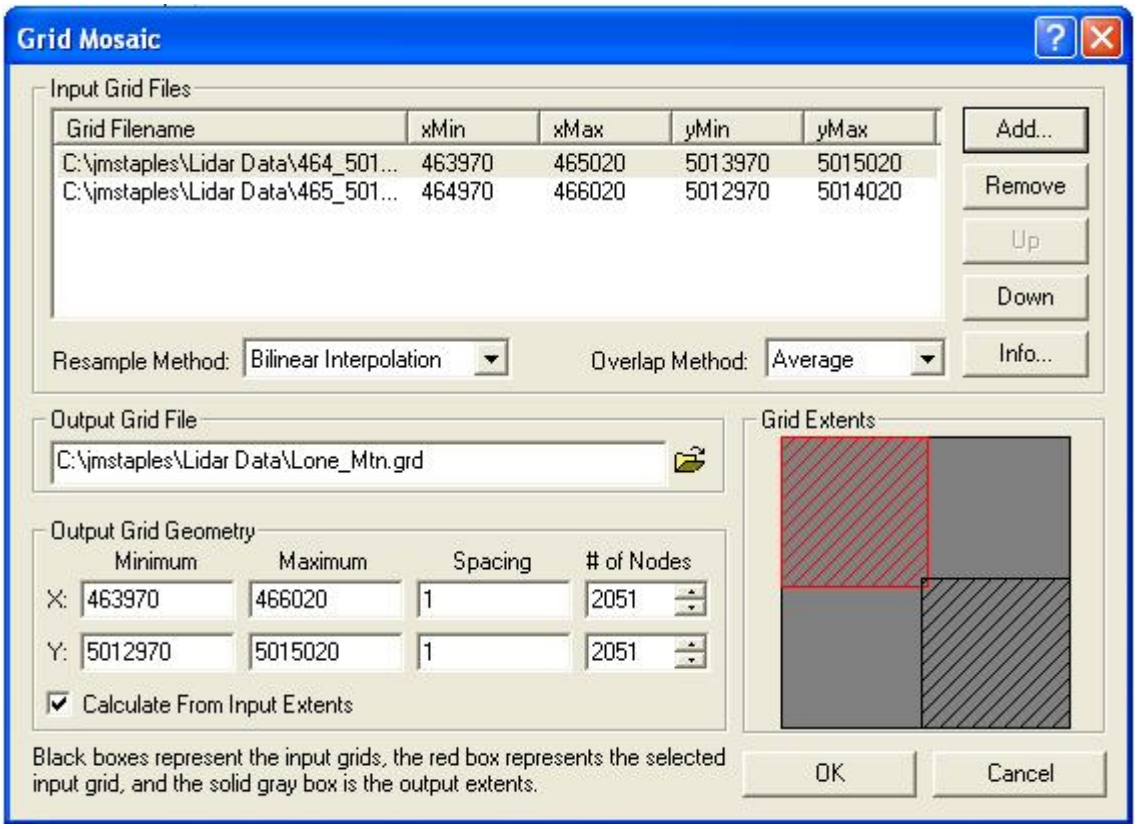

Figure 66. Mosaic window in Surfer 8 allowing .grd files to be combined into one file. The lower right corner labeled Grid Extents shows the relative positions of the selected files.

STEP 5. Extract the data for the area of interest from one file.

Once the area of interest has been found either by inspection or using known coordinates, the maximum and minimum values for the x and y coordinates need to be recorded. The area of interest can then be extracted from the larger set of data (Figure 67). The procedure is:

1. Open Surfer 8.
2. Click Grid on the menu bar.
3. Select Extract from the drop down menu, and the "Extract Grid" window opens (Figure 67).
4. Name the output file and choose the file type GS ASCII (*.grd). Do this by clicking on the folder icon to the right of the name of the output file.
5. Adjust the First and Last numbers for the x and y values so that the Minimum and Maximum x and y values are the correct ones to bound the area of interest.
6. The Read Every boxes for x and y can be adjusted so that every nodal value within the bounded area is extracted (select 1) or every other nodal value is extracted (select 2). Other numbers can be selected. Higher numbers reduce the file size and reduce the resolution.
7. Click OK.

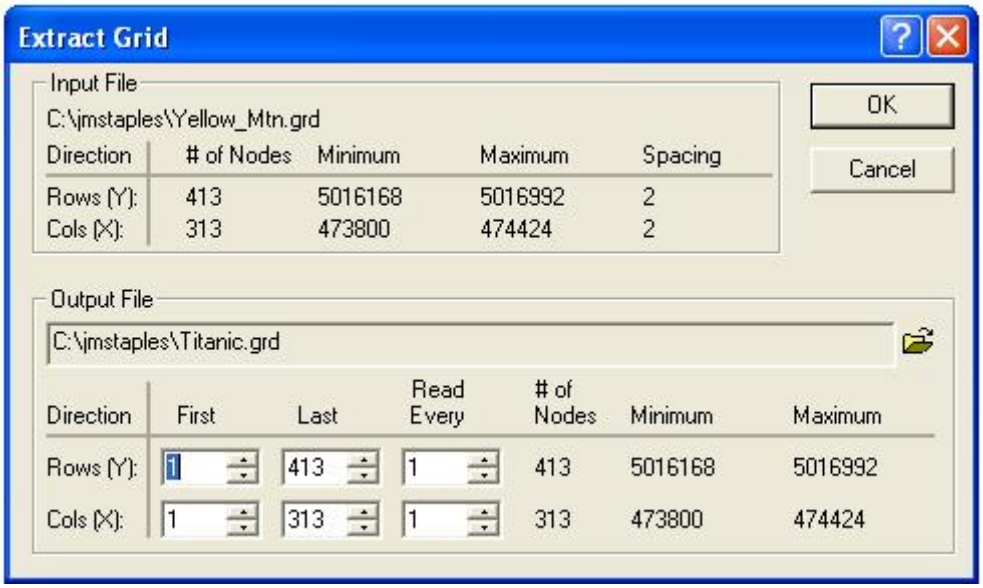

Figure 67. Extract window in Surfer 8 allowing a specific set of data to be extracted from a single .grd file. The size of the resulting file can be reduced by changing the Read Every boxes. In this case the output file will contain the data from every node within the selected area. The original LIDAR data has a horizontal resolution of one meter, and the spacing value of 2 for the input file means it has resolution of two meters. The output file reads each node and will have a two meter resolution as well.

STEP 6. Transform the data by flipping it on the x axis.

In order for the thermal software to assign the correct cardinal directions to the data set, each one was flipped on the x axis (Figure 68). While there may be other methods to manipulate the data so that it is oriented accurately in the thermal software, this one is simple and works.

1. Open Surfer 8.
2. Click on Grid on the menu bar.
3. Select Transform from the drop down menu.
4. Open the file to be transformed.
5. Select the operation to be performed. In this case select Mirror Y.
6. Name the output file and choose the file type GS ASCII (*.grd). Do this by clicking on the folder icon to the right of the name of the output file.
7. Click OK.

Figure 68. Transform window in Surfer 8 allowing a specified input file to be transformed by a given operation. Files containing the LIDAR topographic data needed to by transformed with the Mirror Y operation which flips the data on the x axis.

STEP 7. Change .grd files to .asc files.

The thermal software accepts topographic data in .asc files. The .grd files (Figure 69) created by Surfer 8 in the GS ASCII format can simply have the file extension changed to .asc. This is easily done in the file transfer window of the secure shell client used to connect to the remote server which contains the thermal software. Files with the .grd extension are renamed with the .asc extension (Figure 70).

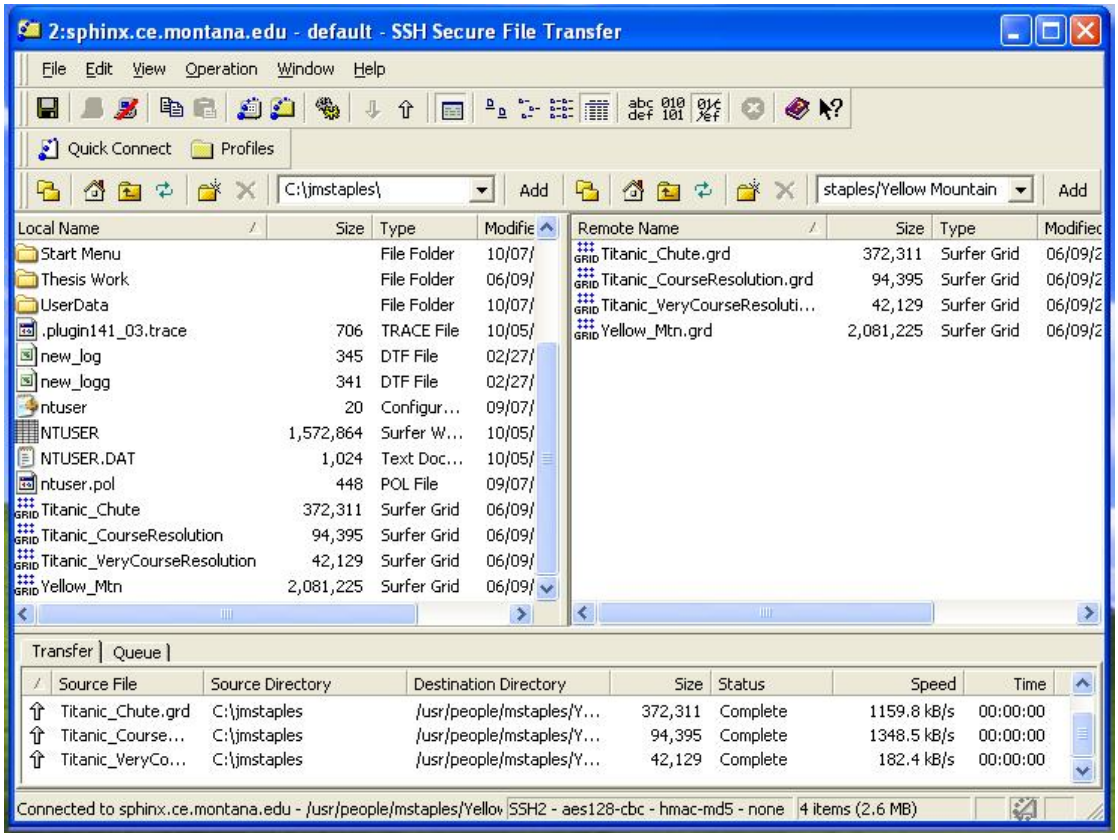

Figure 69. Surfer 8 .grd files have been transferred to the remote server that contains the thermal software. These files need to have the extension changed from .grd to .asc.

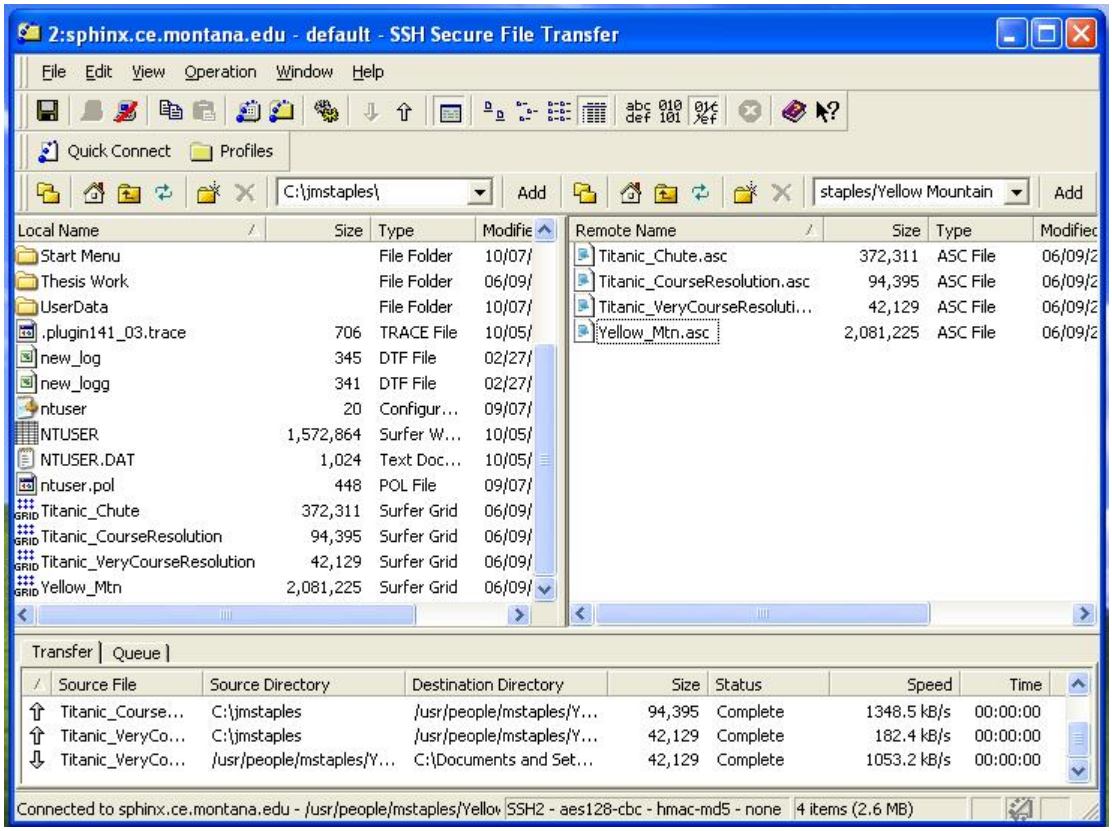

Figure 70. Files with a .grd extension were changed to .asc by renaming them in this file transfer window.

STEP 8. Add header with necessary information about the data set for the thermal software.

Once the files containing the topographic data are given the .asc extension, the header within such files must be changed to give the thermal software the necessary information (Figure 71). The header needs to be changed to give the year date, the number of columns, the number of rows, the x coordinate of the lower left corner, the y coordinate of the lower left corner, the cell size, and the NODATA value. With this header, the topographic data is ready to be read by the thermal software (Figure 72).

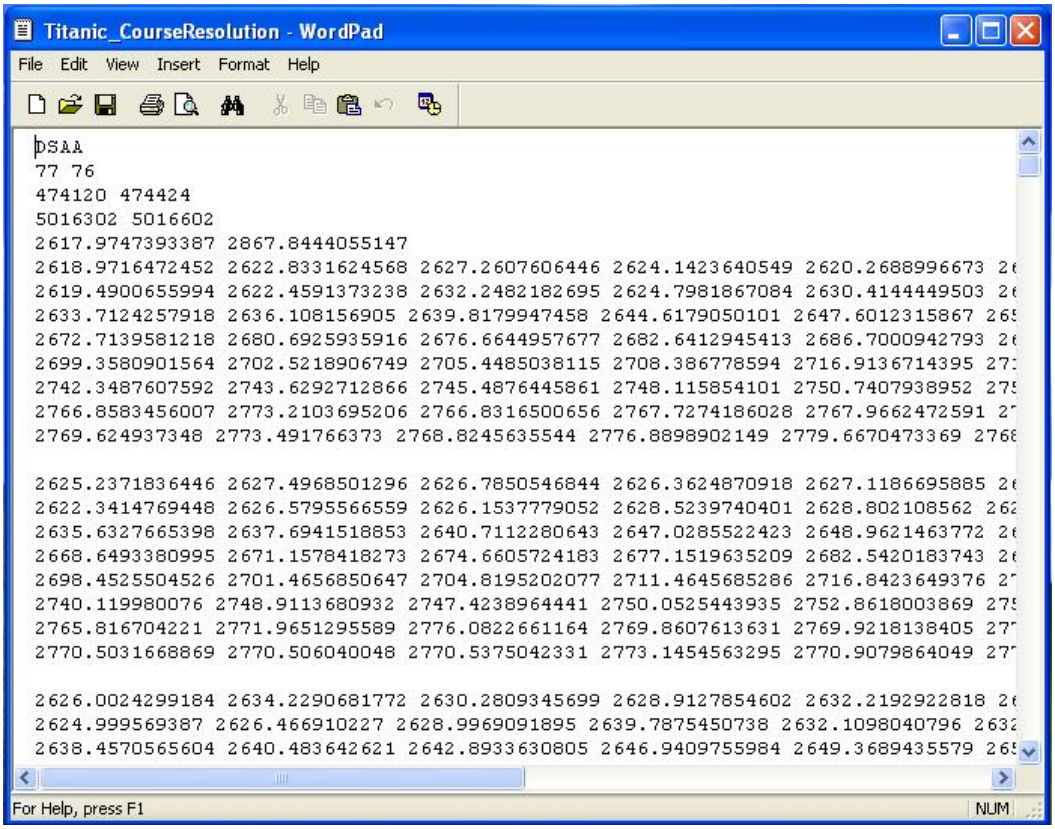

Figure 71. Topographic data from both .grd and .asc files in a matrix of elevation values. This file contains the Surfer 8 header which needs to be changed to a format recognized by the thermal software.

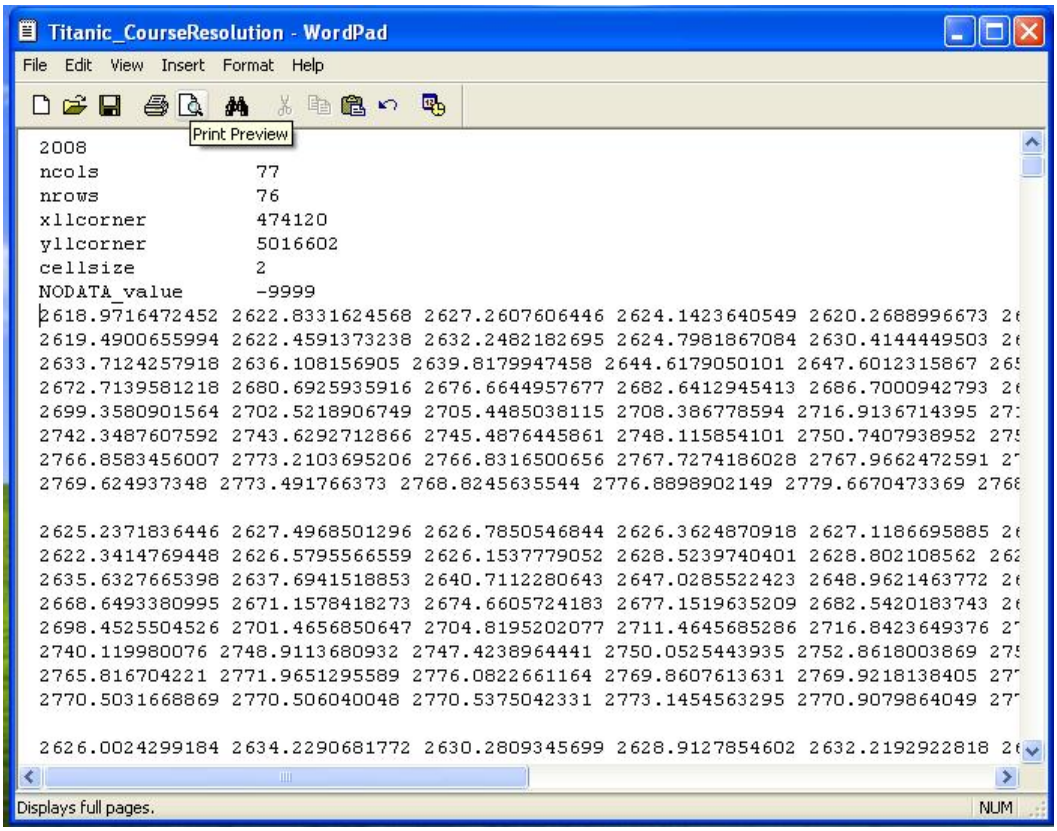

Figure 72. Topographic data in a matrix of elevation values with a header recognized by the thermals software. The cell size refers to the horizontal resolution of the data. In this case the resolution or the distance between nodal elevations is 2 meters.